UNIVERSITY OF SOUTHAMPTON

FACULTY OF PHYSICAL SCIENCES AND ENGINEERING

School of Electronics and Computer Science

Colloidal Quantum dots based hybrid LEDs and Photovoltaics

by

Chirenjeevi Krishnan

Thesis for the degree of Doctor of Philosophy

May 2017

UNIVERSITY OF SOUTHAMPTON

ABSTRACT

FACULTY OF PHYSICAL SCIENCES AND ENGINEERING

School of Electronics and Computer Science

Thesis for the degree of Doctor of Philosophy

COLLOIDAL QUANTUM DOTS BASED HYBRID LEDS AND PHOTOVOLTAICS

Chirenjeevi Krishnan

Colloidal quantum dots (QDs) have proven themselves as excellent light emitters and strong absorbers. This work aims to use QDs to enhance the performance of light emitting diodes (LEDs) and photovoltaics. Photonic quasi crystals (PQC) are used to bring QDs close to quantum wells (QWs) of InGaN LED. This thesis demonstrates the colour conversion effective quantum yields of 123% and 110% for single colour QDs and white LEDs respectively. High colour conversion quantum yield was made possible through efficient coupling of QDs and QWs by both radiative and non-radiative resonant energy transfer (RET). Existence of RET between QWs and QDs is demonstrated using the time resolved photoluminescence spectroscopy. The PQC LED module with current tunable submodules was inkjet printed with different colours of QDs. Reproducibility and correlated colour temperature tunability of colour tunable module using inkjet printing is also demonstrated. Lead sulfide (PbS) QDs as a superficial layer on Si solar cell has shown the absolute and relative photon conversion efficiencies of 1.37% and 20% respectively. This improvement in photon conversion was achieved through luminescent down shifting and RET from QDs to underlying silicon. The PbS QD at the surface also serves as a refractive index matching layer thus the light scatters, increasing the coupling of photon into the Si solar cell. CdSe/ZnS (core/shell) QDs were also hybridised on the planar Si solar cell and optical enhancements were investigated. It was demonstrated that the QD layer can also serve as an efficient refractive index layer and optimum thickness was found through dispersing QDs at different spin speeds. Finally, PQC was used to bring CdSe/ZnS QDs in proximity to metallurgical junction of the Si solar cell. For optimised QD layer, the relative enhancement of Jsc was found to be 17.5%. It was shown that by increasing the air fill fraction of the PQC solar cell, efficient light trapping can be achieved. On hybridisation with CdSe/ZnS QDs, short circuit current of 31.67mA/cm^2 was demonstrated. When the comparison was drawn between the champion hybrid PQC solar cell and planar device, the hybrid PQC showed an absolute and relative Jsc enhancement of 9mA/cm^2 and 41% respectively.

Table of Contents

List of Tables

List of Figures

DECLARATION OF AUTHORSHIP

I, **Chirenjeevi Krishnan** declare that this thesis and the work presented in it are my own and has been generated by me as the result of my own original research.

COLLOIDAL QUANTUM DOTS BASED HYBRID LEDS AND PHOTOVOLTAICS

I confirm that:

1. This work was done wholly or mainly while in candidature for a research degree at this University;
2. Where any part of this thesis has previously been submitted for a degree or any other qualification at this University or any other institution, this has been clearly stated;
3. Where I have consulted the published work of others, this is always clearly attributed;
4. Where I have quoted from the work of others, the source is always given. With the exception of such quotations, this thesis is entirely my own work;
5. I have acknowledged all main sources of help;
6. Where the thesis is based on work done by myself jointly with others, I have made clear exactly what was done by others and what I have contributed myself;
7. Parts of this work have been published as:
    - **C. Krishnan**, M. Brossard, K.-Y. Lee, J.-K. Huang, C.-H. Lin, H.-C. Kuo, M. D. B. Charlton, and P. G. Lagoudakis, "Hybrid photonic crystal light-emitting diode renders 123% color conversion effective quantum yield," Optica 3, 503–509 (2016).
    - Y.-L. Tsai, C.-Y. Liu, **C. Krishnan**, D.-W. Lin, Y.-C. Chu, T.-P. Chen, T.-L. Shen, T.-S. Kao, M. D. B. Charlton, P. Yu, C.-C. Lin, H.-C. Kuo, and J.-H. He, "Bridging the “green gap” of LEDs: giant light output enhancement and directional control of LEDs via embedded nano-void photonic crystals," Nanoscale 8, 1192–1199 (2016)
    - J. Z. Liu, M. D. B. Charlton, C. H. Lin, K. Y. Lee, **C. Krishnan**, and M. C. Wu, "Efficiency Improvement of Blue LEDs Using a GaN Burried Air Void Photonic Crystal With High Air Filling Fraction," IEEE J. Quantum Electron. 50, 314–320 (2014).
    - Y. Y. Huang, W. Pan, Y. C. Lai, T. T. Yang, R. Chen, **K. Chirenjeevi**, W. S. Weng, P. Yu, H. F. Meng, and M. Charlton, "Characteristics of conductive polymer/silicon heterojunction solar cells with periodic nanostructures," 2013 IEEE 39th Photovolt. Spec. Conf. 1028–1030 (2013).

- Y.-K. Liao, T.-Y. Chuang, D.-H. Hsieh, S.-C. Chen, **K. Chirenjeevi**, K.-J. Chen, P. Lagoudakis, M. D. B. Charlton, P.-C. Yu, C.-C. Lin, and H. Kuo, "An 11% Efficiency Boost of Flexible Inkjet-printing Cu(In,Ga)Se2 Solar Cells byNon-radiative Energy Transfer of Nano-crystal Quantum Dots," in CLEO: 2013 Postdeadline, OSA Postdeadline Paper Digest (Online) (Optical Society of America, 2013), p. ATh5A.3.

Signed: .....

Date: .....

Acknowledgements

I would like to thank my supervisors Dr. Martin Charlton and Prof. Pavlos Lagoudakis for giving me the opportunity to work in this interesting field. Dr. Martin Charlton, thank you for introducing me to the field of photonic crystals and sharing the valuable knowledge about reflectometery. I could not ask for a better supervisor. Pavlos, thank you for the weekly meeting. Looking back at them, they were my learning sessions during my PhD. Mael, you are a terrific scientist and hope to see you reach high level in the field of research and thank you for teaching me what is science and how research is done.

The modular LED for work on hybrid PQC LEDs was provided by luxtaltek corporation Taiwan. Sean, thank you for trusting me to handle your LED samples, it was a stepping stone for my pathway during my PhD. I would like to thank Dr Russel Torah for training and valuable discussions on inkjet printing. Work on solar cells presented in this thesis would have not been possible without shallow p-n junction wafers from QCells. Giacomo thanks a lot mate for help with time resolved measurements.

PhD life would have been terrible without jokes from Tasmiat and Jing shi. You guys can create fun out of anything. Mike thanks for guiding me in the first two years of my PhD. The passion towards research is awesome; I wonder if there is anything you do not know about optics. Swezin thanks a lot for the support and friendship you have given me over these years. Pisi your fun and thanks for the pen which has helped my research. I would like to thank my best friend Arifa for motivating me to finish up my thesis.

I would like to dedicate this thesis to Amma, Appa and Akka and Mama for their support and love and pushing me to pursue PhD. I have no words to put forward for my love to my wife for understanding me during write up and taking care of our new born baby boy single handed.

Acronyms

CCT	Correlated colour temperature
CRI	Colour rendering index
EQE	External Quantum Efficiency
EL	Electroluminescence
ICP-RIE	Inductively coupled plasma reactive ion etching
IQE	Internal quantum efficiency
Jsc	Short circuit density
LDS	Luminescent down shifting
LED	Light emitting diode
MQW	Multiple quantum well
PV	Photovoltaics
PSS	Patterned sapphire substrate
PL	Photoluminescence
PhC	Photonic crystal
PQC	Photonic quasi crystal
QW	Quantum well
QD	Quantum dot
RIE	Reactive ion plasma etching
R.I	Refractive Index
RET	Resonant energy transfer
SEM	Scanning Electron Microscope
TRPL	Time resolved photoluminescence
UV	Ultra violet

Chapter 1: Introduction

Semiconductor nanoparticles are made up of nano-crystalline material with few hundreds to thousands of atoms [1]. Nano particles are often referred as Quantum dots (QDs). Quantum dots are grow by using molecular beam epitaxy and different lithographic approaches and is few tens of nano-metre [2]. The challenge is to obtain semiconductor QDs with preferred size (less than 10nm) using this top-down approach. Colloidal suspension of QDs can be prepared via chemical synthesis and sizes vary between 2 nm and 10 nm. In bottom up approach, chemical synthesis gives a precise control of size and shapes such examples are spherical quantum dots [3,4], quantum rods [4,5] and tetrapods [4]. Colloidal quantum dots is the subject of this thesis and is referred as QDs in the text. When QDs are confined in all three dimensions, it exhibits size dependent electrical and optical properties and they become significant when it reaches the Bohr radius of the bulk counterpart. One of the interesting properties of QDs is the size dependant emission in the visible and near –infrared region of the spectrum.

Colloidal quantum QDs have shown tremendous improvement in their performance through core /shell band-gap engineering [6–8] and surface passivation [9–11], achieving near unity photoluminescence quantum yield [12]. One of the delimiting factor for CQDs was toxicity due to use of heavy metals like Cd and Pb. Ongoing research have shown promising results on environmental friendly quantum dots like Si [13] and InP/ZnS [14,15]. The band gap tunability, large absorption cross-section, brightness, cost-effective and easy integration in devices have attracted QDs within different domains of the scientific community. As a result, colloidal QDs have found their way in applications like LEDs [16–18], photovoltaics [19,20], biological sensing [21,22] and lasers [23].

As the semiconducting materials move from bulk to nanoscale, the ratio of surface atoms increase and act as trap centres. The passivation of QDs is achieved through encapsulation of core QDs with wider band gap shell or organic ligands. The passivation hinders the injection or extraction of charge carriers from QDs. Dexter [24] proposed a hybrid organic/ semiconductor hetero-structure, in which organic layer act as an absorbing layer and transfers the electron-hole pair to underlying semiconductor via non-radiative resonant energy transfer (RET). The idea of Dexter was extended to QDs/semiconductors hybrid structures for light emitting [25,26] and light harvesting applications [27]. This thesis will focus on hybrid QD LEDs and photovoltaics, to enhance their performance through RET and luminescent down shifting (LDS). A brief overview of colloidal QDs based LEDs and photovoltaics will also be presented.

1.1 Colloidal QDs light emitters

Comprehensive usage of light emitting diodes for lighting in United States by 2027 [28] could save upto ~348 terawatt-hour (TW.h) of energy. This is equivalent to the power generated by 44 large electric plant where each has the capability to provide 1000 megawatt. The estimated savings is in the region of 30 billion US dollars, given the current prices of electricity.

Student services centre of Southampton University has changed old incandescent and fluorescent lamps to efficient LEDs. This lead to 35 tonnes of reduced carbon emission making energy savings of approximately 8500 pounds a year. Although, this is a small in-house example but a global incentive has been taken to replace the conventional lamps with LEDs considering the environmental impacts. This demands energy efficient solid state light emitters. The current commercial LEDs uses blue InGaN blue LED and yellow colour converting phosphours to emit white LEDs. The phosphors have a maximum spectral width of 50-100nm resulting in poor colour saturation. Indoor lighting and industrial lighting need different requirements of correlated colour temperature and colour rendering index. Correlated colour temperature (CCT) denotes comparison of light source with black body emitter at different temperatures. Colour rendering index (CRI) compares the illumination of object under the illumination source in comparison to sunlight. It will be attractive to have light emitters that will be able to cover different parts of spectrum with high colour saturation.

Colloidal QDs emission wavelength can be tuned by synthesis [3], making it a suitable candidate for lighting applications. As the size of QDs decrease, the blue shift in the spectral emission of QDs can be seen. Also, the spectral tunability of QDs can be obtained by changing their chemical composition [30,31]. Colloidal QDs have demonstrated emissions in UV to mid infrared regions of the spectrum. CdZnS/ZnS (core/shell) with reduced core QDs have shown emission below 400nm [32]. Visible and near infrared emission regions of the spectrum is covered by CdSe/ZnS (core/shell) [17] and PbS [33] based QDs. Colloidal synthesised PbTe/CdTe (core/shell) QDs have shown mid infrared emission between 1µm and 3µm [34].

QDs can be electrically driven with sophisticated electron and hole transport layer. The maximum EQE of QD LED reported is 20.5% [35]. The best reported EQE for convention InGaN quantum well blue LED is over 80% [36]. QDs can be optically excited and have already been implemented in QD lighting and displays.

QDs have shown to have high colour purity with full width half maximum of ~30nm [37]. High colour rendering index (CRI) of ~90% have been reported by blending blue, green, red QDs for

electrically driven QD LEDs [38]. In case of optical driven QD LED, green and red LEDs are deposited on the surface of blue LEDs [39].

High colour saturation and easy integration of QDs with spin deposition, inkjet printing [40] and spray deposition [41] have led to development of QD based displays. QDs based displays are already being commercialised [42] by start-ups like QD vision, Nanosys as well as giant corporations like Samsung and Sony.

Apart from electrical and optical excitation, the QDs can also be excited via non-radiative transfer from adjacent QWs [25]. Brief overview of state of the art QD LEDs and QD excitations schemes are presented in chapter 2.

Currently, electrically driven QD LEDs have relatively low EQE and optically driven QD LEDs does not efficiently utilise the photons generated by excitation of QDs. In this work, the author aims to bring the QDs close to excitation source therefore enhance the performance of QD LEDs through efficient coupling by radiative and non-radiative resonant energy transfer.

1.2 Colloidal QDs light harvesters

Quantum size of QDs can be used to tune the absorption profile of QDs which makes it an attractive material for photovoltaics. Recently, the colloidal QDs photovoltaic cell have been reported with absolute power conversion efficiency of ~11.6 [43]. This enhancement is a benchmark for QD solar cells as it catches up with the rival organic photovoltaics with efficiency of 11.3% [44]. The high efficiency in solar cells was achieved through years of research in improving electronic properties of QDs [45].

The photovoltaic foundation lies on absorbing the incoming solar radiation, generating electron-hole pairs, dissociating and collecting at respective electrodes. . The photon absorption at QD site and direct extraction of charge carriers is an interesting phenomenon. For QDs to be a commercially viable technology, electronic trap densities and diffusion length in QDs has to be improved [45].On the other hand, silicon is a mature technology with good electronic properties with record solar cell efficiencies of 26.5% [46]. The high enhancement in silicon solar cells were made possible through matching the absorption of Si to solar cells using light trapping structures. Silicon is a poor absorber in comparison to solution processed QDs. Most researched materials for colloidal QDs are infrared PbS and PbSe QDs. Optical penetration depth for PbSe QDs are estimated to be 20nm and 500nm at 400nm and 1700nm wavelengths respectively [47].

The Concept of hybrid photovoltaics was envisaged by Dexter [48], the hybrid structure consisted of metal-semiconductor schottky solar cell embedded in organic layer. Incoming solar photons are absorbed by highly absorbing organic layer and transferred to semiconductor via non-radiative resonant energy transfer. This revolutionary idea has already been demonstrated between organics/QD to silicon [49,50].Hence, this thesis focuses to extend this work and aims to use QDs as absorbing layer and enhance the performance of silicon solar cells through non-radiative resonant energy transfer and luminescent down shifting. Hybrid QD/Si structure can overcome the need for electronic transport in QDs consequently make QDs based technologies more commercially viable. Hybrid configuration can also potentially reduce the need for 200μm silicon hence lowering the cost of PVs.

1.3 Motivation and thesis structure

The aim of this thesis is to demonstrate high colour conversion hybrid QD/ InGaN MQW LED and enhance the performance of hybrid QD/ silicon solar cell. In particular the aim is to utilize RET mechanism to enhance the coupling of QWs and QDs in hybrid LED architecture. In case of hybrid QD/Si solar cells, the aim was efficient photon management through RET, LDS and refractive index matching. In chapter 2, the reader will be introduced to the solid-state physics of QDs. A review on colloidal QDs for LED and solar applications is presented. The principle of resonant energy transfer is also discussed along with its applications in LEDs and solar cells. Chapter 2 touches the basic overview of photonic quasicrystals. Chapter 3 is on hybrid photonic quasi crystal LEDs, and it shows that the resonant energy transfer can enhance the pumping of QDs thus achieving above 100% colour conversion quantum yield. The existence of resonant energy transfer was verified using time resolved spectroscopy. It was also demonstrated through optimising the ratio of three different QDs in white LEDs. CCT of white LEDs can be tuned between 12928K and 6509K. Chapter 4 is concerned with deposition of the QD on correlated colour temperature (CCT) LEDs. It shows that by using inkjet printing, the deposition area is controllable and has a good reproducibility. Chapter 5 is about using QDs to enhance the performance of planar Si solar cell. The enhancement in hybrid QD/Si solar cell is shown for two different types QDs. PbS core QDs shows the enhancement due RET, Luminescent down shifting (LDS), refractive index matching and scattering. In case of CdSe/ZnS (core/shell), the author optimised the QD layer thickness to get maximum Jsc enhancement. Chapter 6 is on hybrid photonic quasi crystal solar cell. 12 fold quasi crystals with two different air fill fraction was used and QDs deposition spin speed was also optimised to get maximum Jsc enhancement. Chapter 7 gives the summary of what has been determined as a result of this work and their impact. It also outlines the possible future works.

References

1. V. I. Klimov, "Spectral and Dynamical Properties of Multiexcitons in Semiconductor Nanocrystals," http://dx.doi.org/10.1146/annurev.physchem.58.032806.104537 **58**, 635–73 (2007).

2. A. P. Alivisatos, "Semiconductor Clusters, Nanocrystals, and Quantum Dots," Science (80-.). **271**, 933–937 (1996).

3. L. Qu and X. Peng, "Control of Photoluminescence Properties of CdSe Nanocrystals in Growth," J. Am. Chem. Soc. **124**, 2049–2055 (2002).

4. D. V. Talapin, J. H. Nelson, E. V. Shevchenko, S. Aloni, A. Bryce Sadtler, and A. P. Alivisatos, "Seeded Growth of Highly Luminescent CdSe/CdS Nanoheterostructures with Rod and Tetrapod Morphologies," Nano Lett **7**, 2951–2959 (2007).

5. L. Li, J. Hu, W. Yang, and A. P. Alivisatos, "Band Gap Variation of Size- and Shape-Controlled Colloidal CdSe Quantum Rods," Nano Lett. **1**, 349–351 (2001).

6. B. O. Dabbousi, J. Rodriguez-Viejo, F. V. Mikulec, J. R. Heine, H. Mattoussi, R. Ober, A. K. F. Jensen, and M. G. Bawendi, "(CdSe)ZnS Core−Shell Quantum Dots: Synthesis and Characterization of a Size Series of Highly Luminescent Nanocrystallites," J. Phys. Chem. B **101**, 9463–9475 (1997).

7. P. Reiss, J. Bleuse, and A. Pron, "Highly Luminescent CdSe/ZnSe Core/Shell Nanocrystals of Low Size Dispersion," Nano Lett. **2**, 781–784 (2002).

8. S. Kim, B. Fisher, H.-J. Eisler, and M. Bawendi, "Type-II Quantum Dots: CdTe/CdSe(Core/Shell) and CdSe/ZnTe(Core/Shell) Heterostructures," J. Am. Chem. Soc. **125**, 11466–11467 (2003).

9. X.-S. Wang, T. E. Dykstra, M. R. Salvador, I. Manners, G. D. Scholes, and M. A. Winnik, "Surface Passivation of Luminescent Colloidal Quantum Dots with Poly(Dimethylaminoethyl methacrylate) through a Ligand Exchange Process," J. Am. Chem. Soc. **126**, 7784–7785 (2004).

10. W. K. Bae, J. Joo, L. A. Padilha, J. Won, D. C. Lee, Q. Lin, W. Koh, H. Luo, V. I. Klimov, and J. M. Pietryga, "Highly Effective Surface Passivation of PbSe Quantum Dots through Reaction with Molecular Chlorine," J. Am. Chem. Soc. **134**, 20160–20168 (2012).

11. L. Xu, K. Chen, H. M. El-Khair, M. Li, and X. Huang, "Enhancement of band-edge luminescence and photo-stability in colloidal CdSe quantum dots by various surface passivation technologies," Appl. Surf. Sci. **172**, 84–88 (2001).

12. A. B. Greytak, P. M. Allen, W. Liu, J. Zhao, E. R. Young, Z. Popović, B. J. Walker, D. G. Nocera, and M. G. Bawendi, "Alternating layer addition approach to CdSe/CdS core/shell quantum dots with near-unity quantum yield and high on-time fractions," Chem. Sci. **3**, 2028–2034 (2012).

13. X. Cheng, S. B. Lowe, P. J. Reece, and J. J. Gooding, "Colloidal silicon quantum dots: from preparation to the modification of self-assembled monolayers (SAMs) for bio-applications," Chem. Soc. Rev. **43**, 2680–2700 (2014).

14. V. Brunetti, H. Chibli, R. Fiammengo, A. Galeone, M. A. Malvindi, G. Vecchio, R. Cingolani, J. L. Nadeau, and P. P. Pompa, "InP/ZnS as a safer alternative to CdSe/ZnS core/shell quantum dots: in vitro and in vivo toxicity assessment," Nanoscale **5**, 307–317 (2013).

15. X. Yang, D. Zhao, K. S. Leck, S. T. Tan, Y. X. Tang, J. Zhao, H. V. Demir, and X. W. Sun, "Full Visible Range Covering InP/ZnS Nanocrystals with High Photometric Performance and Their Application to White Quantum Dot Light-Emitting Diodes," Adv. Mater. **24**, 4180–4185 (2012).

16. K.-S. Cho, E. K. Lee, W.-J. Joo, E. Jang, T.-H. Kim, S. J. Lee, S.-J. Kwon, J. Y. Han, B.-K. Kim, B. L. Choi, and J. M. Kim, "High-performance crosslinked colloidal quantum-dot light-emitting diodes," Nat. Photonics **3**, 341–345 (2009).

17. Y. Shirasaki, G. J. Supran, M. G. Bawendi, and V. Bulović, "Emergence of colloidal quantum-dot light-emitting technologies," Nat. Photonics **7**, 13–23 (2013).

18. S. Coe, W.-K. Woo, M. Bawendi, and V. Bulović, "Electroluminescence from single monolayers of nanocrystals in molecular organic devices," Nature **420**, 800–803 (2002).

19. I. J. Kramer and E. H. Sargent, "Colloidal Quantum Dot Photovoltaics: A Path Forward," ACS Nano **5**, 8506–8514 (2011).

20. G. I. Koleilat, L. Levina, H. Shukla, S. H. Myrskog, S. Hinds, A. G. Pattantyus-Abraham, and E. H. Sargent, "Efficient, Stable Infrared Photovoltaics Based on Solution-Cast Colloidal Quantum Dots," ACS Nano **2**, 833–840 (2008).

21. K. E. Sapsford, T. Pons, I. L. Medintz, and H. Mattoussi, "Biosensing with Luminescent

Semiconductor Quantum Dots," Sensors **6**, 925–953 (2006).

22. P. D. Howes, R. Chandrawati, and M. M. Stevens, "Colloidal nanoparticles as advanced biological sensors.," Science **346**, 1247390 (2014).

23. V. I. Klimov, A. A. Mikhailovsky, S. Xu, A. Malko, J. A. Hollingsworth, C. A. Leatherdale, H.-J. Eisler, and M. G. Bawendi, "Optical Gain and Stimulated Emission in Nanocrystal Quantum Dots," Science (80-.). **290**, 314–317 (2000).

24. D. L. Dexter, "Two ideas on energy transfer phenomena: Ion-pair effects involving the OH stretching mode, and sensitization of photovoltaic cells," J. Lumin. **18**–**19**, 779–784 (1979).

25. M. Achermann, M. A. Petruska, S. Kos, D. L. Smith, D. D. Koleske, and V. I. Klimov, "Energy-transfer pumping of semiconductor nanocrystals using an epitaxial quantum well.," Nature **429**, 642–646 (2004).

26. S. Chanyawadee, P. G. Lagoudakis, R. T. Harley, M. D. B. Charlton, D. V Talapin, H. W. Huang, and C.-H. Lin, "Increased color-conversion efficiency in hybrid light-emitting diodes utilizing non-radiative energy transfer.," Adv. Mater. **22**, 602–606 (2010).

27. S. Chanyawadee, R. T. Harley, M. Henini, D. V. Talapin, and P. G. Lagoudakis, "Photocurrent Enhancement in Hybrid Nanocrystal Quantum-Dot $p-i-n$ Photovoltaic Devices," Phys. Rev. Lett. **102**, 77402 (2009).

28. U.S. Department of Energy, "LED lighting," http://energy.gov/energysaver/led-lighting.

29. M. D. Regulacio and M.-Y. Han, "Composition-Tunable Alloyed Semiconductor Nanocrystals," Acc. Chem. Res. **43**, 621–630 (2010).

30. X. Zhong, M. Han, Z. Dong, T. J. White, and W. Knoll, "Composition-Tunable ZnxCd1-xSe Nanocrystals with High Luminescence and Stability," J. Am. Chem. Soc. **125**, 8589–8594 (2003).

31. J. Kwak, J. Lim, M. Park, S. Lee, K. Char, and C. Lee, "High-Power Genuine Ultraviolet Light-Emitting Diodes Based On Colloidal Nanocrystal Quantum Dots," Nano Lett. **15**, 3793–3799 (2015).

32. M. A. Hines and G. D. Scholes, "Colloidal PbS Nanocrystals with Size-Tunable Near-Infrared Emission: Observation of Post-Synthesis Self-Narrowing of the Particle Size

Distribution," Adv. Mater. **15**, 1844–1849 (2003).

33. L. Protesescu, T. Zünd, M. I. Bodnarchuk, and M. V Kovalenko, "Air-Stable, Near- to Mid-Infrared Emitting Solids of PbTe/CdTe Core–Shell Colloidal quantum dots," ChemPhysChem **17**, 670–674 (2016).

34. X. Dai, Z. Zhang, Y. Jin, Y. Niu, H. Cao, X. Liang, L. Chen, J. Wang, and X. Peng, "Solution-processed, high-performance light-emitting diodes based on quantum dots," Nature **515**, 96–99 (2014).

35. Y. N. and M. I. and D. S. and M. S. and T. Mukai, "White light emitting diodes with super-high luminous efficacy," J. Phys. D. Appl. Phys. **43**, 354002 (2010).

36. Q. Sun, Y. A. Wang, L. S. Li, D. Wang, T. Zhu, J. Xu, C. Yang, and Y. Li, "Bright, multicoloured light-emitting diodes based on quantum dots," Nat Phot. **1**, 717–722 (2007).

37. P. O. Anikeeva, J. E. Halpert, M. G. Bawendi, and V. Bulović, "Electroluminescence from a Mixed Red−Green−Blue Colloidal Quantum Dot Monolayer," Nano Lett. **7**, 2196–2200 (2007).

38. W.-S. Song, S.-H. Lee, and H. Yang, "Fabrication of warm, high CRI white LED using non-cadmium quantum dots," Opt. Mater. Express **3**, 1468–1473 (2013).

39. H. M. Haverinen, R. a. Myllylä, and G. E. Jabbour, "Inkjet printing of light emitting quantum dots," Appl. Phys. Lett. **94**, 12–15 (2009).

40. K.-J. Chen, H.-C. Chen, K.-A. Tsai, C.-C. Lin, H.-H. Tsai, S.-H. Chien, B.-S. Cheng, Y.-J. Hsu, M.-H. Shih, C.-H. Tsai, H.-H. Shih, and H.-C. Kuo, "Resonant-Enhanced Full-Color Emission of Quantum-Dot-Based Display Technology Using a Pulsed Spray Method," Adv. Funct. Mater. **22**, 5138–5143 (2012).

41. Z. Luo, D. Xu, and S. T. Wu, "Emerging Quantum-Dots-Enhanced LCDs," J. Disp. Technol. **10**, 526–539 (2014).

42. J. Du, Z. Du, J.-S. Hu, Z. Pan, Q. Shen, J. Sun, D. Long, H. Dong, L. Sun, X. Zhong, and L.-J. Wan, "Zn–Cu–In–Se Quantum Dot Solar Cells with a Certified Power Conversion Efficiency of 11.6%," J. Am. Chem. Soc. **138**, 4201–4209 (2016).

43. M. A. Green, K. Emery, Y. Hishikawa, W. Warta, and E. D. Dunlop, "Solar cell efficiency tables (version 48)," Prog. Photovoltaics Res. Appl. **24**, 905–913 (2016).

44. M. Yuan, M. Liu, and E. H. Sargent, "Colloidal quantum dot solids for solution-processed solar cells," Nat. Energy **1**, 16016 (2016).

45. K. Masuko, M. Shigematsu, T. Hashiguchi, D. Fujishima, M. Kai, N. Yoshimura, T. Yamaguchi, Y. Ichihashi, T. Mishima, N. Matsubara, T. Yamanishi, T. Takahama, M. Taguchi, E. Maruyama, and S. Okamoto, "Achievement of More Than 25% Conversion Efficiency With Crystalline Silicon Heterojunction Solar Cell," IEEE J. Photovoltaics **4**, 1433–1435 (2014).

46. J. Tang and E. H. Sargent, "Infrared Colloidal Quantum Dots for Photovoltaics: Fundamentals and Recent Progress," Adv. Mater. **23**, 12–29 (2011).

47. D. L. Dexter, "Two ideas on energy transfer phenomena: Ion-pair effects involving the OH stretching mode, and sensitization of photovoltaic cells," J. Lumin. **18**–**19**, 779–784 (1979).

48. A. P. Alivisatos, M. F. Arndt, S. Efrima, D. H. Waldeck, and C. B. Harris, "Electronic energy transfer at semiconductor interfaces. I. Energy transfer from two-dimensional molecular films to Si(111)," J. Chem. Phys. **86**, 6540–6549 (1987).

49. S. Lu, Z. Lingley, T. Asano, D. Harris, T. Barwicz, S. Guha, and A. Madhukar, "Photocurrent induced by nonradiative energy transfer from nanocrystal quantum dots to adjacent silicon nanowire conducting channels: toward a new solar cell paradigm.," Nano Lett. **9**, 4548–52 (2009).

Chapter 2: Theoretical background and Literature review

2.1 Bulk semiconductors

The electronic structure of bulk semiconductors consists of multiple atomic orbitals giving rise to continuous energy bands. The highest occupied and lowest unoccupied band is termed as valence band and conduction band. When a photon is absorbed, an electron is excited from valence band to conduction band (Figure 2.1), the electron in conduction band is described by the charge e^-, effective mass m_e^* and the spin (s=1/2). The quasi particle hole with charge e^+, effective mass m_h^* and spin (s=1/2) is created in valence band on excitation of an electron. The energy required for excitation is given by:

$$E = E_g + E_{e,Kin} + E_{h,kin} \tag{1}$$

E_g is the bandgap energy, where band gap is the minimum gap between a conduction band and valence band. $E_{e,kin}(E_{h,kin})$ is the kinetic energy of electron (hole). As photon has a negligible momentum, only vertical transition can take place. Electron-hole pair interacts via columbic interaction to form another quasi particle exciton, which act as a single uncharged particle and can be characterised by their Bohr radius. The exciton Bohr radius (a_B^*) is determined by scaling Bohr radius of hydrogen atom to the ratio of semiconductor dielectric constant (ε) and effective carrier mass [1] as shown below:

$$a_B^* = \varepsilon \frac{m_0}{\mu_{eh}^*} a_0 \tag{2}$$

Where a_0 is a hydrogen Bohr radius and m_0 is the carrier mass of electron in hydrogen atom. The electron-hole reduced mass (μ_{eh}^*) is given by $\mu_{eh}^{*-1} = m_e^{*-1} + m_h^{*-1}$. Similar to hydrogen atom, the lowest ionisation energy for semiconductors is given by Rydberg energy (exciton binding energy):

$$R_y^* = \frac{e^2}{2\varepsilon a_B^*} \tag{3}$$

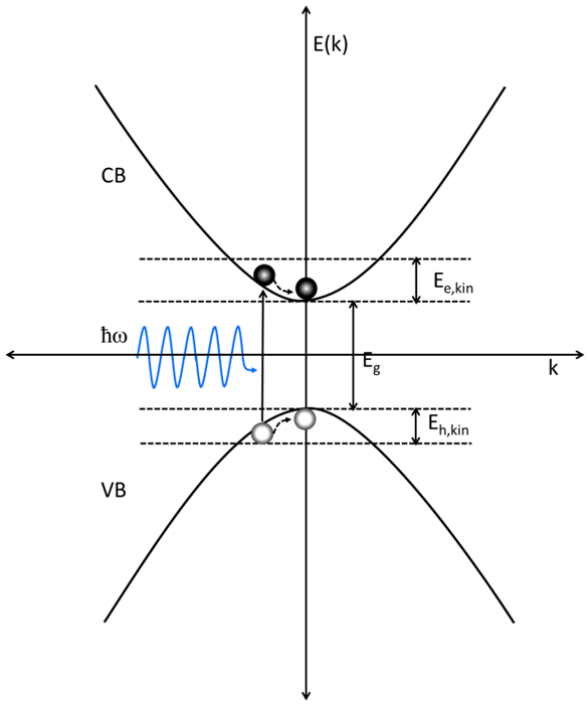

Figure 2.1: Shows an energy- k vector diagram for bulk semiconductors. On absorption of photon (ħω), an electron is excited from the conduction band (CB) to valence band (VB).

The exciton like elementary particle exhibits centre of mass motion with an effective carrier mass ($m_{exc}{}^{*} = m_e^* + m_h^*$). The exciton dispersion relation is given by:

$$E_{exc}(k) = E_g - \frac{R_y^*}{n^2} + \frac{\hbar^2 k^2}{2m_{exc}{}^{*}} \tag{4}$$

Where n is the principal quantum number taking integral value and ħ is reduced Plancks constant and k is exciton wave vector. If the exciton is created due to the absorption of photon then momentum (p= ħ k) is negligible. Therefore equation 4 can be rewritten as:

$$E_{exc} = E_g - \frac{R_y^*}{n^2} \tag{5}$$

2.2 Colloidal QDs

Colloidal Quantum Dots (QDs) vary in sizes from 2nm to 10nm, which is between the size of molecule and the bulk semiconductor. QDs exhibit the properties of both extremes, wider absorption spectra similar to a bulk semiconductor as well as narrow and efficient fluorescence such as molecular dyes. In addition, size dependent electronic and optical properties of QDs have

attracted researchers in various scientific domains. As the size of QD decreases, the energy spacing increases, hence making it possible to tune them in wide range of electromagnetic spectrum with single material composition. Since QD can be viewed as a large molecule, the properties of QDs are studied by adding atoms to core particle. This bottom-up approach has gained importance due to increase in computational power [2]. Alternative approach is top-down approach, where QD is viewed as bulk semiconductor with finite confinement in three dimensions. The quantum confinement effect becomes significant when QD size approaches the exciton Bohr radius. The exciton Bohr radius of certain bulk semiconductors are given in table 1. It can be observed that the bandgap increases with reduced exciton Bohr radius. The exciton Bohr radius is approximately the sum of electron and hole Bohr radius. For most of the semiconductors shown in table 1, electron has larger Bohr radius than hole. In this case, electrons experience a stronger confinement than hole. The degree of quantum confinement in QDs will dependent on their bulk counterpart. For example, PbTe QDs will experience higher degree of electron and hole confinement than CdSe with 3nm diameter. Bohr radius of electron, hole and exciton defines three confinement regimes. It experiences a weak confinement regime when a ($a^*_{e,B}$, $a^*_{h,B} < a$) is greater than electron bohr radius ($a^*_{e,B}$) and hole bohr radius ($a^*_{h,B}$) , where a is the radius of QDs. Intermediate confinement regime when a is between $a^*_{h,B}$ and $a^*_{e,B}$ ($a^*_{h,B} < a < a^*_{e,B}$) and a strong confinement regime when radius of QDs is less the electron and Bohr radius ($a^*_{e,B}$, $a^*_{h,B} > a$) .

The band gap of QDs can be determined using a particle in sphere model [3,4]. Mathematical details are omitted in this explanation but it shows the principal. The discrete energy levels for particle (electron and hole) confined in a spherical potential is given by:

$$E_{n,l} = \frac{\hbar^2 \beta^2_{n,l}}{2m^* a^2} \tag{6}$$

Where ħ is reduced Plancks constant, m^* is effective mass of electron or hole. $\beta_{n,l}$ is roots of a Bessel function, which has absolute values depending on principal quantum number ‘n’ and angular quantum number ‘l’.

Table 1: Band gaps, effective masses and Bohr radius of electron, hole and excitons in bulk semiconductors [4].

		$E_g(eV)$	m_e^*/m_0	m_h^*/m_0	Electron $a_{e,B}^*$ (nm)	hole $a_{h,B}^*$ (nm)	Exciton a_B^* (nm)
II-VI	CdS	2.48	0.25	0.6	1	<1	2
	CdSe	1.73	0.12	0.9	3	1	4
	CdTe	1.48	0.09	0.8	4	1	5
III-V	InP	1.34	0.073	0.45	7	1	8
	InAs	0.35	0.023	0.57	27	2	29
	InSb	0.17	0.012	0.44	59	2	61
IV-VI	PbS	0.42	0.087	0.083	10	11	21
	PbSe	0.28	0.047	0.041	26	29	55
	PbTe	0.31	0.034	0.032	56	48	104

The band gap of QD [5] is the sum of fundamental gap of the bulk with confinement energy of electron and hole.

$$E_{QD} = E_{bulk} + \frac{\hbar^2 \beta_{n_e,l_e}^2}{2{m_e}^* a^2} + \frac{\hbar^2 \beta_{n_h,l_h}^2}{2{m_h}^* a^2} \quad (7)$$

E_{QD} and E_{bulk} are the band gap of QD and bulk semiconductor. From the equation 7, it can be observed that the confinement energy scales with $1/a^2$, where a is a diameter of QD. The electron and hole are treated independently in the equation 7, this applies when the radius of QD is smaller than exciton Bohr radius (strong confinement). The coulombic attraction in QD is much larger than the bulk, however for strong confinement regime, the kinetic energy of electron and holes is even greater. Coulomb attraction can be neglected in this case. When the QD size is much larger than exciton Bohr radius and falls in weak confinement regime. The band gap of QD (equation 7) is corrected for coulombic attraction.

$$E_{QD} = E_{bulk} + \frac{\hbar^2 \beta_{n_e,l_e}^2}{2{m_e}^* a^2} + \frac{\hbar^2 \beta_{n_h,l_h}^2}{2{m_h}^* a^2} - E_C \quad (8)$$

Where E_C is the first order correction factor for coulombic attraction in QD. E_C is equals to $1.8e^2/4\pi\varepsilon a$ where 'e' is the elementary charge and ε is the dielectric permittivity of QD. From equations 6, 7 and 8, it can be seen that the band gap of QD increases with the decrease in size and discrete energy levels are formed at the edges of conduction band and valence band [6].

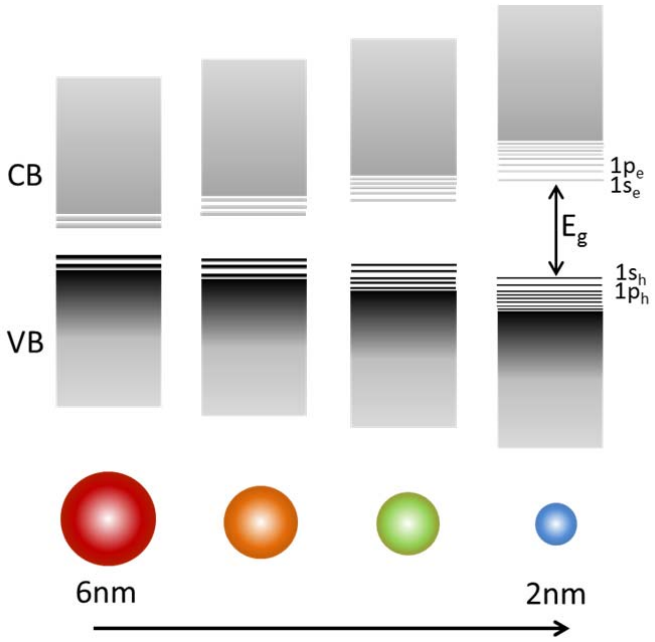

Figure 2.2: Schematic of quantum confinement effects on the energy level in QD with decrease in size [6].

Figure 2.2 shows the schematic of quantum confinement in different sizes of QD. As the size of the QDs reduces, it shows that inter band and intra band energy spacing level increases. The size dependent quantum confinement effects can be observed experimentally from the absorption and photo luminescence spectra of QDs. Figure 2.3 (a) shows the absorption spectra of core CdSe nanocrystals with diameter equal to 2.8nm, 4.1nm and 5.6nm. The first optical transition of QD is observed at the onset of absorption and from which the band gap of QDs can be estimated. The absorption peaks are at wavelengths of 600nm, 550nm and 500nm corresponding to the first optical transition of CdSe QDs with diameter of 5.6nm, 4.1nm and 2.8nm respectively. In accordance to theory, as the size of QDs decreases, E_g increases and the blue shift in first optical transition is observed. Inset in figure 2.3(a) is a high resolution transmission electron microscopy (TEM) image of 5.6nm QDs. Figure 2.3 (b) shows the normalised absorption and photo luminescence (PL) spectra of PbS core QDs with diameter 5.4nm, 3.8nm and 3.2nm. Similar to CdSe QDs, there is a blue shift in PL and absorption spectra of PbS QDs. The bandgap of PbS QDs (5.4nm) and CdSe QDs (5.6nm) are estimated from absorption spectra and compared to their respective bulk. Band gap energy (ΔE_g) increase for PbS QDs is higher than of a CdSe QDs, which can attribute to higher degree of confinement which arise from larger exciton Bohr radius (Table 1). Absorption spectra of QDs can show up to three optical transitions.

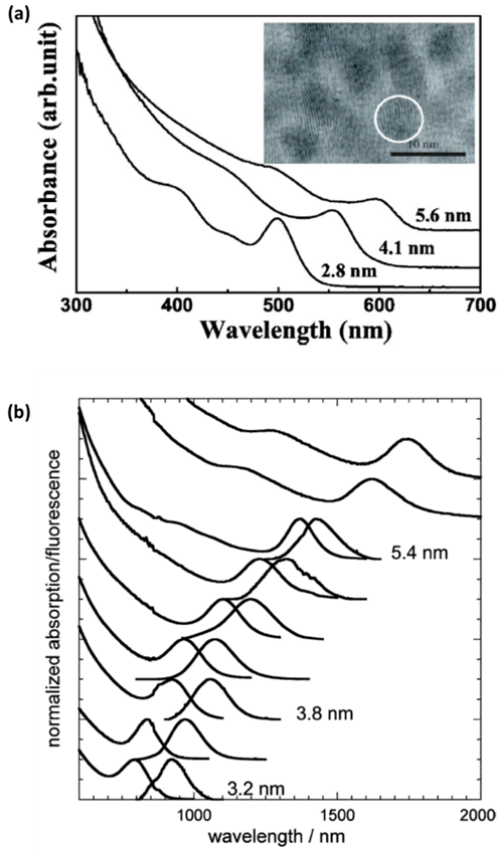

Figure 2.3: (a) absorption spectra of core CdSe nanocrystals with diameter 5.6nm, 4.1nm and 2.8nm. Inset shows the HRTEM image of 5.6nm diameter CdSe QDs [7]. (b) Absorption and photoluminescence spectra of PbS core QDs with diameter of 5.4nm, 3.8nm and 3.2nm [8].

From figure 2.3(a) and (b), only two optical transitions are visible. Although, particle in sphere model predicts the discrete energy level of QDs, there can be as much as 100% relative error from the experimental observation. The spherical model can be used to understand the basic photo physics of QDs but for more accurate predication, advanced treatment like multiband effective mass treatment [9] and tight binding model [10] should be considered. Experimentally up to eight optical transitions are resolved using fluorescence line narrowing [11,12]and photo luminescence excitation spectroscopy [9,12].

2.3 Core/shell QDs

Colloidal Quantum dots are chemically synthesised [13] and terminated with organic ligands for passivation. The ratio of surface atoms to core is higher in zero dimensional QD semiconductors. For 5nm PbSe QDs, about 40% of atoms are on the surface of QDs [1], which act as potential

charge trap for delocalised charge carriers. The termination of the surface atoms with organic ligands provides a certain degree of passivation. The drawback of organic ligands is incomplete passivation and photo instability. Another approach for passivating QDs is by using inorganic layer as cap (shell) layer. An epitaxial inorganic layer (few monolayers) is grown on to the surface of QDs [14]. Based on the shell layer, there is a relative offset between conduction band (and valence band) of the core and shell. If the conduction band of the core is less than the shell and valence band of core is higher than the shell, it is then called type I QDs (figure 2.4). In case of type1, both electron and hole are confined within the core. CdSe/ZnS [15] and CdSe/ZnSe [16] (core/shell) type 1 QDs have reported a high photoluminescence. Type 1 can serve as better light emitters due to reduced surface states and confinement of electrons-hole in the core. In type II core/shell QDs (figure 2.4), the valence band (and conduction band) of core is less than the shell. The photo excited electrons relax at minimum of the conduction band (in this case, core) and holes relax at maximum of the valence band (in this case, shell). The separation of electrons and holes for type II QDs have wide implications in photovoltaics [17] and exciton lasers [18]. Previously, the core multi shell QDs [19] with photoluminescence quantum yield as high as 85% [20] have been reported.

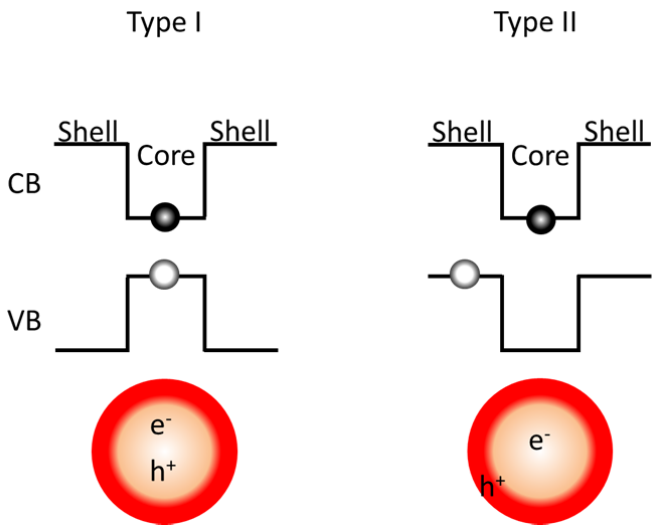

Figure 2.4: Shows the schematic and confinement of electrons and holes in type I and type II core/shell QDs

2.4 Colloidal quantum dots (QDs) for LEDs

Colloidal QDs are prepared via chemical synthesis [21–23] and have diameters less the Bohr radius of the bulk material. As discussed in section 2.2, quantum confinement effect can be used to tune the bandgap of QD. Depending on the core material either visible or infrared region of the

spectrum can be spanned. The visible region of the spectrum is covered by CdSe, CdSe/ZnS (core/shell), CdTe and CdTe/ZnS(core/shell) QDs and the infrared region of the spectrum is dominated by PbSe and PbS QDs. The photo luminescence quantum yield is the number of photons emitted to number of photons absorbed and is used to describe the performance of QDs. Near unity quantum yields have been shown in both CdSe/CdS [24] and CdTe [25] QDs, making them an ideal light emitters. In comparison with competing fluorescent organic dyes, QDs have broader absorption band. The absorption of QDs gradually increases towards the UV region of the spectrum, making them an excellent absorber. QDs have also shown to exhibit good thermal and photochemical stability. QDs can be excited electrically, optically or through resonant energy transfer (RET).

2.4.1 Electrically excited QDLEDs

The first demonstration [26] of electrical injection of QDs was established with polymer/ITO as hole transport layer and magnesium electrode as electron transport layer. The external quantum efficiencies (EQEs) of these QD LEDs were between 0.001- 0.01%, where EQE is the ratio of photons emitted to the charge (electron-hole) injected. The EQE of QD LED with semiconducting polymer was further improved to 0.22% [27] by using core/shell (CdSe/CdS) QDs. In above approach, the QD layer was used as both electroluminescence layer and transport layer. In Coe *et al.* [28] work, a monolayer of QDs was sandwiched between organic transport layers and the phase separation technique [29] was used to achieve a monolayer of QDs. Solution of QDs and organics were mixed together and spin casted on to the substrate, as the solvent in the mixer dries, the organic capped QDs are moved to the surface and it self-assembles. QD layer is used as electro luminescence layer in this case. 25 fold improvement in luminous efficiency (1.9 cdA^{-1}) with the EQE of 0.4- 0.5% was reported. Using similar approach, the EQE was further improved by 1-2% [29,30]. The physical process behind enhancement of the EQE was due to direct electrical injection and resonant energy transfer [31]. The contact printing [32] approach was demonstrated for fabricating single and multi-coloured QD LEDs. QDs were spin coated on top of PDMS (polydimethylsiloxane) mould, which was then transferred to substrate with either hole or electron transport layer. The direct electrical injection was performed by using organic hole and electron transport layer. White LED consist of red emitting QD (CdSe/ZnS), green emitting QD (ZnSe/CdSe/ZnS) and blue emission organic hole transport layer was demonstrated using contact printing technique. An advantage of contact printing over phase separation technique is that, it is independent of QDs and organic layer. By using contact printing [33], the EQE of 2.7% (orange emission) and 2.6% (red emission) was achieved. The deposition of QD at precise area has a huge impact on QD display and solid-state lighting.

The true potential of QDs is not exploited if the transport layer is based on organic polymers. It would be ideal to use photo stable and high charge mobility inorganic transport layer over organic

transport layer. The QD LED based on inorganic layer was demonstrated [34], where monolayer of QDs was deposited on top of the p-GaN and then n-GaN layer was grown over QDs. This architecture resembles the p-i-n structure where charges are injected via doped GaN layer and electroluminescence is achieved through CdSe/ZnS (core/shell) QDs. The EQE of this device was found to be relatively low (0.001-0.01%). Nevertheless, the key advantage of this QD LED based on inorganic transport is that the electron and transport layer are both stable in an ambient atmosphere. Improvement of this architecture was achieved using metal-oxide as a transport layer for QD LEDs. In [35], few monolayers of ZnCdSe QDs were sandwiched between NiO and ZnO: SnO_2 charge transport layers. The EQE obtained with metal-oxide transport layer was 0.1% [35] which was later improved to 0.2%. Free carrier concentration in both metal-oxide layers should be kept similar to avoid charge imbalance. Charge imbalance was one of the delimiting factor in direct electrical injection of QDs. Excess electron or hole carriers caused the QD to charge, which then relaxes through non-radiative mechanism via auger recombination [36]. The QD LED efficiencies based on inorganic transport were an order of magnitude less than that of QD LEDs with organic transport. The advantage of organic transport layers over inorganic transport layer is the direct electrical injection and the existence of exciton energy transfer from organic transport to QDs [31].

As a consequence of many years of study, QD LED has shown improvement in the EQE and luminescence. This improvement was due to increase in photo luminescence quantum yield of QDs and engineering the charge transport layer. In spite of continuous progress, the difference in electron and hole injection has limited the EQE to ~2%. Rather than using organic layers or Inorganic layers, hybrid charge transport layer was considered. Using hybrid organic and inorganic charge transport layer, the EQE of 7.3% [37] (for 628nm) and 5.8% [37] (for 515nm) have been achieved. Quantum yield of QDs was further optimised to achieve a EQE of 18.5% [38] and 20.5% [39] for QD LEDs. The record EQE QDLED architecture consists of ITO/organic transport layer/QD (40nm)/PMMA(6nm)/ZnO(150nm)/Ag. The electron mobility of ZnO nanocrystal particles is three orders of magnitude higher than of a organic transport layer. Excess injection of carriers degrade the QDs and reduces the lifetime of QDLEDs. High EQE (20.5%) was demonstrated by using thin insulating layer between electron transport layer and QDs to maintain charge balance with injected holes. Best electrically injected QDLED has the EQE above 18.5% [38,39], luminescence of 218,000 cdm^{-2} [37] and lifetime of 300,000 hours [40] which is catching up with organic LEDs performance. Therefore, electrically injected QD LEDs are also finding their way into display market and solid-state lighting. Full colour QDs display [41] has been demonstrated using contact printing technique. QD LEDs on wearable platform can also have a huge applications in consumer market, as wearable white QD LEDs [42] have already been demonstrated using intaglio transfer printing.

2.4.2 Optically excited QD-LEDs

Direct electrical injection of QDs is an interesting phenomena, which has recently reached the peak when achieving performance comparable to OLEDs [43]. Record EQE of QD LED through direct electrical injection is 18.5% [38] - 20.5% [39], which is far behind the highest reported InGaN blue LEDs with the EQE of 85% [44]. The photoluminescence quantum yield (QY) of QDs has reached near unity. One approach to make use of high QY QDs is to optically excite the QDs. In this case, QD absorbs high-energy photons and emits them via stoke shift. First [45] QD down conversion LED was proposed by exciting at 590nm and emitting QD in polylaurylmethacrylate matrix via blue GaN LED. Similar approach was used to produce white LEDs either by combining two, three or more different types of QDs [46,47]. Using QD as an alternative to yellow phosphor (YAG: Ce3+, cerium doped yttrium aluminium garnet) in white LEDs, high CRI above 95 % [48] can be obtained. The colour rendering index (CRI) denotes the ability of light source rendering the true colour of illuminated object with respect to daylight. From section 2.4, it can be seen that efficient transport layer is a need for direct electrical injection. The difference in carrier injection from hole and electron transport was major step back in commercialisation of QD LEDs. This drawback is overcome in the case of down conversion QD LEDs. QDs have absorption below their emission wavelength and keep increasing towards the UV region of the spectrum. By using blue or UV LEDs, it is possible to optically excite QDs with emission in visible or infra-red spectrum. Broad absorption of QDs has wide applications in solid-state lighting and back lighting of LCD displays. Research success of QD display [49]was demonstrated with 46 inch LCD panel backlight with QD LEDs in which 96 cool white QD LEDs were used for backlighting and QD LEDs vertical structure consisted of InGaN blue LED encapsulated with QDs (red and green) silicone mixture. On comparison with displays made from phosphors, the QDs based display showed saturated colour with 19% wider coverage in NTSC (National Television Systems Committee) standard of CIE 1931 colour space. QDs based [50] display or lighting can be categorised as QD edge optic, QD film and on chip QD LED . In QD edge optic and film technology, QDs are kept away from the source (blue or UV LED). On chip QLED, QDs matrix mixture (QD and silicone/epoxy) is deposited on to the surface of the LED (blue or UV). All these three approaches for QD integration can be adapted to lighting and displays.

In 2013, first commercial QDs backlight display was launched by Sony along with QD vision as Sony Bravia Triluminous televisions which utilised integrated QD edge optics. Recently, Samsung and 3M (along with Nanosys Inc) have launched displays based on QDs. QD based solid-state lighting [51] and displays are beginning to reach the consumer market. However, the efficiency of colour conversion reported is lower than QY of QDs. In this thesis, the author has demonstrated that by using efficient hybrid QD/LED architecture, the colour conversion quantum yield of QDs was increased above 15%.

2.5 Colloidal quantum dots (QDs) for Solar cells

The absorption of QDs can be tuned from visible to infrared spectrum, which makes QDs a suitable photovoltaic material. PbS and PbSe QDs have obtained ample attraction in the field of photovoltaics due to the wide tunability from visible to infrared region of the spectrum. QDs based solar cells have been reported in these architectures are QDs blended in conjugated polymer, QD schottky solar cell, QD heterojunction solar cell or QD sensitized solar cell. When QDs is blended with conjugated polymer solar cells, the light is absorbed in both QDs and organic polymer; and charges are separated at the interface of QDs and polymer. As a result, electrons are in QDs and holes are in a polymer [52] where electrons are transported through the network of QDs and holes are transported through conjugated polymer. Below optimum concentration of QD, the photoconductivity increases with the concentration of QDs in QD/polymer blend. Highest efficiency reported for QD-polymer hybrid photovoltaics is <6% [53,54]. The PbS and PbSe QDs form p-type semiconductor when treated with butylamine and ethanedithiol respectively [55,56]. The PbSe and PbSQDs are predominantly used in QD solar cells and to form schottky contact with low work function metals like Lithium floride (LiF), calcium (Ca), aluminium (Al) and magnesium (Mg) [57–59]. Highest reported power conversion efficiency (PCE) for QD schottky solar cell is 5.2% [60]. One architecture of heterojuction solar cell [61] is FTO (fluorine doped tin oxide) glass coated with TiO_2 nanoparticle, which are then coated with QDs (preferably PbS or PbSe) followed by metal contact. QDs are attached to TiO_2 using organic linker molecular and the conductivity of organic hole enhances the electron transport. QDs are deposited using layer by layer approach [62]. The required thickness was obtained by removing organic ligand and spin coating the QDs. QDs acts as light collector and hole transport layer; and TiO_2 nanoparticle act as the electron collector. Solar cell efficiency of this QD heterojunction solar cell was found to be 3.5% which was later improved to 7.4% [63] through passivation of QDs. The performance of QD heterojunction solar cell was further enhanced to 9.2% [64] using inverted pyramid light trapping structure. The QDs sensitised solar cell is similar to dye sensitised solar cell, where QDs replaces the dye and are chemically adsorbed by semiconductor (TiO_2, ZnO and SnO_2).

Record efficiency of QD based solar is 11.6 % [65] whilst single junction silicon solar cell and GaAs solar cell have efficiencies of 25.6% [66] and 29% [67] respectively. QDs have high absorption cross-section compared with bulk single junction solar cell and have shown photoluminescence quantum yield above 95 % [24]. Therefore, an alternative approach to efficiently use QDs is to use it as down conversion layer. The light is absorbed in QD layer and down shifts the photons at wavelengths where the EQE of bulk silicon solar is high. Another interesting approach is to use QD and bulk solar architecture by employing non-radiative resonant energy transfer from QDs to bulk of solar cells. The RET and applications of solar cells are discussed in section 2.6.

2.6 Resonant energy transfer

Resonant energy transfer (RET) is an electronic excitation transfer process from excited donor to acceptor at ground state. RET is a non-radiative process occurring within short life time of excited state [68]. Figure 2.5 shows the mechanism of RET process, which involves absorption of photon (energy $\hbar\omega = E_{D,n3}$) and excitation of electron at donor. The excited electron then relaxes thermally to the lower excitation state ($E_{D,n0} < E_{D,n3}$). The excitation is transferred to an acceptor with possible electronic transition($E_{A,n1} = E_{D,n0}$). The excited electron in acceptor then relaxes thermally and annihilates emitting of a photon.

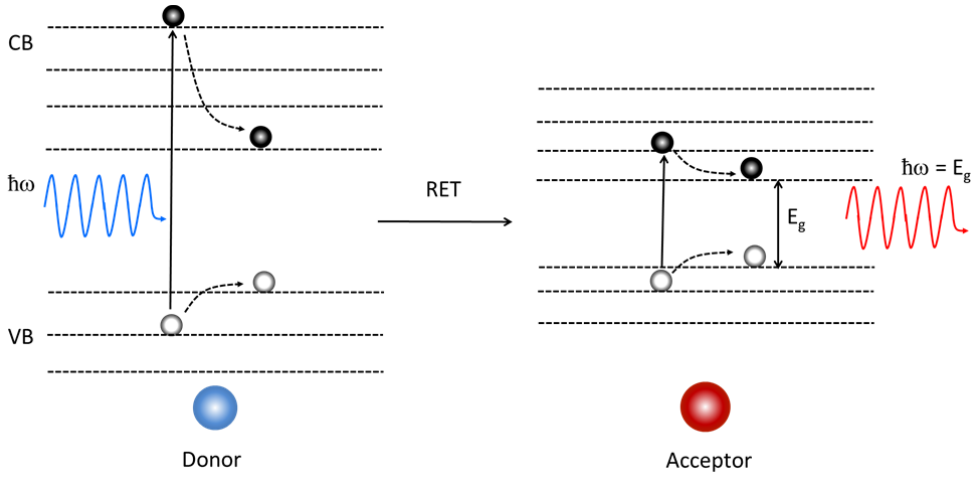

Figure 2.5: Schematic of RET mechanism from larger QDs to smaller QD.

The trivial radiative transfer mechanism involves the absorption of photon by donor and band gap emission of donor, which is then re-absorbed by the acceptor and a photon is emitted. Unlike radiative transfer, there is no photon exchange between donor and acceptor in RET mechanism, making it faster excitation transfer mechanism than a radiative transfer. RET was introduced by Förster in molecular systems, which involved dipole-dipole transfer between donor and acceptor molecule. The RET transfer rate between them is given by [68] [71]:

$$k_{RET} = \frac{1}{\tau}\left(\frac{R_F}{R}\right)^p \qquad (9)$$

Where τ is the excited lifetime of donor in absence of RET transfer and R is the space between molecules. Förster radius (R_F) is the distance at which RET transfer efficiency is equal to 50%. $R_F$is a system parameter depending on the quantum yield of donor and spectral overlap between donor emission and acceptor absorption. RET transfer rate follows distance power

dependence [69]and p denotes the dimensionality of acceptor molecules and p=6 for dipole –dipole coupling. It can also be extended to array of acceptor molecules, for dipole to layer of acceptor molecules (p=4) fourth power of distance has been observed [69,70]. RET transfer rate from layer of donor to layer of acceptor has shown to have square power (p=2) dependence on the distance [69,70]. Although, this theoretical approach of RET was limited to molecular systems, it still can be extended to QDs based systems. Energy transfer rate from QD donor (smaller QDs) to QD acceptor (larger QDs) in mixed QD film followed R^6 dependence [71], where R is the distance between QD donor and QD acceptor. Similarly, RET transfer rate from layer of dipole (InGaN Qw) to layer of QDs follows R^4 dependence [72].

2.6.1 RET based hybrid LEDs

Theoretical prediction of using a non-radiative RET to pump luminescent organic was proposed by Agranovich *et al.* [73,74]. They predicted by using hybrid inorganic/organic heterostructures, it is possible to obtain fast (100ps) excitonic transfer from inorganic donor to organic acceptor. Excitionic transfer via RET was an order magnitude faster than radiative transfer. Experimental demonstration of RET in organic light emitters [75] was achieved by a non-radiative pumping of F8DP (blue emitting polymer) with a UV emitting InGaN QW. At the same time frame, a non-radiative energy transfer from ZnO QWs to organic over layer was reported [76]. Non-radiative RET pumping of QDs was demonstrated by Achermann *et al.* [72,77]. RET pumping of QDs was achieved by spin coating the monolayer of CdSe/ZnS QDs on to the surface of InGaN LEDs. The LED structure [77] consists of p-GaN/GaN(10nm)/InGaN(3nm)/n-GaN(3nm) and its respective contact electrodes. On electrical injection, the electron-hole pairs from InGaN QWs are transferred non-radiatively to CdSe/Zns QDs. The limitation of this practical QD hybrid RET LED is that the acceptors QDs are separated from the donor QW by 3nm n-GaN layer. As an alternative methodology to this approach, Chanyawadee *et al.* [78] showed QDs acceptors can be bought close to QWs donor via etching QWs and depositing QDs within etched mesa. The LED architecture from bottom to top consists of sapphire substrate/n-GaN/MQWs (InGaN/GaN)/p-AlGaN/P-GaN and its respective contact electrodes at p-GaN and n-GaN layer. Using reactive ion etching, elliptical slots were etched into the LED stack, penetrating into p-GaN/p-AlGaN/MQWs. CdSe/CdS rod shaped QDs were drop casted into the etched mesa. This hybrid LED achieved 82% RET transfer efficiency due to close proximity of donor (QWs) and acceptor (QDs). The efficiency of RET transfer for hybrid devices (QW to organic layer or QDs) depend on the temperature [79,80] and exciton dimensionality (localised or free exciton) [79]. It was observed that free excitons can undergo RET transfer within an order of magnitude higher than of a localised excitons. Rinderndermann *et al*. [79] suggested by engineering the exciton dimensionality and in plane wave vector of exciton, it is possible to enhance RET transfer through QWs. The exciton dimensionality of QWs can be tuned by adjusting epitaxial growth conditions of QWs.

2.6.2 RET based hybrid photovoltaics

The concept of electro-hole pair generation in semiconductor layer through RET was visualised by Dexter in 1979 [81]. Hybrid photovoltaic structure consists of metal-semiconductor schottky solar cell embedded in organic layer (Figure 6.7 (a)). The organic layer serves as a light absorber and generated electron-hole pair are transferred to semiconductor layer via a non-radiative RET process. To Dexter's theoretical prediction, a non-radiative energy transfer from pyrene to silicon [82] and pyrazine to GaAs was observed [83]. In both configurations, when an organic molecule was placed near the semiconductor surface (Figure 6.7 (b)) an accelerated decay in fluorescence was observed indicating the existence of non-radiative transfer channel. Due to the theoretical report [73,74] on RET transfer from semiconductor QW to organic layer, hybrid organic/inorganic structure has gained increased attention in the field of LEDs and solar cells. RET based hybrid photovoltaics as envisaged by Dexter is a donor material, absorbs the entire (or percentage of) incident photon and generated excitons are then transferred to acceptor through a non-radiative RET mechanism. The exciton dissociation can take place at donor/ acceptor interface or at acceptor site which is then collected at respective electrodes. It is worth noting that it is beneficial for an acceptor to absorb photons and contribute to photo current. On basis of this configuration, various schemes have been proposed in hybrid photovoltaics.

One such scheme of RET based hybrid PVs is by using amorphous-silicon polymer hybrid solar cells [84]. In this, nanostructured amorphous silicon form heterojunction with either P3HT or MEH-PVV organic polymer (Figure 6.7 (d)). On photon absorption in P3HT (or MEH-PVV), the generated excitons are transferred to amorphous silicon through non-radiative transfer. The transferred exciton dissociates at organic/amorphous silicon interface, followed by injection of holes into the organic polymer layer. The reported performance of the solar cell was poor due to inefficient hole transport from an amorphous silicon. Nevertheless, this report was one of early implementation of RET based hybrid PVs.The concern of this thesis is to use QDs as light absorbers. Colloidal QDs for PVs was shown in section 2.5 and in this section and the discussion was limited to RET transfer from QDs to semiconductors.

The evidence of RET from QDs to buried QW was first demonstrated [85] between PbS QDs and InGaAs QW (Figure 6.7 (c)). Epitaxial InGaAs is buried 3nm below the GaAs surface and monolayer of PbS QDs is then deposited on top of GaAs. The band gap of PbS QDs was chosen such that there was a direct RET to InGaAs and there is no transfer to the surface of GaAs. PbS QDs and InGaAs QW have peak photo luminescence of 965nm and 1100nm respectively; while GaAs photoluminescence is centred at 873nm. RET transfer efficiency of 30% from PbS QDs to InGaAs QW was achieved. RET efficiency of 60% was estimated for unity quantum yield QDs. The existence of RET transfer from small PbS QDs to large PbS QDs in QD ensemble was also

demonstrated. Similarly, a non-radiative RET transfer for smaller CdSe QDs to large CdSe QDs for monolayer and bilayer assemblies was reported [86].

Hybrid QD/patterned p-i-n structure [87] that employs RET scheme (Figure 6.7 (e)), shows significant boost in photocurrent providing a new route to photovoltaics. Using molecular beam epitaxy (MBE), p-i-n heterostructure was grown on GaAs substrate. The p-i-n structure from bottom to top consist of n^+-GaAs/i-AlGaAs(100nm)/i-MQW/i-AlGaAs(100nm)/p^+-AlGaAs(500nm)/p^+GaAs(250nm). Multiple Quantum wells (MQWs) consist of 20 periodic GaAs QW (7.5nm)/AlGaAs barrier (12nm). Focused ion beam (FIB) was used to pattern 1.4μm deep gratings over an area of 80×80μm^2. Patterned gratings have a width and pitch equal to 570nm and 1.5µm respectively. CdSe/CdS QDs are then drop-casted into the patterned p-i-n heterostructure. From time resolved photo-luminescence (TRPL) measurement of GaAs MQW before and after hybridisation, they observed increase in PL rise time. Non-radiative transfer from QDs to MQWs causes an additional intermediate process to the direct excitation of QW. The rise time increase can also be due to intermediate radiative transfer. Fast decay of CdSe/CdS QDs in hybrid/ patterned p-i-n heterostructure to CdSe/CdS QDs on glass substrate confirms the existence of a non-radiative RET. From the decay dynamics of CdSe/CdS QDs on glass and hybrid/patterned p-i-n heterostructure, RET transfer efficiency of 79% is estimated between CdSe/CdS QDs and GaAs QWs. Controlled flat p-i-n heterostructure was also fabricated and the decay dynamics of QDs remained unaltered in a hybrid QD/ flat p-i-n heterostructure. 40µm spot of 400nm laser excitation was used to measure the photocurrent of hybrid QD/patterned p-i-n heterostructure and QD/flat p-i-n hetrostructure. Six fold enhancement of the photocurrent was observed in hybrid QD/patterned p-i-n heterostructure. From TRPL measurements, pumping of QWs through a non-radiative RET process is 10 times faster than a radiative transfer indicating RET is a dominant pumping mechanism for hybrid QD/patterned p-i-n heterostructure.

Silicon solar cells are the dominant technology in solar industry, efforts have been taken to create RET based Si solar cells. Hybrid QD/Si solar cell has the leverage of both worlds; high absorption of QDs and maturity of silicon technologies. The photo current enhancement in silicon nanowire was demonstrated [88] by non-radiative RET from adjacent layer of QDs (Figure 6.7 (f)).The choice of QDs was 2.5nm core PbS QDs with peak emission at 1100nm. This particular PbS QDs was chosen to absorb the photons between UV- mid IR spectrum. 200nm thick QD layer on top of Si Nanowires provided increase in absorption cross section. The generated excitons are then transferred non-radiatively to nanowires with an efficiency of 15-38%. RET from QDs to bulk silicon would be beneficial to existing silicon solar cells, and have been demonstrated using CdSe/ZnS [89] (Figure 6.7 (g)) and PbS QDs [90] (Figure 6.7 (h)). In hybrid CdSe/ZnS – Si structure [89], RET rate is ~8 times faster than a radiative decay of CdSe/ZnS QDs, achieving RET efficiency of 65%. The estimated separation distance between donor (CdSe/ZnS QDs) and acceptor (Si) is 4.4nm.

Different schemes used in RET based solar cells have been discussed above. The Figure 2.6 shows the summary of RET based hybrid photovoltaics. In all these cases, there are certain amount of electron-hole pairs which undergo a non-radiative transfer. These electron-hole pairs annihilate emitting photons. These photons can be absorbed by the acceptor and can contribute to the photo current. Therefore, QDs can also serve as mere down conversion layer, down converting high energy photons to low energy where the EQE of solar is high thus improving the solar cell efficiencies.

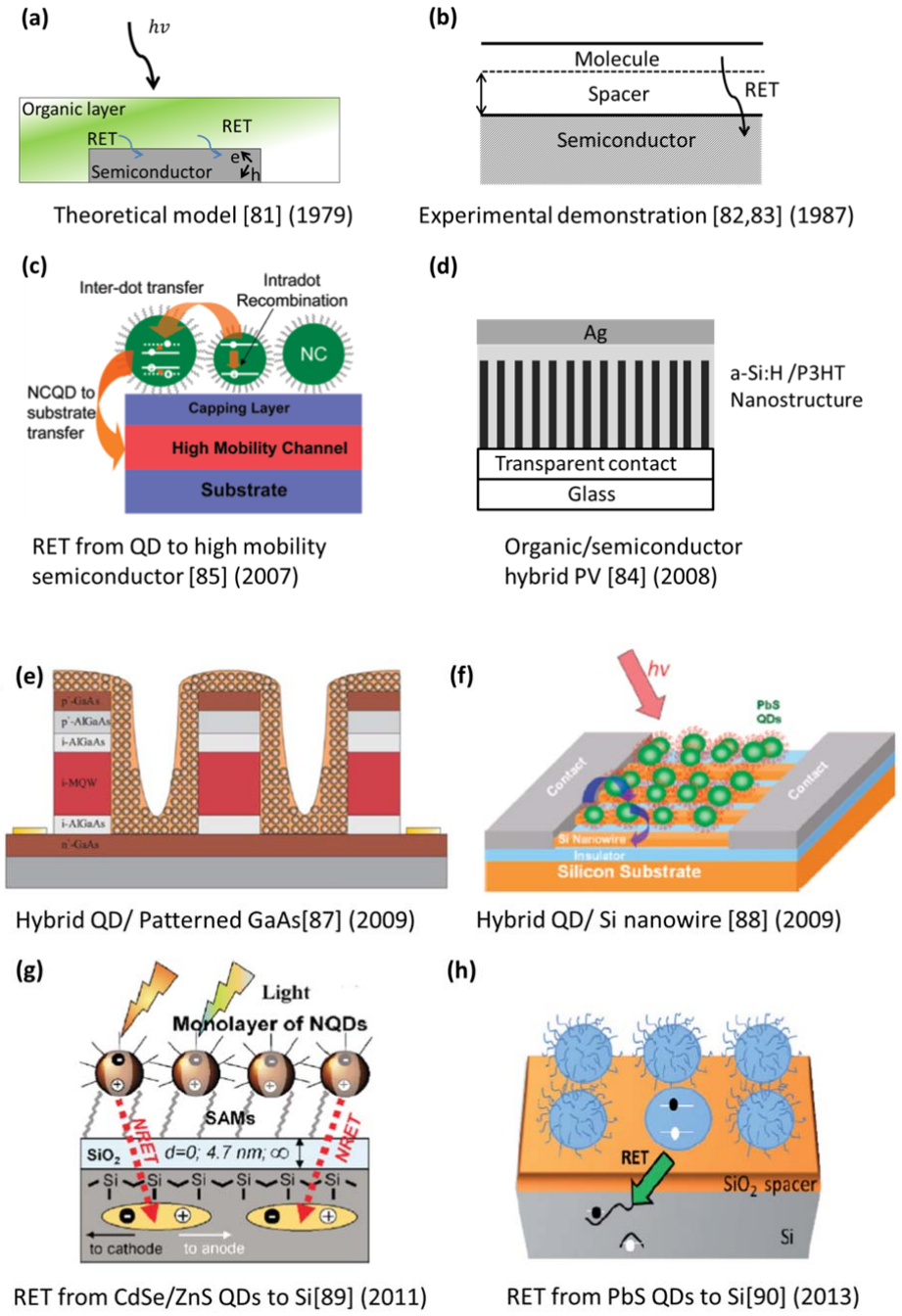

Figure 2.6: RET schemes for hybrid photovoltaics.

2.7 Photonic crystals

In this section, the reader will be introduced to photonic crystals (PhCs) and photonic quasi crystals (PQC) will be discussed. The PQC lattice configuration will be described and the section will end by concluding on the type of photonic crystal lattice used in this study.

2.7.1 Photonic Crystals

Assuming homogeneous material, photonic crystals (PhCs) are periodic perturbation of permittivity of material either in one, two or three dimensions. When these perturbations are in order of wavelength then it can interact with light and provide a new platform for optical devices. PhC has gained the interest of optics community and has found applications for waveguides, lasers and LEDs. The propagation of light is PhCs is analogous to electrons motion in semiconductors. In case of crystalline semiconductors, periodic lattice introduces gaps for electron and forbids them to move in certain directions for certain energies. If the gap extends in all possible direction, it would result in complete electronic band gap. The common example for band gap in semiconductor is between the conduction band and valence band. Similarly, the 3D photonic band gap can be constructed for material inhibiting the propagation of electromagnetic wave in all possible directions. For semiconductor, the allowed energy levels for electron are given by eigen values of time–independent Schrödinger equation. For photonic crystals, it is given by Maxwell equation [91]:

$$\nabla \times \left[\frac{1}{\varepsilon(r)} \nabla \times H(r)\right] = \left(\frac{\omega}{c}\right)^2 H(r) \tag{10}$$

Where ω is the angular frequency and c is free space speed of light. $\varepsilon(r)$ is the permittivity distribution with space, hence it is possible to solve equation computationally for infinite variations of permittivity in a medium. The possible eigen values is given by $\left(\frac{\omega}{c}\right)^2$. From Magnetic field H(r), the electric field E(r) can be obtained by using Maxwell equation. Alternatively, it can be solved directly for electric field and is written in the form of:

$$\nabla \times \nabla \times E(r) = \left(\frac{\omega}{c}\right)^2 \varepsilon(r) E(r) \tag{11}$$

In case of periodic variations of permittivity like PhCs, the electric and magnetic field in Maxwell equation can be written as:

$$H_k(r) = e^{ik\cdot r}u_k(r) \quad u_k(r) = u_k(r+R) \tag{12}$$

$$E_k(r) = e^{ik\cdot r}v_k(r) \qquad v_k(r) = v_k(r+R) \tag{13}$$

These are nothing but plane waves multiplied by periodic functions ($u_k(r)$ and $v_k(r)$) of lattice. When adding lattice vectors (R) to periodic functions, the state of the system is unchanged. This state is known as a bloch state according to Bloch's theorem. By solving Maxwell equation 11 or 12 for different values of k vector in a PhC lattice, it leads to redundant values in mode frequencies($\omega(k) = \omega(k+R)$) owing it to its periodicity. The Maxwell equation can also be solved for non-redundant values of k within the first Brillouin zone. This can further be reduced to smallest area called irreducible Brillouin zone when it exhibits rotational symmetry within the first Brillouin zone. It can be concluded that by solving Maxwell equation for different values of k within irreducible Brillouin zone, the dispersion relation of PhCs can be deduced in other words, the band diagram and their corresponding band gaps. In same way, electric field that exists within the PhC structure can also be calculated.

2.7.2 Photonic Quasi Crystals

Photonic quasi crystals (PQC) possess long range order and short range disorder. Photonic quasi crystal with ten-fold symmetry was first reported by Shetchman *et al.* [92] in aluminium-manganese alloy. The typical symmetries of PQC are 2, 4 and 6 but it can also acquire high order symmetry like 5,9,10 and 12 or more. The photonic quasi crystal used in this thesis is 12-fold quasi crystals generated by random -stampfli inflation rule [93]. First parent dodecagonal cell with 6 squares and 12 triangles is created by tessellation of squares and triangles. The parent cell is then inflated by a factor of $2+\sqrt{3}$. Offspring decagonal cell are placed within the parent cell, such that the centre offspring coincide with vertices of parent and sides running perpendicular to the tile edges. The gaps between offspring are filled with square and triangles; the gap between three offspring dodecagonal is filled by triangle and the gap between four offspring dodecagonal is filled by three triangles and square. Figure 2.7 shows the construction of 12-fold quasi crystal from parent dodecagon.

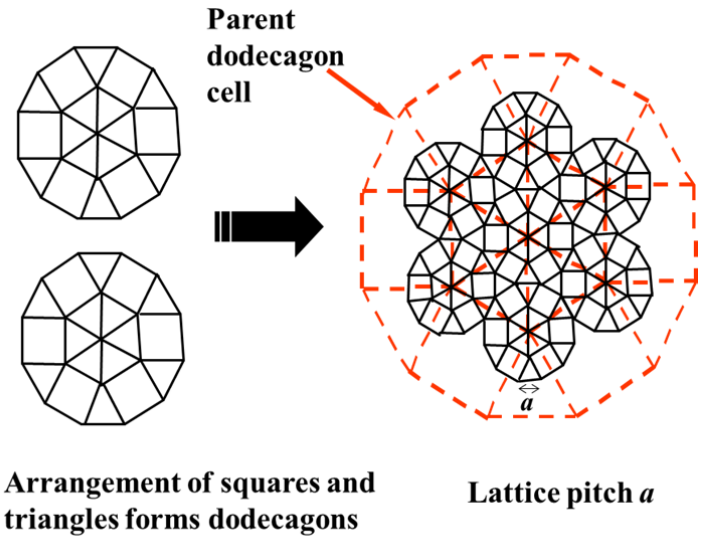

Figure 2.7: Random-stampfli inflation methods to create 12-fold photonic quasi crystal [94]

2.7.3 PQC LEDs

In planar LEDs, more than 90% [95] of light generated is trapped as guided modes within the high refractive index of GaN (n~2.5) due to total internal reflection. Surface roughening [96] was primarily used for light extraction. As an alternative to this approach, PhCs were used to extract the light efficiently from LEDs. For efficient light extraction, the PhCs should be able to extract all the guided modes coming from all azimuthal directions. The triangular and square lattice has shown to extract guided modes in LEDs only from certain direction due to their lattice symmetry [97]. For omnidirectional light extraction higher order symmetry like quasi crystal should be considered. It was experimentally [98] shown that light extraction in LEDs increased with increasing lattice symmetry from triangular PhCs to octagonal PQC and to 12-fold PQC. The pitch and air fraction dependence on 12-fold PQC LED was investigated [99], for three pitches of 450nm, 550nm and 750nm. It was observed that pitch of 750nm with air fraction of 30%, yielded the highest total light extraction. The 750nm pitch PQC LED reported had 5% error in hole diameter due to the exposure via e-beam lithography. The hybrid PQC/QD LED with pitch of 700nm and hole diameter of 350nm lattice configuration was chosen for this work.

The PQCs (or PhCs) in LEDs can be categorised with respect to position of QWs. For example, as shallow PQC, deep PQC or buried PQC. Shallow PQCs and buried PQCs have been reported through numerous publications whereas; deep PQCs suffered from least interest due to plasma etching of QWs which degrades the performance of LEDs. The thesis focuses on bringing QDs close to multiple quantum wells (MQWs) to benefit from RET. The proposed hybrid LED in this work is 12-fold PQC with 700nm pitch 350nm hole diameter etched into MQWs and hybridised

with suitable QDs. The main challenge of this configuration would be to minimise the surface states, which arises due to plasma damage.

2.7.4 Photonic crystals in solar cells

Solar cell performance has reached new heights in efficiency reaching 29% for single junction and 38.8% for multi junction terrestrial solar cells [67]. Si solar cells have the record efficiency of 25.6% [66] and commercial cells between 15% and 20%. The efficiency of solar cell is below thermodynamic limit of solar cell. By controlling the light at nanometre and micrometre scale along with advancements in material can lead to solar cell efficiencies between 50%-70% [100]. Some of the proposed nanostructures [101] are used at front, rear and as the absorbing layer of solar cells. Pyramids at the surface are most adapted light trapping structure to increase the absorption of solar cell. Other strategies like nanowires [102], high refractive index nanostructures [101,103] and nano cones [104,105] have also been employed. The nanostructures at rear act as back reflector, for improving the absorption of thin film Si solar cell for longer wavelengths. For metallic grating with DBR showed enhancement of ~135% for the wavelengths between 1000nm - 1200nm [106]. Nano cones [107] and random surface [108], when used as back surface reflector enhanced the performance of thin film solar cells. Light trapping structure can also be integrated into the absorbing layer; the best example of this is a silicon nanowire solar cell with radial p-n junction [109]. This structure has good absorption with effective charge extraction along the length of the nanowire, which is advantageous. It was also demonstrated that the light trapping of Si nanowire cells was above theoretical limit of randomisation [109]. These different nanostructures discussed can be in order of wavelength and benefits from photonic crystal properties.

For Si nanowires arranged with different photonic crystal lattices [110], the regular photonic crystals showed anisotropy absorption profile. Isotropic absorption profile was obtained when Si nanowires were in quasi-random arrangement. Optical absorption for silicon nano hole array was compared to silicon nanowire for the same lattice constant (500nm). It was reported [111]that nanohole array showed higher absorption than nanowires [113]. The absorption of nanohole array increased with reduction in silicon fill fraction.

In this thesis, the proposed hybrid solar structure consists of etching nano holes into the solar cell. 12-fold lattice with higher order symmetry is preferred to benefit from their isotropic absorption. PQC holes are then hybridised with suitable QDs, resulting in hybrid PQC/QD solar cells.

References

1. Gerasimos Konstantatos and Edward H. Sargent, *Colloidal Quantum Dot Optoelectronics and Photovoltaics* (Cambridge university press, 2013).

2. O. V Prezhdo, "Photoinduced Dynamics in Semiconductor Quantum Dots: Insights from Time-Domain ab Initio Studies," Acc. Chem. Res. **42**, 2005–2016 (2009).

3. L. E. Brus, "A simple model for the ionization potential, electron affinity, and aqueous redox potentials of small semiconductor crystallites," J. Chem. Phys. **79**, 5566–5571 (1983).

4. O.Madelung, *Semiconductors:Data Handbook* (Springer-Verlag, 2004).

5. C. de M. Donega, *Nanoparticles Workhorses of Nanoscience* (Springer, 2014).

6. C. de M. Donega, "Synthesis and properties of colloidal heteronanocrystals," Chem. Soc. Rev. **40**, 1512–1546 (2011).

7. S. Neeleshwar, C. L. Chen, C. B. Tsai, Y. Y. Chen, C. C. Chen, S. G. Shyu, and M. S. Seehra, "Size-dependent properties of CdSe quantum dots," Phys. Rev. B **71**, 201307 (2005).

8. J. J. Peterson and T. D. Krauss, "Photobrightening and photodarkening in PbS quantum dots," Phys. Chem. Chem. Phys. **8**, 3851–3856 (2006).

9. D. J. Norris and M. G. Bawendi, "Measurement and assignment of the size-dependent optical spectrum in CdSe quantum dots," Phys. Rev. B **53**, 16338–16346 (1996).

10. L. M. Ramaniah and S. V Nair, "Optical absorption in semiconductor quantum dots: A tight-binding approach," Phys. Rev. B **47**, 7132–7139 (1993).

11. S. A. Empedocles, D. J. Norris, and M. G. Bawendi, "Photoluminescence Spectroscopy of Single CdSe Nanocrystallite Quantum Dots," Phys. Rev. Lett. **77**, 3873–3876 (1996).

12. D. J. Norris, A. L. Efros, M. Rosen, and M. G. Bawendi, "Size dependence of exciton fine structure in CdSe quantum dots," Phys. Rev. B **53**, 16347–16354 (1996).

13. C. B. Murray, S. Sun, W. Gaschler, H. Doyle, T. A. Betley, and C. R. Kagan, "Colloidal synthesis of nanocrystals and nanocrystal superlattices," IBM J. Res. Dev. **45**, 47–56 (2001).

14. A. P. Alivisatos, "Semiconductor Clusters, Nanocrystals, and Quantum Dots," Science (80-.). **271**, 933–937 (1996).

15. H. Wang, H. Nakamura, M. Uehara, Y. Yamaguchi, M. Miyazaki, and H. Maeda, "Highly

Luminescent CdSe/ZnS Nanocrystals Synthesized Using a Single-Molecular ZnS Source in a Microfluidic Reactor," Adv. Funct. Mater. **15**, 603–608 (2005).

16. P. Reiss, J. Bleuse, and A. Pron, "Highly Luminescent CdSe/ZnSe Core/Shell Nanocrystals of Low Size Dispersion," Nano Lett. **2**, 781–784 (2002).

17. J. Bang, J. Park, J. H. Lee, N. Won, J. Nam, J. Lim, B. Y. Chang, H. J. Lee, B. Chon, J. Shin, J. B. Park, J. H. Choi, K. Cho, S. M. Park, T. Joo, and S. Kim, "ZnTe/ZnSe (Core/Shell) Type-II Quantum Dots: Their Optical and Photovoltaic Properties," Chem. Mater. **22**, 233–240 (2010).

18. V. I. Klimov, S. A. Ivanov, J. Nanda, M. Achermann, I. Bezel, J. A. McGuire, and A. Piryatinski, "Single-exciton optical gain in semiconductor nanocrystals," Nature **447**, 441–446 (2007).

19. J. McBride, J. Treadway, L. C. Feldman, S. J. Pennycook, and S. J. Rosenthal, "Structural Basis for Near Unity Quantum Yield Core/Shell Nanostructures," Nano Lett. **6**, 1496–1501 (2006).

20. R. Xie, U. Kolb, J. Li, T. Basché, and A. Mews, "Synthesis and Characterization of Highly Luminescent CdSe−Core CdS/Zn0.5Cd0.5S/ZnS Multishell Nanocrystals," J. Am. Chem. Soc. **127**, 7480–7488 (2005).

21. K. J. Nordell, E. M. Boatman, and G. C. Lisensky, "A Safer, Easier, Faster Synthesis for CdSe Quantum Dot Nanocrystals," J. Chem. Educ. **82**, 1697 (2005).

22. D. Zhou, M. Lin, Z. Chen, H. Sun, H. Zhang, H. Sun, and B. Yang, "Simple Synthesis of Highly Luminescent Water-Soluble CdTe Quantum Dots with Controllable Surface Functionality," Chem. Mater. **23**, 4857–4862 (2011).

23. Y.-F. Liu and J.-S. Yu, "Selective synthesis of CdTe and high luminescence CdTe/CdS quantum dots: the effect of ligands," J. Colloid Interface Sci. **333**, 690–698 (2009).

24. A. B. Greytak, P. M. Allen, W. Liu, J. Zhao, E. R. Young, Z. Popović, B. J. Walker, D. G. Nocera, and M. G. Bawendi, "Alternating layer addition approach to CdSe/CdS core/shell quantum dots with near-unity quantum yield and high on-time fractions," Chem. Sci. **3**, 2028–2034 (2012).

25. R. C. Page, D. Espinobarro-Velazquez, M. A. Leontiadou, C. Smith, E. A. Lewis, S. J. Haigh, C. Li, H. Radtke, A. Pengpad, F. Bondino, E. Magnano, I. Pis, W. R. Flavell, P. O'Brien, and D. J. Binks, "Near-Unity Quantum Yields from Chloride Treated CdTe Colloidal Quantum Dots," Small **11**, 1548–1554 (2015).

26. V. L. Colvin, M. C. Schlamp, and A. P. Alivisatos, "Light-emitting diodes made from cadmium selenide nanocrystals and a semiconducting polymer," Nature **370**, 354–357 (1994).

27. M. C. Schlamp, X. Peng, and and A. P. Alivisatos, "Improved efficiencies in light emitting diodes made with CdSe(CdS) core/shell type nanocrystals and a semiconducting polymer," J. Appl. Phys. **82**, 5837–5842 (1997).

28. S. Coe, W.-K. Woo, M. Bawendi, and & V. Bulovic, "Electroluminescence from single monolayers of nanocrystals in molecular organic devices," Nature **420**, 800–803 (2002).

29. S. Coe-Sullivan, J. S. Steckel, W.-K. Woo, M. G. Bawendi, and V. Bulović, "Large-Area Ordered Quantum-Dot Monolayers via Phase Separation During Spin-Casting," Adv. Funct. Mater. **15**, 1117–1124 (2005).

30. J. Zhao, J. a. Bardecker, A. M. Munro, M. S. Liu, Y. Niu, I. K. Ding, J. Luo, B. Chen, A. K. Y. Jen, and D. S. Ginger, "Efficient CdSe/CdS quantum dot light-emitting diodes using a thermally polymerized hole transport layer," Nano Lett. **6**, 463–467 (2006).

31. P. O. Anikeeva, C. F. Madigan, J. E. Halpert, M. G. Bawendi, and V. Bulović, "Electronic and excitonic processes in light-emitting devices based on organic materials and colloidal quantum dots," Phys. Rev. B **78**, 85434 (2008).

32. L. Kim, P. O. Anikeeva, S. a. Coe-Sullivan, J. S. Steckel, M. G. Bawendi, and V. Bulović, "Contact printing of quantum dot light-emitting devices," Nano Lett. **8**, 4513–4517 (2008).

33. P. O. Anikeeva, J. E. Halpert, M. G. Bawendi, and V. Bulović, "Quantum dot light-emitting devices with electroluminescence tunable over the entire visible spectrum," Nano Lett. **9**, 2532–2536 (2009).

34. A. H. Mueller, M. A. Petruska, M. Achermann, D. J. Werder, E. A. Akhadov, D. D. Koleske, M. A. Hoffbauer, and V. I. Klimov, "Multicolor Light-Emitting Diodes Based on Semiconductor Nanocrystals Encapsulated in GaN Charge Injection Layers," Nano Lett. **5**, 1039–1044 (2005).

35. J. M. Caruge, J. E. Halpert, V. Wood, V. Bulovic, and M. G. Bawendi, "Colloidal quantum-dot light-emitting diodes with metal-oxide charge transport layers," Nat Phot. **2**, 247–250 (2008).

36. W. K. Bae, S. Brovelli, and V. I. Klimov, "Spectroscopic insights into the performance of quantum dot light-emitting diodes," MRS Bull. **38**, 721–730 (2013).

37. J. Kwak, W. K. Bae, D. Lee, I. Park, J. Lim, M. Park, H. Cho, H. Woo, D. Y. Yoon, K.

Char, S. Lee, and C. Lee, "Bright and efficient full-color colloidal quantum dot light-emitting diodes using an inverted device structure," Nano Lett. **12**, 2362–2366 (2012).

38. B. S. Mashford, M. Stevenson, Z. Popovic, C. Hamilton, Z. Zhou, C. Breen, J. Steckel, V. Bulovic, M. Bawendi, S. Coe-Sullivan, and P. T. Kazlas, "High-efficiency quantum-dot light-emitting devices with enhanced charge injection," Nat. Photonics **7**, 407–412 (2013).

39. X. Dai, Z. Zhang, Y. Jin, Y. Niu, H. Cao, X. Liang, L. Chen, J. Wang, and X. Peng, "Solution-processed, high-performance light-emitting diodes based on quantum dots," Nature **515**, 96–99 (2014).

40. Y. Yang, Y. Zheng, W. Cao, A. Titov, J. Hyvonen, J. R. Manders, J. Xue, P. H. Holloway, and L. Qian, "High-efficiency light-emitting devices based on quantum dots with tailored nanostructures," Nat. Photonics **9**, 259–266 (2015).

41. T.-H. Kim, K.-S. Cho, E. K. Lee, S. J. Lee, J. Chae, J. W. Kim, D. H. Kim, J.-Y. Kwon, G. Amaratunga, S. Y. Lee, B. L. Choi, Y. Kuk, J. M. Kim, and K. Kim, "Full-colour quantum dot displays fabricated by transfer printing," Nat. Photonics **5**, 176–182 (2011).

42. M. K. Choi, J. Yang, K. Kang, D. C. Kim, C. Choi, C. Park, S. J. Kim, S. I. Chae, T.-H. Kim, J. H. Kim, T. Hyeon, and D.-H. Kim, "Wearable red–green–blue quantum dot light-emitting diode array using high-resolution intaglio transfer printing," Nat. Commun. **6**, 7149 (2015).

43. Y. Shirasaki, G. J. Supran, M. G. Bawendi, and V. Bulovic, "Emergence of colloidal quantum-dot light-emitting technologies," Nat Phot. **7**, 13–23 (2013).

44. Y. N. and M. I. and D. S. and M. S. and T. Mukai, "White light emitting diodes with super-high luminous efficacy," J. Phys. D. Appl. Phys. **43**, 354002 (2010).

45. J. Lee, V. C. Sundar, J. R. Heine, M. G. Bawendi, and K. F. Jensen, "Full Color Emission from II–VI Semiconductor Quantum Dot–Polymer Composites," Adv. Mater. **12**, 1102–1105 (2000).

46. S. Nizamoglu, G. Zengin, and H. V. Demir, "Color-converting combinations of nanocrystal emitters for warm-white light generation with high color rendering index," Appl. Phys. Lett. **92**, 2010–2013 (2008).

47. S. Nizamoglu, T. Ozel, E. Sari, and H. V Demir, "White light generation using CdSe/ZnS core–shell nanocrystals hybridized with InGaN/GaN light emitting diodes," Nanotechnology **18**, 65709 (2007).

48. P. Zhong, G. He, and M. Zhang, "Optimal spectra of white light-emitting diodes using

quantum dot nanophosphors," Opt. Express **20**, 9122–9134 (2012).

49. E. Jang, S. Jun, H. Jang, J. Lim, B. Kim, and Y. Kim, "White-Light-Emitting Diodes with Quantum Dot Color Converters for Display Backlights," Adv. Mater. **22**, 3076–3080 (2010).

50. J. S. Steckel, J. Ho, C. Hamilton, C. Breen, W. Liu, P. Allen, J. Xi, and S. Coe-Sullivan, "Quantum dots: The ultimate down-conversion material for LCD displays," Dig. Tech. Pap. - SID Int. Symp. **45**, 130–133 (2014).

51. V. Wood and V. Bulović, "Colloidal quantum dot light-emitting devices," Nano Rev. **1**, 1–7 (2010).

52. N. C. Greenham, X. Peng, and A. P. Alivisatos, "Charge separation and transport in conjugated-polymer/semiconductor-nanocrystal composites studied by photoluminescence quenching and photoconductivity," Phys. Rev. B **54**, 17628–17637 (1996).

53. R. Zhou, R. Stalder, D. Xie, W. Cao, Y. Zheng, Y. Yang, M. Plaisant, P. H. Holloway, K. S. Schanze, J. R. Reynolds, and J. Xue, "Enhancing the Efficiency of Solution-Processed Polymer:Colloidal Nanocrystal Hybrid Photovoltaic Cells Using Ethanedithiol Treatment," ACS Nano **7**, 4846–4854 (2013).

54. Z. Liu, Y. Sun, J. Yuan, H. Wei, X. Huang, L. Han, W. Wang, H. Wang, and W. Ma, "High-Efficiency Hybrid Solar Cells Based on Polymer/PbSxSe1-x Nanocrystals Benefiting from Vertical Phase Segregation," Adv. Mater. **25**, 5772–5778 (2013).

55. J. P. Clifford, K. W. Johnston, L. Levina, and E. H. Sargent, "Schottky barriers to colloidal quantum dot films," Appl. Phys. Lett. **91**, 253117 (2007).

56. J. M. Luther, M. Law, Q. Song, C. L. Perkins, M. C. Beard, and A. J. Nozik, "Structural, optical, and electrical properties of self-assembled films of PbSe nanocrystals treated with 1,2-ethanedithiol," ACS Nano **2**, 271–80 (2008).

57. J. T. and E. H. Sargent, "Solution- processed infrared quantum dot solar cells," in *Colloidal Quantum Dot Optoelectronics and Photovoltaics* (Cambridge university press, 2013), pp. 256–286.

58. K. W. Johnston, A. G. Pattantyus-Abraham, J. P. Clifford, S. H. Myrskog, D. D. MacNeil, L. Levina, and E. H. Sargent, "Schottky-quantum dot photovoltaics for efficient infrared power conversion," Appl. Phys. Lett. **92**, 151115 (2008).

59. J. M. Luther, M. Law, M. C. Beard, Q. Song, M. O. Reese, R. J. Ellingson, and A. J. Nozik, "Schottky solar cells based on colloidal nanocrystal films.," Nano Lett. **8**, 3488–92 (2008).

60. C. Piliego, L. Protesescu, S. Z. Bisri, M. V. Kovalenko, and M. A. Loi, "5.2% efficient PbS nanocrystal Schottky solar cells," Energy Environ. Sci. **6**, 3054 (2013).

61. L. Etgar, T. Moehl, S. Gabriel, S. G. Hickey, A. Eychmüller, and M. Grätzel, "Light energy conversion by mesoscopic PbS quantum dots/TiO2 heterojunction solar cells.," ACS Nano **6**, 3092–9 (2012).

62. A. G. Pattantyus-Abraham, I. J. Kramer, A. R. Barkhouse, X. Wang, G. Konstantatos, R. Debnath, L. Levina, I. Raabe, M. K. Nazeeruddin, M. Grätzel, and E. H. Sargent, "Depleted-heterojunction colloidal quantum dot solar cells.," ACS Nano **4**, 3374–80 (2010).

63. A. H. Ip, S. M. Thon, S. Hoogland, O. Voznyy, D. Zhitomirsky, R. Debnath, L. Levina, L. R. Rollny, G. H. Carey, A. Fischer, K. W. Kemp, I. J. Kramer, Z. Ning, A. J. Labelle, K. W. Chou, A. Amassian, and E. H. Sargent, "Hybrid passivated colloidal quantum dot solids," Nat Nano **7**, 577–582 (2012).

64. A. J. Labelle, S. M. Thon, S. Masala, M. M. Adachi, H. Dong, M. Farahani, A. H. Ip, A. Fratalocchi, and E. H. Sargent, "Colloidal Quantum Dot Solar Cells Exploiting Hierarchical Structuring," Nano Lett. **15**, 1101–1108 (2015).

65. J. Du, Z. Du, J.-S. Hu, Z. Pan, Q. Shen, J. Sun, D. Long, H. Dong, L. Sun, X. Zhong, and L.-J. Wan, "Zn–Cu–In–Se Quantum Dot Solar Cells with a Certified Power Conversion Efficiency of 11.6%," J. Am. Chem. Soc. **138**, 4201–4209 (2016).

66. K. Masuko, M. Shigematsu, T. Hashiguchi, D. Fujishima, M. Kai, N. Yoshimura, T. Yamaguchi, Y. Ichihashi, T. Mishima, N. Matsubara, T. Yamanishi, T. Takahama, M. Taguchi, E. Maruyama, and S. Okamoto, "Achievement of More Than 25% Conversion Efficiency With Crystalline Silicon Heterojunction Solar Cell," IEEE J. Photovoltaics **4**, 1433–1435 (2014).

67. M. A. Green, K. Emery, Y. Hishikawa, W. Warta, and E. D. Dunlop, "Solar cell efficiency tables (version 48)," Prog. Photovoltaics Res. Appl. **24**, 905–913 (2016).

68. T. Förster, "10th Spiers Memorial Lecture. Transfer mechanisms of electronic excitation," Discuss. Faraday Soc. **27**, 7 (1959).

69. G. Itskos, G. Heliotis, P. G. Lagoudakis, J. Lupton, N. P. Barradas, E. Alves, S. Pereira, I. M. Watson, M. D. Dawson, J. Feldmann, R. Murray, and D. D. C. Bradley, "Efficient dipole-dipole coupling of Mott-Wannier and Frenkel excitons in (Ga,In)N quantum well/polyfluorene semiconductor heterostructures," Phys. Rev. B **76**, 35344 (2007).

70. J. Hill, S. Y. Heriot, O. Worsfold, T. H. Richardson, A. M. Fox, and D. D. C. Bradley, "Controlled Förster energy transfer in emissive polymer Langmuir-Blodgett structures,"

Phys. Rev. B **69**, 41303 (2004).

71. M. Lunz, A. L. Bradley, W.-Y. Chen, and Y. K. Gun'ko, "Two-Dimensional Förster Resonant Energy Transfer in a Mixed Quantum Dot Monolayer: Experiment and Theory," J. Phys. Chem. C **113**, 3084–3088 (2009).

72. M. Achermann, M. A. Petruska, S. Kos, D. L. Smith, D. D. Koleske, and V. I. Klimov, "Energy-transfer pumping of semiconductor nanocrystals using an epitaxial quantum well.," Nature **429**, 642–646 (2004).

73. V. M. Agranovich, D. M. Basko, G. C. La Rocca, and F. Bassani, "Excitons and optical nonlinearities in hybrid organic-inorganic nanostructures," J. Phys. Condens. Matter **10**, 9369–9400 (1998).

74. V. M. Agranovich, G. C. La Rocca, and F. Bassani, "Efficient electronic energy transfer from a semiconductor quantum well to an organic material," J. Exp. Theor. Phys. Lett. **66**, 748–751 (1997).

75. G. Heliotis, G. Itskos, R. Murray, M. D. Dawson, I. M. Watson, and D. D. C. Bradley, "Hybrid Inorganic/Organic Semiconductor Heterostructures with Efficient Non-Radiative Energy Transfer," Adv. Mater. **18**, 334–338 (2006).

76. S. Blumstengel, S. Sadofev, C. Xu, J. Puls, and F. Henneberger, "Converting Wannier into Frenkel excitons in an inorganic/organic hybrid semiconductor nanostructure.," Phys. Rev. Lett. **97**, 237401 (2006).

77. M. Achermann, M. A. Petruska, D. D. Koleske, M. H. Crawford, and V. I. Klimov, "Nanocrystal-based light-emitting diodes utilizing high-efficiency nonradiative energy transfer for color conversion.," Nano Lett. **6**, 1396–400 (2006).

78. S. Chanyawadee, P. G. Lagoudakis, R. T. Harley, M. D. B. Charlton, D. V Talapin, H. W. Huang, and C.-H. Lin, "Increased color-conversion efficiency in hybrid light-emitting diodes utilizing non-radiative energy transfer.," Adv. Mater. **22**, 602–606 (2010).

79. J. J. Rindermann, G. Pozina, B. Monemar, L. Hultman, H. Amano, and P. G. Lagoudakis, "Dependence of resonance energy transfer on exciton dimensionality.," Phys. Rev. Lett. **107**, 236805 (2011).

80. S. Rohrmoser, J. Baldauf, R. T. Harley, P. G. Lagoudakis, S. Sapra, A. Eychmüller, and I. M. Watson, "Temperature dependence of exciton transfer in hybrid quantum well/nanocrystal heterostructures," Appl. Phys. Lett. **91**, 92126 (2007).

81. D. L. Dexter, "Two ideas on energy transfer phenomena: Ion-pair effects involving the OH

stretching mode, and sensitization of photovoltaic cells," J. Lumin. **18**–**19**, 779–784 (1979).

82. A. P. Alivisatos, M. F. Arndt, S. Efrima, D. H. Waldeck, and C. B. Harris, "Electronic energy transfer at semiconductor interfaces. I. Energy transfer from two-dimensional molecular films to Si(111)," J. Chem. Phys. **86**, 6540–6549 (1987).

83. P. M. Whitmore, A. P. Alivisatos, and C. B. Harris, "Distance Dependence of Electronic Energy Transfer to Semiconductor Surfaces: n 3 π * Pyrazine/GaAs(110)," Phys. Rev. Lett. **50**, 1092–1094 (1983).

84. V. Gowrishankar, S. R. Scully, A. T. Chan, M. D. McGehee, Q. Wang, and H. M. Branz, "Exciton harvesting, charge transfer, and charge-carrier transport in amorphous-silicon nanopillar/polymer hybrid solar cells," J. Appl. Phys. **103**, 64511 (2008).

85. S. Lu and A. Madhukar, "Nonradiative resonant excitation transfer from nanocrystal quantum dots to adjacent quantum channels.," Nano Lett. **7**, 3443–51 (2007).

86. M. Achermann, M. A. Petruska, S. A. Crooker, and V. I. Klimov, "Picosecond Energy Transfer in Quantum Dot Langmuir−Blodgett Nanoassemblies," J. Phys. Chem. B **107**, 13782–13787 (2003).

87. S. Chanyawadee, R. T. Harley, M. Henini, D. V. Talapin, and P. G. Lagoudakis, "Photocurrent enhancement in hybrid nanocrystal quantum-dot p-i-n photovoltaic devices," Phys. Rev. Lett. **102**, 1–4 (2009).

88. S. Lu, Z. Lingley, T. Asano, D. Harris, T. Barwicz, S. Guha, and A. Madhukar, "Photocurrent induced by nonradiative energy transfer from nanocrystal quantum dots to adjacent silicon nanowire conducting channels: toward a new solar cell paradigm.," Nano Lett. **9**, 4548–52 (2009).

89. H. M. Nguyen, O. Seitz, D. Aureau, A. Sra, N. Nijem, Y. N. Gartstein, Y. J. Chabal, and A. V. Malko, "Spectroscopic evidence for nonradiative energy transfer between colloidal CdSe/ZnS nanocrystals and functionalized silicon substrates," Appl. Phys. Lett. **98**, 161904 (2011).

90. P. Andreakou, M. Brossard, C. Li, P. G. Lagoudakis, M. Bernechea, and G. Konstantatos, "Spectroscopic evidence of resonance energy transfer mechanism from PbS QDs to bulk silicon," EPJ Web Conf. **54**, 1017 (2013).

91. J. N. W. John D. Joannopoulos, Robert D. Meade, *Photonic Crystals:Molding the Flow of Light* (Princenton university press, 1995).

92. D. Shechtman, I. Blech, D. Gratias, and J. W. Cahn, "Metallic Phase with Long-Range

Orientational Order and No Translational Symmetry," Phys. Rev. Lett. **53**, 1951–1953 (1984).

93. M. Oxborrow and C. L. Henley, "Random square-triangle tilings: A model for twelvefold-symmetric quasicrystals," Phys. Rev. B **48**, 6966–6998 (1993).

94. M. E. Zoorob, M. D. B. Charlton, G. J. Parker, J. J. Baumberg, and M. C. Netti, "Complete photonic bandgaps in 12-fold symmetric quasicrystals," Nature **404**, 740–743 (2000).

95. S. Pimputkar, J. S. Speck, S. P. DenBaars, and S. Nakamura, "Prospects for LED lighting," Nat Phot. **3**, 180–182 (2009).

96. T. Fujii, Y. Gao, R. Sharma, E. L. Hu, S. P. DenBaars, and S. Nakamura, "Increase in the extraction efficiency of GaN-based light-emitting diodes via surface roughening," Appl. Phys. Lett. **84**, 855–857 (2004).

97. C.-F. Lai, J.-Y. Chi, H.-C. Kuo, C.-H. Chao, H.-T. Hsueh, J.-F. T. Wang, and W.-Y. Yeh, "Anisotropy of light extraction from GaN two-dimensional photonic crystals," Opt. Express **16**, 7285–7294 (2008).

98. Z. S. Zhang, B. Zhang, J. Xu, K. Xu, Z. J. Yang, Z. X. Qin, T. J. Yu, and D. P. Yu, "Effects of symmetry of GaN-based two-dimensional photonic crystal with quasicrystal lattices on enhancement of surface light extraction," Appl. Phys. Lett. **88**, 171103 (2006).

99. P. A. Shields, M. D. B. Charlton, T. Lee, M. E. Zoorob, D. W. E. Allsopp, and W. N. Wang, "Enhanced Light Extraction by Photonic Quasi-Crystals in GaN Blue LEDs," IEEE J. Sel. Top. Quantum Electron. **15**, 1269–1274 (2009).

100. A. Polman and H. A. Atwater, "Photonic design principles for ultrahigh-efficiency photovoltaics," Nat Mater **11**, 174–177 (2012).

101. M. L. Brongersma, Y. Cui, and S. Fan, "Light management for photovoltaics using high-index nanostructures," Nat Mater **13**, 451–460 (2014).

102. H. Savin, P. Repo, G. von Gastrow, P. Ortega, E. Calle, M. Garín, and R. Alcubilla, "Black silicon solar cells with interdigitated back-contacts achieve 22.1% efficiency," Nat Nano **10**, 624–628 (2015).

103. P. Spinelli, M. A. Verschuuren, and A. Polman, "Broadband omnidirectional antireflection coating based on subwavelength surface Mie resonators," Nat Commun **3**, 692 (2012).

104. J. Zhu, Z. Yu, G. F. Burkhard, C.-M. Hsu, S. T. Connor, Y. Xu, Q. Wang, M. McGehee, S. Fan, and Y. Cui, "Optical Absorption Enhancement in Amorphous Silicon Nanowire and Nanocone Arrays," Nano Lett. **9**, 279–282 (2009).

105. S. Jeong, M. D. McGehee, and Y. Cui, "All-back-contact ultra-thin silicon nanocone solar cells with 13.7% power conversion efficiency," Nat Commun **4**, (2013).

106. L. Zeng, Y. Yi, C. Hong, J. Liu, N. Feng, X. Duan, L. C. Kimerling, and B. A. Alamariu, "Efficiency enhancement in Si solar cells by textured photonic crystal back reflector," Appl. Phys. Lett. **89**, 111111 (2006).

107. C.-M. Hsu, C. Battaglia, C. Pahud, Z. Ruan, F.-J. Haug, S. Fan, C. Ballif, and Y. Cui, "High-Efficiency Amorphous Silicon Solar Cell on a Periodic Nanocone Back Reflector," Adv. Energy Mater. **2**, 628–633 (2012).

108. A. Ingenito, O. Isabella, and M. Zeman, "Experimental Demonstration of 4n2 Classical Absorption Limit in Nanotextured Ultrathin Solar Cells with Dielectric Omnidirectional Back Reflector," ACS Photonics **1**, 270–278 (2014).

109. E. Garnett and P. Yang, "Light Trapping in Silicon Nanowire Solar Cells," Nano Lett. **10**, 1082–1087 (2010).

110. M. D. Kelzenberg, S. W. Boettcher, J. A. Petykiewicz, D. B. Turner-Evans, M. C. Putnam, E. L. Warren, J. M. Spurgeon, R. M. Briggs, N. S. Lewis, and H. A. Atwater, "Enhanced absorption and carrier collection in Si wire arrays for photovoltaic applications," Nat Mater **9**, 239–244 (2010).

111. S. E. Han and G. Chen, "Optical Absorption Enhancement in Silicon Nanohole Arrays for Solar Photovoltaics," Nano Lett. **10**, 1012–1015 (2010).

Chapter 3: Hybrid QD photonic quasi crystal LED

3.1 Introduction

In recent years, the promise of controllable narrow emission bands, quantum dots (QDs) with the advent of near-unity photoluminescence quantum yields, [1,2] have been heralded as potentially a ground breaking emitting materials for colour conversion applications [3]. While direct utilisation of QDs as electrically excited emitters is an inspiring prospect, the reported external quantum efficiencies (EQE) of such devices remain low, with highest reported values around 20% [4,5]. The imbalance in charge injection has been delimiting mechanism of electrically pumped QD LEDs. On contrary commercial and laboratory III-V LEDs have EQE about 30-40% [6] and 85% [7] respectively. The incorporation of QDs as colour converters in traditional solid-state devices have proven to be more successful, QD LED displays being a prime example [8]. In these devices, QDs are typically dispersed into a polymer film on the surface of the LED chip. As far-field configuration, only photons escaping from the LED stack is absorbed by the emitters. Most of the blue light emitted within the LED gets trapped in its epitaxial layers due to total internal reflection, resulting in poor radiative coupling between the blue light field of MQWs and the QDs. This dramatically reduces the overall efficiency of such hybrid LED architectures. A common approach to improve the coupling efficiency between the LED and QDs is to roughen the LED surface or to etch nanostructures into the LED surface, in the form of photonic crystals. These etched structures only typically penetrate onto the top barrier layer and act as diffraction gratings [9,10], enhancing the extraction efficiency of the MQW emission. While nanohole [11] or nanorod [12] structures penetrating into the active area have shown to improve the colour conversion efficiency. Simple photonic crystal designs and poor sidewall quality have so far limited the performance of such devices [12–14].

This chapter presents an efficient hybrid 12-fold photonic quasi-crystal (PQC) multi-quantum well (MQW) white LED geometry which allows a drastic improvement of the out-coupling efficiency while retaining the good electrical properties of unpatterned devices. This chapter demonstrates that this architecture allows electrically injected carriers to efficiently couple to the QDs through non-radiative resonant energy transfer while allowing near-field coupling between the blue light field and the emitters within the LED, and this results into record-breaking effective quantum yields reaching 123% for single colour QDs with peak emission at 585nm and 110% for white LEDs [15].

3.2 Materials and Methods

3.2.1 Fabrication of hybrid PQC LED

Luxtaltek Corporation, Taiwan has provided the PQC LED used in this chapter. The LED epi-structure was grown on a patterned sapphire substrate via metal organic chemical vapour deposition (MOCVD) reactor using a bottom to top approach, sequentially depositing a 50nm GaN nucleation layer, a 2μm un-doped GaN buffer layer, a 3μm Si-doped n-GaN layer, 10 pairs of $In_{0.21}Ga_{0.79}N$/GaN MQWs with a central wavelength of 453nm and a 200nm Mg-doped p-GaN layer. After the growth of the LED wafer, a 230nm indium tin oxide (ITO) transparent conducting layer was evaporated using e-beam on top of the LED wafer. Nano-imprint lithography (NIL) and photolithography were used to define nanoholes within a selected mesa area. Silicon dioxide layer with thickness of 400 nm was first deposited on the surface of the prepared LED wafer by plasma-enhanced chemical vapour deposition (PECVD) and then 360nm thick imprint-resist (IR) was spun at 3000rpm on top of SiO_2 layer. By placing and releasing a nano-imprint mold onto IR layer, a 12-fold photonic quasi-periodic crystal nanohole pattern was transferred to the IR layer. SiO_2 nanoholes were formed through a two-steps plasma reactive ion etching (RIE) technique using O_2 and CHF_3 process gases. Silicon dioxide layer was then coated with photoresist (PR) layer and pattern of selected dry-etching areas was defined using standard photolithography process. The LED wafer with a PR layer and a nano-patterned dielectric layer was used etched using inductively coupled plasma reactive ion etching (ICP-RIE) system. The process gases used were Cl_2 and BCl_3 with flow rates of 20sccm and 10sccm respectively where bias power and ICP power were set to 100W. The etch depth of LED stack including the thickness of ITO film is 1.2um.

To complete the modular array LED chip, the PQC LED wafer was processed through a link-chip process. The etching of ITO and mesa layer were done using a standard chip processes utilising photolithography, wet-etch and dry-etch processes. The ITO thin film on the LED wafer was etched to form an ohmic-contact layer by wet etch using a mixed solution of $HCl/FeCl_3$. This was carried out after the pattern transfer using photolithography technique. The mesa area was then defined by photolithography and etching was performed using Cl_2/BCl_3/Ar etching gas in an ICP-RIE system which transferred the mesa pattern onto the n-GaN layer. To obtain the chip isolation, a PR/SiO_2 (2μm/10μm) layer was employed as hard mask in a slow dry-etching. The sidewalls of isolated chips were then passivated with a 500nm SiO_2 PECVD film. A multi-metal layer (Cr/Au=50/1500nm) was formed onto the surface of ITO and n-GaN via e-gun evaporation system and then PR was lift-off. The final LED structure consists of 80 link chips (1.1x0.2 mm^2) integrated into a 25mm^2 chip area. The detailed process steps and schematic of fabrication is shown in appendix A.1.

The QDs used for device hybridisation were Trilite fluorescent Nanocrystals procured from Cytodiagnostics. These CdS_xSe_{1-x}/ZnS core/shell colloidal semiconductor QDs (oleic acid capped) were found to have 1s emission peaks at 535±15nm (QD-535), 585±15nm (QD-585), 630±15nm (QD-630) and their 1s absorption peaks at 515nm, 560nm and 620nm respectively. The QDs dispersed in toluene were deposited on the PQC devices using dynamic spin coating at 1500 rpm and dried at atmospheric condition.

3.2.2 Characterisation Method

I-V characterization was performed using a Keitheley 2400 source meter. LED spectra and intensities were measured inside a six inch integration sphere (figure 3.1) coupled to a TE-cooled BWtek spectrometer. SEM characterisation of the LED and QD thickness were done using a Zeiss Nvision 40 FIB-SEM system. Absorption spectra of the QDs on glass were measured using a Jasco UV/VIS/NIR spectrophotometer.

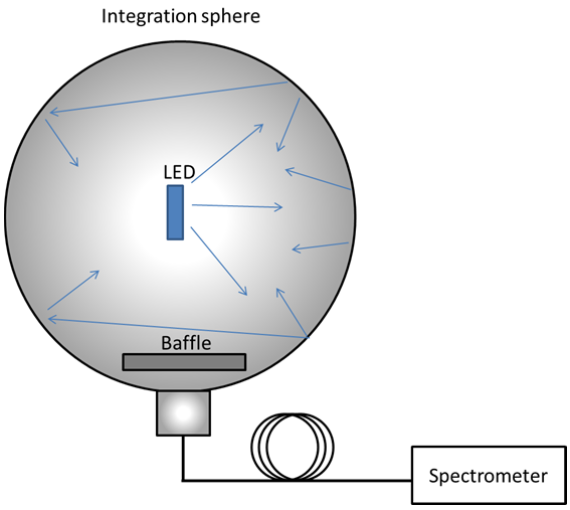

Figure 3.1: Integrating setup for measuring LED spectrum and intensity

Experimental setup of Time resolved photoluminescence (TRPL) is shown in figure 3.2. The life time and decays of excited charge carriers were acquired using a single photon counting (SPC) avalanche photodiode (Micro photon devices PDM series) coupled to Becker and Hickl SPC-140 TCSPC (time correlated single photon counting) acquisition card. The InGaN QWs of the LED were pumped at 380nm using a frequency doubled tunable femtosecond Ti:Sapphire laser (Coherent Chameleon). The excitation power was kept constant at 0.255mW and was focused onto the sample using a 10X Nikon objective (NA=0.50). The photoluminescence from the QWs was collected through the same objective, filtered using a 405nm longpass (Semrock BLP01-405R-25) and a 447nm bandpass (Edmund optics 84-111) filter and focused onto an avalanche photo diode using 40X Nikon objective (NA=0.25).

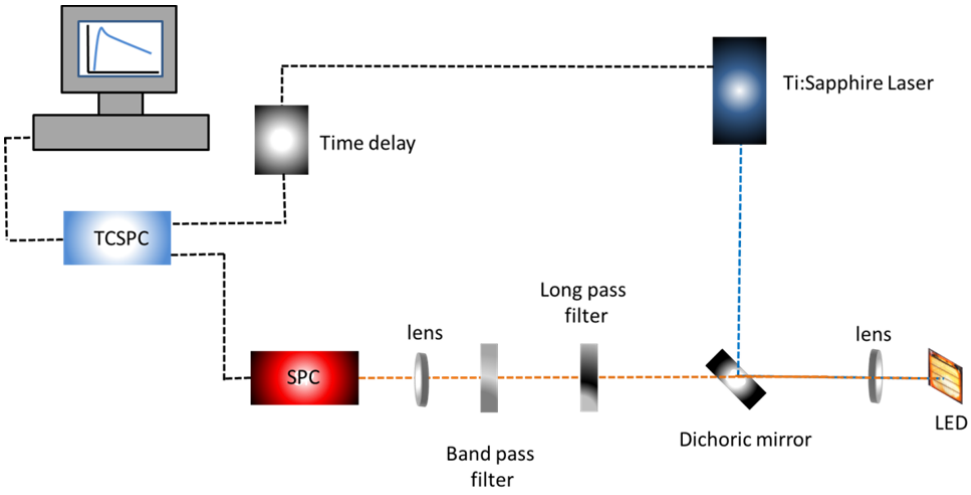

Figure 3.2: Time resolved photoluminescence experimental setup.

3.3 Device Characterisation

The devices studied in this section consist of GaN/InGaN MQW LEDs on patterned sapphire substrate (PSS) into which 12-fold symmetric quasi crystals (PQC) were fabricated using low-cost nanoimprint lithography and plasma etching (see Figure 3.3(a)). As it can be seen in the cross sectional scanning electron microscope (SEM) image given in Figure 3.3(b), the PQC structure penetrates through the MQW active area, forming an array of 480nm diameter cylindrical holes with a lattice pitch of 750nm. A top SEM image of the etched structure is provided in Figure 3.3(c). This high symmetry PQC exhibits long range order and short range disorder and possesses semi-random properties. This PQC geometry has been shown to be far superior to regular photonic crystal lattices commonly adopted for LED applications, due to its highly symmetrical far field beam shape, and due to the relative increase in the density of states, which greatly increases the light extraction [16,17]. The PQCs were integrated into modular LED chips using photolithography, wet and dry etching techniques.

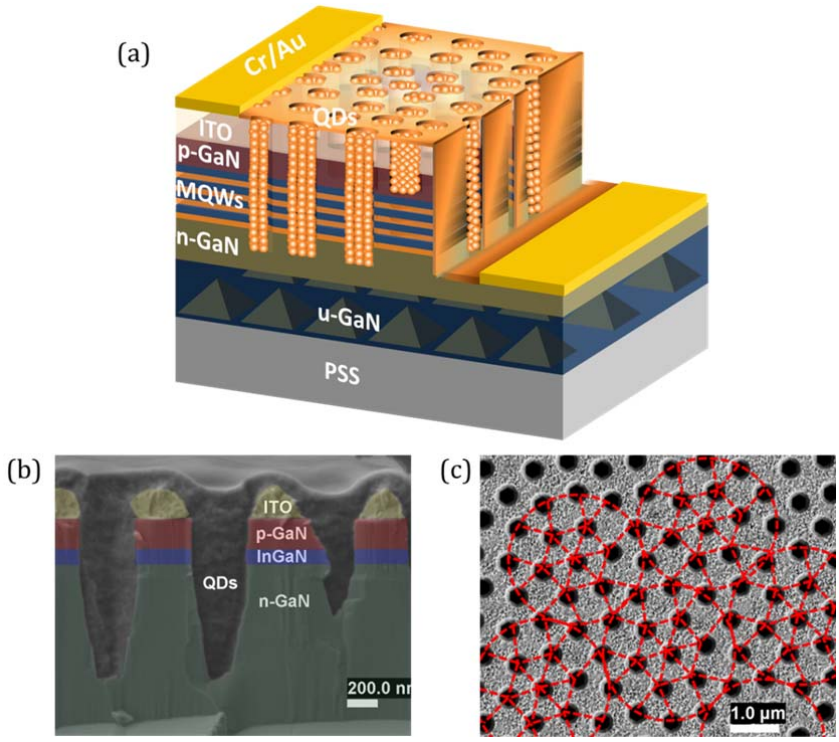

Figure 3.3: (a) Schematic representation, (b) cross-sectional and (c) top SEM images of a photonic quasi-crystal LED

Three different 'off-the-shelf' nearly monodispersed CdS_xSe_{1-x}/ZnS core/shell colloidal semiconductor QDs emitting at 535nm, 585nm and 630nm (referred as QD-535, QD-585, and QD-630) were chosen as colour converters. Spin-coating was used to hybridise PQC LEDs with QD emitters. The spin-coating parameters were tuned to completely fill the nanohole cavities with emitters as shown in Figure. 3.3(b). PQC LEDs were hybridised with both, a single colour QDs and a cocktail of three different colour QDs, to obtain monochromatic color conversion and white devices, respectively. In the case of white device, the relative ratios between the three different colour QDs were tuned to obtain a white light spectrum close to the daylight D-65 standard [18] when combined with a blue LED.

3.3.1 Electrical properties

The electrical properties of the LED chips were studied with and without the PQC. The J-V characteristics are presented in figure 3.4(a) for a planar device (red solid line) and for a PQC device (black solid line). The semi-log J-V plot of figure 3.4 (a) and (b) is shown in appendix A.2. The current density of the PQC structure is found to be slightly higher than the planar case at low current (refer to Figure 3.4), indicating the presence of minor shunting paths in the PQC sidewalls. The shunt resistance reduces from 5.03K ohm cm^2 to 2.75k ohm cm^2 after patterning of PQC. Etching the PQC structure weakly lowers the current-density at higher voltages, with a maximum relative drop of ~19% at 11.5V. The series resistance of LED increases by a factor of 1.2 times after patterning with PQC .The increase of the series resistance in the PQC case is attributed to the

relative poorer current spreading properties in the top layers after etching. Notably, the turn-on voltage is found in both cases to be ~10.3V, the LED chips geometry necessitating higher driving voltages than typical commercial devices. These results, similar to the best reported values in the literature [13,19], indicate a very good nanohole sidewall quality. Hybridisation with QDs was found to weakly impact the electrical properties (Figure 3.4 (b)). A slightly higher current density is observed in the case of hybrid LED compared to the bare case. This effect is attributed to an improvement of the passivation at MQW interface.

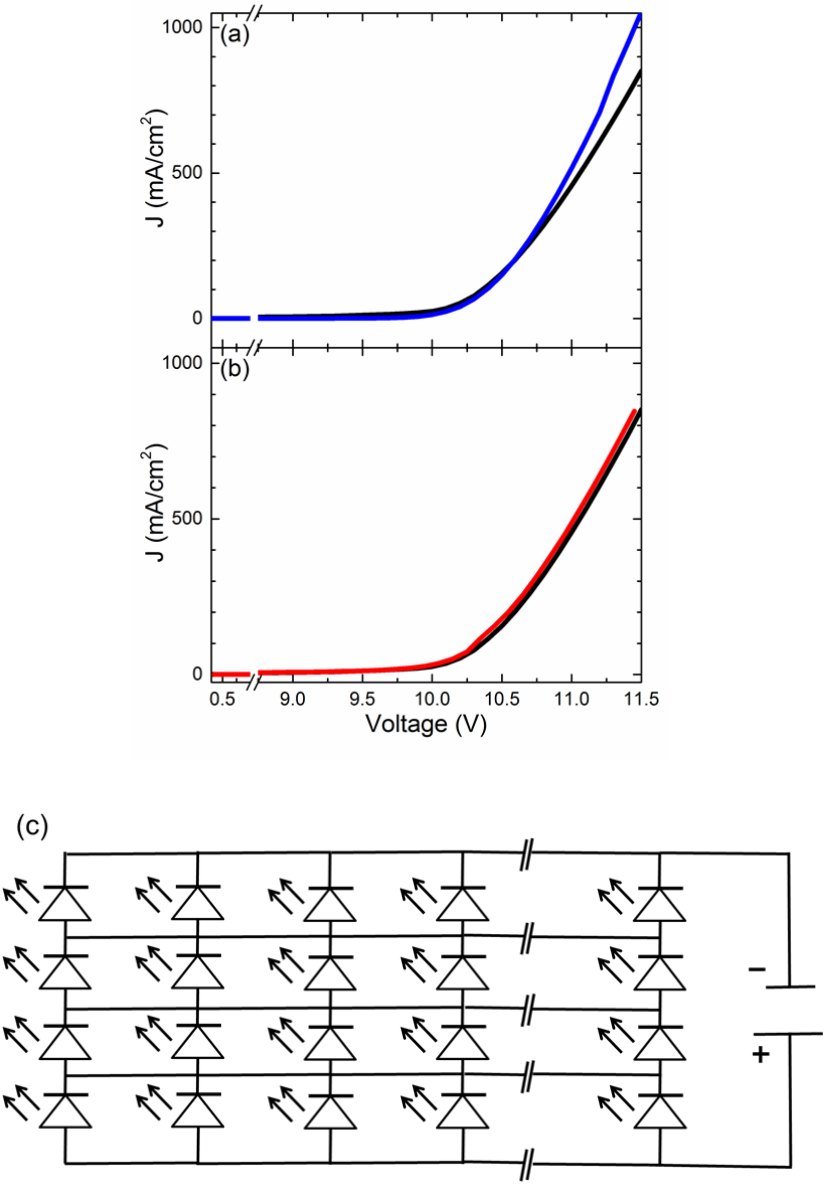

Figure 3.4: (a) J-V characteristics of a planar (blue) and of PQC (black solid line) LED. (b) J-V characteristics of a PQC LED (black solid line) and after hybridisation (red solid line) with QD-585. (c) Equivalent circuit of modular LED array, it consists of 80 micro LEDs arranged in 4 rows and 20 columns. Here to avoid repetition only 5 parallel LED arrays are shown instead of 20 parallel arrays.

LED modular chip consist of 80 micro LED chips that is four in series 20 and LED array in parallel. The 80 micro LEDs are electrically connected in configuration that voltage drop across each micro LED is the same. The equivalent circuit of modular array LED is shown figure 3.4 (c), for easy repetition only five parallel array of LED is shown instead of 20 parallel arrays. In case of local failure of micro LED the voltage drop across the micro LED will remain the same and current to micro LED will increase. This micro LED arrangement is chosen such that even in case of few micro LEDs failure brightness of module can be maintained. From J-V curves in figure 3.4 (b) we can see the turn-on voltage is ~10.3V, the voltage drop across each micro LED is 2.575V and the current density through the LED modular array chip is 78 mA/cm^2.

3.3.2 Electroluminescence spectra

A monochromatic colour conversion device was hybridised with QDs emitting at 585nm. Figure 3.5(a) shows the electroluminescence (EL) spectra before (black solid line) and after (red solid line) hybridisation along with the absorption spectrum of the QDs (orange dashed line). White light LEDs were fabricated using a blend of green, orange and red emitters (QD-535, QD-585, and QD-630). Figure 3.5(b) shows the EL spectrum of the PQC LED before (black solid line) and after (red solid line) hybridisation with the QD blend along with the absorption spectra of the different QD colors (green, orange and red dashed lines). We note the strong spectral overlap between the absorption of the various QDs and LED electroluminescence which is a prerequisite for efficient energy transfer between the MQW and QD emitters. The relatively narrow (~30 nm FWHM) QD luminescence maxima observable in the hybrid EL spectra are in a good agreement with PL properties of the QDs on glass. For both (the single color QD and blended QDs) cases, the EL maxima of the LED is found to be strongly quenched by presence of the QDs, indicating the presence of a significant energy transfer from MQW to QDs.

.

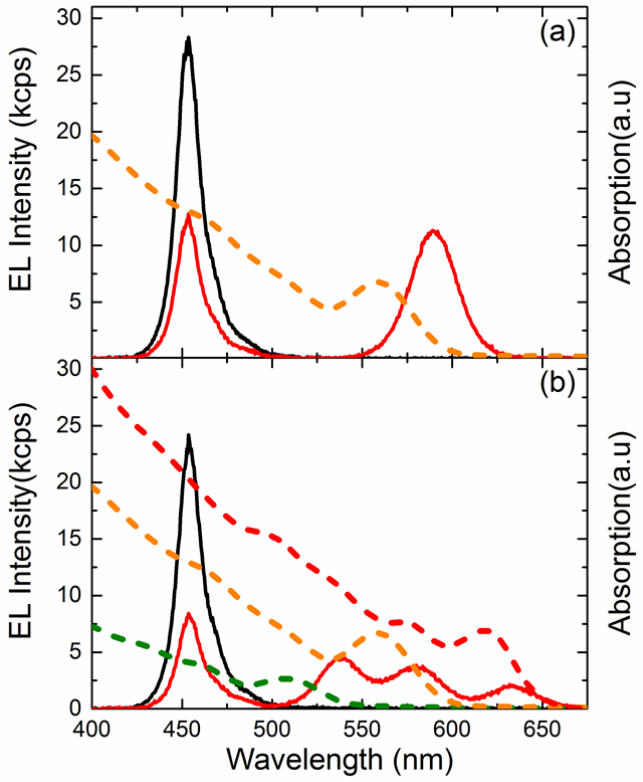

Figure 3.5: Electroluminescence spectra of PQC LED before (black solid line) and after hybridisation (red solid line) with (a) QD-585 and (b) with blend of QD-535, QD-585 and QD-630, along with absorption spectrum of QD-585 (orange dashed line) in (a) and the absorption spectrum of QD-535 (green dashed line) , QD-585 (orange dashed line) and QD-630 (red dashed line) in (b).

3.3.3 Colour Conversion efficiency

The overall amount of energy transfer from the MQWs to QDs, including both radiative and non-radiative RET, can be gauged using colour conversion efficiency (CCE), defined as the ratio of integrated luminescence intensity of QDs in hybridised structure to integrated luminescence intensity of MQWs in the bare device [12]:

$$\mathrm{CCE} = \frac{\int \mathrm{I}_{\mathrm{QDs}}^{\mathrm{Hybrid}}(\lambda)\mathrm{d}\lambda}{\int \mathrm{I}_{\mathrm{MQW}}^{\mathrm{Bare}}(\lambda)\,\mathrm{d}\lambda} \qquad (14)$$

Where λ is the wavelength of light, X in $\mathrm{I}_{\mathrm{X}}^{\mathrm{Y}}$ denotes EL intensity of the QDs or MQWs and Y is a bare or hybrid structures. Further on, the effective quantum yield (EQY) of a colour conversion process is estimated, defined as the ratio of number of photons emitted at QD wavelength to the number of photons effectively 'absorbed' at emission wavelength of MQWs:

$$EQY = \frac{\int I_{QDs}^{Hybrid}(\lambda)d\lambda}{\int I_{MQW}^{Bare}(\lambda)d\lambda - \int I_{MQW}^{Hybrid}(\lambda)d\lambda} \quad (15)$$

It is important to note that in the definition of the EQY, the denominator is given by the difference in the intensity of the MQWs before and after hybridisation. While some of this quenching is due to the QDs absorption at normal incidence to the epitaxy, deposition of the QDs also modifies the out-coupling efficiency [17] of the MQW emission in the plane of the epitaxy. This is especially the case for etched PQCs, where out-coupling efficiency strongly depends on refractive index contrast between the epitaxy and material filling of nanoholes. The latter results in an increase in lateral to the PQC emission intensity, which explains high values of EQY reported in the literature [20,21] (typically higher than the PL QY of QDs) and indeed the results presented in this chapter.

Figure 3.6 (a) shows both CCE and EQY of the QD-585 hybridised PQC LED as a function of injection current. With increasing driving currents, CCE is found to slightly increase and then remain virtually constant, with an average of 66.7% and a standard deviation of 0.8%. These values, much higher than the CCEs reported in Refs [12,22,14,23], are a strong indicator that the QDs efficiently couple to guided modes in the LED. The EQY of QDs is found on the other hand to be significantly dependent on injection current, with a gradual 9% relative increase from 25mA to its maximum value of 123% at ~70mA. It is conceivable that initial EQY increase is related to the thermal activation of trapped carriers in QDs [21], which would increase their PLQY. The decrease above 70mA is attributed to a temperature quenching of PLQY of the QDs, previously reported in the literature for such emitters [24]. The EQY maximum value of 123% represents a large 30% relative increase compared to the previous best reported values (~95% in Refs [20,21]). It is also important to note that this result was obtained with a standard off-the-shelf QDs with ~40% PLQY (see Ref. [25]). Since PLQY of QDs remains a bottleneck for all colour conversion processes, using state-of-the-art emitters providing PLQYs in excess of 80% [1,2] will potentially double the EQY of our devices and drastically improve LED performance.

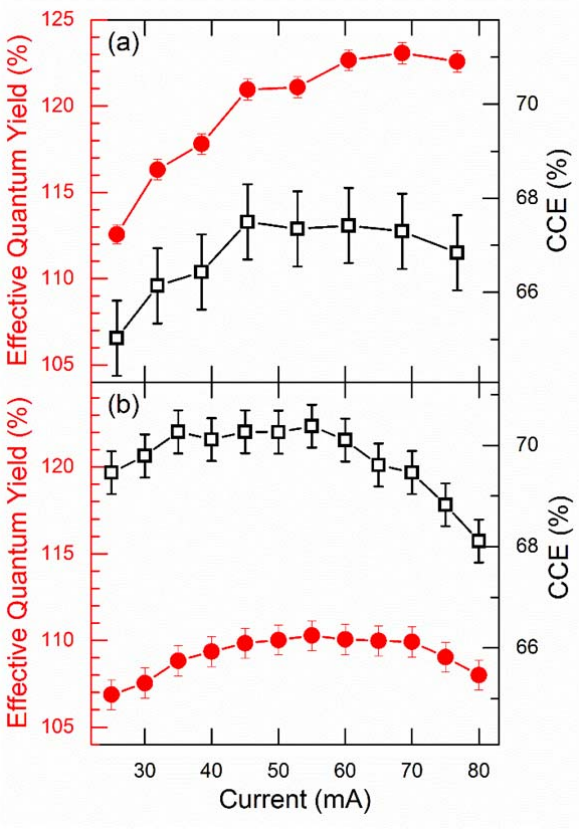

Figure 3.6: Effective quantum yield (red solid circles) and colour conversion efficiency (black open squares) of PQC hybridised with QD-585 in (a) and with the QD blend in (b). The solid lines are presented as a guide for the eye.

CCE and EQY of the device hybridised with QD blend (QD-535, QD-585, and QD-630) are plotted in Figure 3.6 (b) as a function of injection current. As in the previous case, both values are found to gradually increase with increasing current before reaching their maxima at approximately 60mA and dropping for higher currents. The CCE is found to be similar to the monochromatic case, with values ranging from 68% to 70%. This is a good indication that the overall QD density is similar for both blend and single color QD hybridised devices are in a good agreement with SEM cross-sectional studies indicating fully-filled nanoholes (see Figure 3.3 (b)). The EQY of white device is found on the other hand to be significantly decreased compared to the single colour QD case, with a maximum value of ~110%. This ~10% relative decrease from single colour QDs to a blend is attributed to energy transfer, both radiative and non-radiative, between the three different colors within the blend. Using state-of-the-art QDs with PLQY in excess of 80% would alleviate this mismatch to a significant extent.

3.3.4 CIE coordinates

The CIE (Commission Internationale de l'Éclairage) coordinates [18] of various hybrid PQC LEDs shown were calculated using their EL spectra and are displayed in Figure 3.7 for an injection current of 80mA. The white LED device was found to be at (0.312, 0.337) in the CIE map (red star) and its Correlated Colour Temperature (CCT) was calculated to be 6509K. These coordinates are a good match to the 6500K D65 daylight standard at (0.313, 0.329). Both CCT and CIE coordinates are found to remain stable for a range of injection currents (20-85mA), with small relative variations of ~5% across the current range. The CIE of PQC LED hybridised with QD-585 was found to be (0.3861, 0.2668) and is annotated in Figure 3.7 by a green circle. These coordinates were also found to be weakly dependent on the injection current between 20mA and 80mA. By tuning the ratio of various components of the tri-color QD blend, CCT could be tuned between 12928K and 6509K (black stars in Figure 3.7).

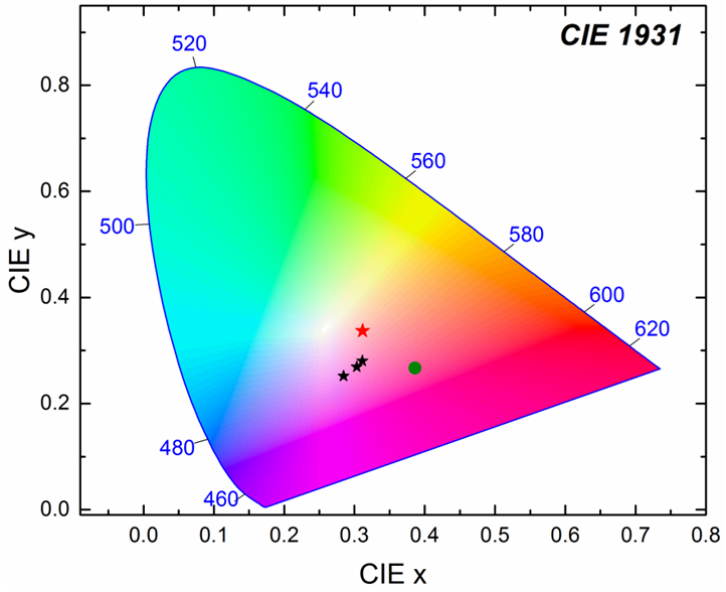

Figure 3.7: Chromaticity diagram indicating the CIE coordinates for PQC LEDs hybridised with QD-585(green circle), with the tri-color blend (red star) and for variations of blend ratio (black stars). Measurements are reported for 80mA injection current.

3.3.5 Time Resolved Spectroscopy

Time resolved photoluminescence (TRPL) spectroscopy was used to study non-radiative resonant energy transfer between MQWs and QD colour converters. The samples were excited at 380nm using a frequency-doubled Ti:Sapphire laser. The excitation density was kept constant at 40nJ/cm^2. The photoluminescence (PL) was detected using a fast APD and time-correlated single photon

counting electronics (~50ps temporal resolution). The PL decays of MQW before (black continuous) and after (red continuous) hybridisation with QD-858 (single color QD device) and with tri-color QD blend are displayed in Figure 3.8(a) and Figure 3.8 (b), respectively. The decay dynamics are found to be strongly accelerated after hybridisation, indicating the presence of an additional recombination channel in the MQWs attributed to RET. The decays were fitted with a double stretched exponential function [15]:

$$I(t) = Ae^{-\left((k_r+k_{RET})*t\right)^{\beta}} + Be^{-(k_r*t)^{\beta}} \quad (16)$$

where $I(t)$ is a time dependent PL intensity, k_r and k_{RET} are radiative and RET decay rates respectively, β is a stretched exponent, A denote a fraction of excitons close enough to the MQW sidewalls to undergo RET and B is a fraction of excitons that do not contribute to RET. The sum of A and B is kept constant and equal to one.

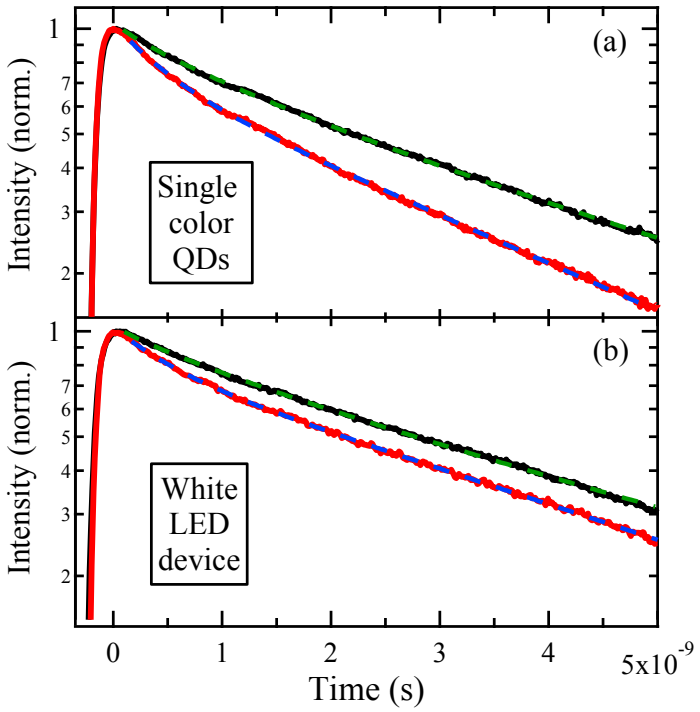

Figure 3.8: Time resolved photoluminescence decay of a PQC LED before (black) and after (red) hybridisation with QD-585 in (a) and with tri color QDs blend in (b). The dashed line indicates the best fit to experimental data.

In single colour QDs case, the bare decay was fitted by setting k_{RET} to zero, which yielded a radiative lifetime of 3.2ns and a β value of 0.82. In this fitting function, β represents a quality factor for the distribution of decay rates, with $\beta = 1$ indicating a single recombination channel. The high value of β indicates high quality of the nanohole sidewalls. The radiative and RET lifetimes were extracted by fitting the decay of the hybrid device, keeping β=0.82, which yielded radiative and RET lifetimes of 3.3ns and 0.57ns, respectively. Excellent agreement between radiative lifetimes of the hybrid and bare devices indicates that hybridisation does not impact the radiative exciton dynamics of the MQWs. This allows us to conclude that hybridisation with QDs does not affect or create surface recombination channels at MQW/QD interface. Nearly a quarter, 23%, of the MQW exciton population is found to participate to RET. The RET efficiency η_{RET}, calculated using the formula ($\eta_{RET} = \frac{k_{RET}}{k_{RET}+k_r}$), found to be 85%, is in a good agreement with previous reports [23,25]. From these numbers, the estimation can be made that $A * \eta_{RET} \simeq 20\%$ of the excitons in MQW transfer non-radiatively to QD emitters.

A similar analysis was carried out on white light device. Fitting PL decay of the bare structure yielded a radiative lifetime of 4.3ns and a stretching factor β of 0.89. The higher β value compared to single QD case indicate an improved sidewall surface quality (attributed to sample-to-sample variations), which result in a higher exciton radiative lifetime. A best fit of the PL decay of the structure hybridised with the tri-species blend, where β was kept constant and was equal to 0.89, provided radiative and RET lifetimes of 4.5ns and 0.92ns, respectively. The fraction of MQW excitons undergoing RET was found to be 22%, similar to single QD case. Calculating the RET efficiency yielded a value of 80%, in a good agreement with single QD species case and the literature.

3.4 Discussion

In a typical flat GaN LED grown on a sapphire wafer, only ~6% of the light is extracted towards the top transparent contact, while about 60 to 80% [26,27] of the light is trapped within the GaN slab due to the total internal reflection at GaN/air and GaN/sapphire interfaces, depending on LED configuration. About half of these photons are guided into higher order modes, potentially extractable using photonic crystal diffraction gratings or plasmonic structures, while the other half is guided into low order modes and remains mostly confined within GaN [27]. The evanescent field of these guided modes can extend up to 100nm in nanoholes for visible wavelength [28]. By etching nanoholes into MQW area, we allow our emitters to non-radiatively couple into both higher and lower order modes. The presence of this additional population of excitation, photons strongly enhances overall absorption of the QDs. This reasoning is especially true for PQCs compared to lower symmetry photonic crystals (PhCs). Indeed, the high symmetry of PQCs and the size of their Brillouin zones allow presence of large higher energy bands, while in PhCs only few modes are present. The modes making up this band can efficiently 'leak' into the nanoholes, where they are scattered out. In our hybrid structure, these modes can efficiently couple into the QD emitters. This

effect, combined with high 20% non-radiative energy transfer probability from MQW to QDs, can explain the very large effective EQY and CCE reported herein.

In conclusion, this chapter has demonstrated a high performance hybrid QD PQC LED geometry that provides record colour conversion performance. This is made possible by combining a high symmetry PQC geometry allowing high out-coupling efficiencies with good sidewall treatment, allowing to etch through the MQW active area without strongly damaging the electrical properties. These devices allow to place QD emitters in close proximity to MQWs, which enables non-radiative pumping of the emitters by MQW, and within GaN slab. This allows the QDs to couple to lower order guided modes within the epitaxy. This results into effective quantum yields for QD emitters reaching 123% for single QD species colour converters, and slightly lower values of ~110% for a tri-species white QD blend. These results surpass previous reports by more than 30%. This allow to fabricate a hybrid white LED with record colour-conversion performance and a quasi-perfect 6500K D65 spectrum. The performance of these hybrid devices, using 'off-the-shelf' QDs, could be strongly improved by utilising state-of-the-art nanocrystalline emitters, potentially doubling the color conversion effective quantum yield. The author believes that these hybrid PQC LED structures, fabricated with low-cost nano-imprint lithography and using cheap colloidal QD emitters, could potentially present an important technological breakthrough for the solid state lighting industry. This can be achieved by effectively integrating the colour conversion emitters into the epitaxy. The white LED chips could for instance, be incorporated into the edge-lighting strips of LED-backlit LCD displays. This approach will remove the need for colour conversion layer under the LCD stack and simplify the assembly of QD colour conversion displays and significantly lowering the manufacturing costs.

References

1. R. C. Page, D. Espinobarro-Velazquez, M. a Leontiadou, C. Smith, E. a Lewis, S. J. Haigh, C. Li, H. Radtke, A. Pengpad, F. Bondino, E. Magnano, I. Pis, W. R. Flavell, P. O'Brien, and D. J. Binks, "Near-unity quantum yields from chloride treated CdTe colloidal quantum dots.," Small **11**, 1548–54 (2015).

2. A. B. Greytak, P. M. Allen, W. Liu, J. Zhao, E. R. Young, Z. Popović, B. Walker, D. G. Nocera, and M. G. Bawendi, "Alternating layer addition approach to CdSe/CdS core/shell quantum dots with near-unity quantum yield and high on-time fractions.," Chem. Sci. **3**, 2028–2034 (2012).

3. Y. Shirasaki, G. J. Supran, M. G. Bawendi, and V. Bulović, "Emergence of colloidal quantum-dot light-emitting technologies," Nat. Photonics **7**, 13–23 (2013).

4. X. Dai, Z. Zhang, Y. Jin, Y. Niu, H. Cao, X. Liang, L. Chen, J. Wang, and X. Peng, "Solution-processed, high-performance light-emitting diodes based on quantum dots," Nature **515**, 96–99 (2014).

5. B. S. Mashford, M. Stevenson, Z. Popovic, C. Hamilton, Z. Zhou, C. Breen, J. Steckel, V. Bulovic, M. Bawendi, S. Coe-Sullivan, and P. T. Kazlas, "High-efficiency quantum-dot light-emitting devices with enhanced charge injection," Nat. Photonics **7**, 407–412 (2013).

6. Y.-R. Wu, Q. Yan, S. P. DenBaars, C. Van de Walle, H. Fu, S. Nakamura, Y. Zhao, and C.-C. Pan, "High optical power and low-efficiency droop blue light-emitting diodes using compositionally step-graded InGaN barrier," Electron. Lett. **51**, 1187–1189 (2015).

7. Y. N. and M. I. and D. S. and M. S. and T. Mukai, "White light emitting diodes with super-high luminous efficacy," J. Phys. D. Appl. Phys. **43**, 354002 (2010).

8. "World's First Quantum Dot-Based Monitor," http://coloriq.com/press_release/worlds-first-quantum-dot-based-monitor-with-color-iq-technology-is-now-available-from-philips/.

9. J. J. Wierer, A. David, and M. M. Megens, "III-nitride photonic-crystal light-emitting diodes with high extraction efficiency," Nat. Photonics **3**, 163–169 (2009).

10. C. Wiesmann, K. Bergenek, N. Linder, and U. T. Schwarz, "Photonic crystal LEDs - designing light extraction," Laser Photonics Rev. **3**, 262–286 (2009).

11. M. D. B. Charlton, P. Lagoudakis, and S. Chanyawadee, "Optical device with non radiative energy transfer," U.S. patent WO2010092362 A3 (2010).

12. F. Zhang, J. Liu, G. You, C. Zhang, S. E. Mohney, M. J. Park, J. S. Kwak, Y. Wang, D. D. Koleske, and J. Xu, "Nonradiative energy transfer between colloidal quantum dot-phosphors and nanopillar nitride LEDs," Opt. Express **20**, A333 (2012).

13. Y. C. Shin, D. H. Kim, E. H. Kim, J. M. Park, K. M. Ho, K. Constant, J. H. Choe, Q. Han Park, H. Y. Ryu, J. H. Baek, T. Jung, and T. G. Kim, "High efficiency gan light-emitting diodes with two dimensional photonic crystal structures of deep-hole square lattices," IEEE J. Quantum Electron. **46**, 116–120 (2010).

14. M. J. Park, K. J. Choi, and J. S. Kwak, "Enhanced color-conversion efficiency between colloidal quantum dot-phosphors and nitride LEDs by using nano-patterned p-GaN," J. Electroceramics **33**, 2–6 (2014).

15. C. Krishnan, M. Brossard, K.-Y. Lee, J.-K. Huang, C.-H. Lin, H.-C. Kuo, M. D. B. Charlton, and P. G. Lagoudakis, "Hybrid photonic crystal light-emitting diode renders 123% color conversion effective quantum yield," Optica **3**, 503–509 (2016).

16. Huang, Jian-Jang, H.-C. Kuo, and S.-C. Shen, *Nitride Semiconductor Light-Emitting Diodes (LEDs): Materials, Technologies and Applications* (Woodhead Publishing, 2014).

17. N. Ganesh, W. Zhang, P. C. Mathias, E. Chow, J. a N. T. Soares, V. Malyarchuk, A. D.

Smith, and B. T. Cunningham, "Enhanced fluorescence emission from quantum dots on a photonic crystal surface," Nat. Nanotechnol. **2**, 515–520 (2007).

18. N. Ohta and A. Robertson, *Colorimetry: Fundamentals and Applications* (John Wiley & Sons, 2006).

19. J. Bai, Q. Wang, and T. Wang, "Greatly enhanced performance of InGaN/GaN nanorod light emitting diodes," Phys. Status Solidi Appl. Mater. Sci. **209**, 477–480 (2012).

20. V. Wood and V. Bulović, "Colloidal quantum dot light-emitting devices," Nano Rev. **1**, 1–7 (2010).

21. J. S. Steckel, J. Ho, C. Hamilton, C. Breen, W. Liu, P. Allen, J. Xi, and S. Coe-Sullivan, "Quantum dots: The ultimate down-conversion material for LCD displays," Dig. Tech. Pap. - SID Int. Symp. **45**, 130–133 (2014).

22. M. Achermann, M. a. Petruska, D. D. Koleske, M. H. Crawford, and V. I. Klimov, "Nanocrystal-based light-emitting diodes utilizing high-efficiency nonradiative energy transfer for color conversion," Nano Lett. **6**, 1396–1400 (2006).

23. S. Chanyawadee, P. G. Lagoudakis, R. T. Harley, M. D. B. Charlton, D. V. Talapin, H. W. Huang, and C. H. Lin, "Increased color-conversion efficiency in hybrid light-emitting diodes utilizing non-radiative energy transfer," Adv. Mater. **22**, 602–606 (2010).

24. Y. Zhao, C. Riemersma, F. Pietra, R. Koole, C. de Mello Donegá, and A. Meijerink, "High-Temperature Luminescence Quenching of Colloidal Quantum Dots," ACS Nano **6**, 9058–9067 (2012).

25. M. Brossard, C.-Y. Hong, M. Hung, P. Yu, M. D. B. Charlton, P. G. Savvidis, and P. G. Lagoudakis, "Novel Non-radiative Exciton Harvesting Scheme Yields a 15% Efficiency Improvement in High-Efficiency III-V Solar Cells," Adv. Opt. Mater. **3**, 263–269 (2015).

26. M. D. B. Charlton, "Photonic crystal nitride LEDs," in *Nitride Semiconductor Light-Emitting Diodes (LEDs): Materials, Technologies and Applications* (Woodhead Publishing, 2014), pp. 301–354.

27. A. David, T. Fujii, R. Sharma, K. McGroddy, S. Nakamura, S. P. DenBaars, E. L. Hu, C. Weisbuch, and H. Benisty, "Photonic-crystal GaN light-emitting diodes with tailored guided modes distribution," Appl. Phys. Lett. **88**, 61124 (2006).

28. F. S. Diana, A. David, I. Meinel, R. Sharma, C. Weisbuch, S. Nakamura, and P. M. Petroff, "Photonic crystal-assisted light extraction from a colloidal quantum Dot/GaN hybrid structure," Nano Lett. **6**, 1116–1120 (2006).

Chapter 4: Colour tunable light emitting diodes

4.1 Introduction

Chapter 3 showed the possibility to achieve high performance colour conversion using hybrid PQC LED. The aim of this work is to demonstrate reproducible and spectrally tunable hybrid PQC LED. For this purpose, the modular array LED design was modified to have six sub modules with separate p and n contact pads. Hybridisation of these six modules with suitable QDs, it is possible to tune the wide range of CIE co-ordinates.

4.2 Materials and Methods

4.2.1 Fabrication of CCT tunable LEDS

The devices studied in this chapter consist of GaN/InGaN MQW LEDs on patterned sapphire substrate (PSS), which were fabricated using low-cost nanoimprint lithography and plasma etched to form 12-fold symmetric quasi crystals (PQC). To complete the modular array LED chip, the PQC wafer was processed using link chip process. ITO and mesa layer were etched using a standard chip process, which utilised photolithography, wet- and dry-etching steps similar to process flow of modular array LED chip described in Appendix A.1. Design of the modular array LED was modified to accommodate six modules with separate pn pads. This gives the flexibility of driving six modules with different injection currents.

The QDs used for colour tuning LED were Trilite Fluorescent Nanocrystals procured from Cytodiagnostics. These CdS_xSe_{1-x}/ZnS core/shell colloidal semiconductor QDs (oleic acid capped) were found to have 1s emission peaks at 535±15nm (herein, QD-535), 585±15nm (QD-585), 630±15nm (QD-630), 665±5nm (QD-665) and 1s absorption peaks at 515nm, 560nm, 620nm and 650nm respectively. These QDs with different emission peak were deposited on to the designated module as shown in schematic (Figure 4.1). Drop casting was chosen to be the initial method of deposition, which was extended further to inkjet printing to achieve precise control of the deposition

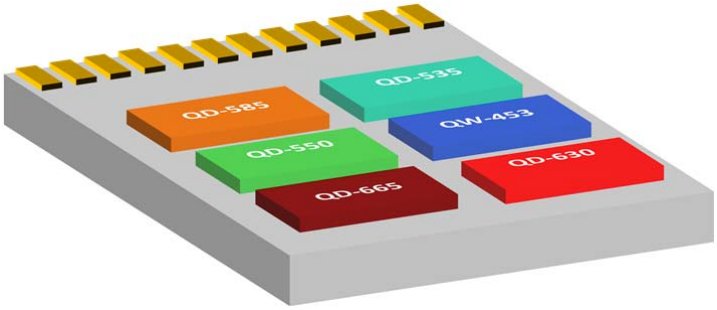

Figure 4.1: Schematic of hybrid CCT tuneable LED with QD -535, QD-550,QD-585,QD-630 and QD-665. QW-453 is QW with emission peak at 453nm.

4.2.2 QD deposition: drop casting

The Colloidal QDs are diluted in toluene to concentration of 10mg/ml using parallel dilution technique. Two micro litre of QD solution is dispensed using micropipette onto the designated module. A cycle of dry and drop casting is followed to cover the designated module with required QDs. This deposition method creates coffee ring effect with more QDs deposited on to the edges compared with the centre. In addition, cross contamination between adjacent modules was also found. Two possible solutions to overcome this problem is either drop cast the QDs while the substrate is heated or use of inclined angle deposition. Heating of QDs [1] degrade the quality of QDs which in return reduces the photoluminescence quantum yield. Inclined angled deposition method was chosen to deposit QDs on to the designated module. Inclined angle deposition setup is as shown in figure 4.2 (a). Micrometre stage holding the micropipette gives the precise controlled movement of x axis, y axis and z axis. The LED chip to be drop casted is placed on a rotating stage to control the angle of contact between the LED chip and micropipette tips. Using micrometre stage, the micro pipette containing QD solution is brought in close proximity to LED chip and then drop casted. Figure 4.2 (b) shows the image of LED module while drop casted using the inclined angle drop casting technique.

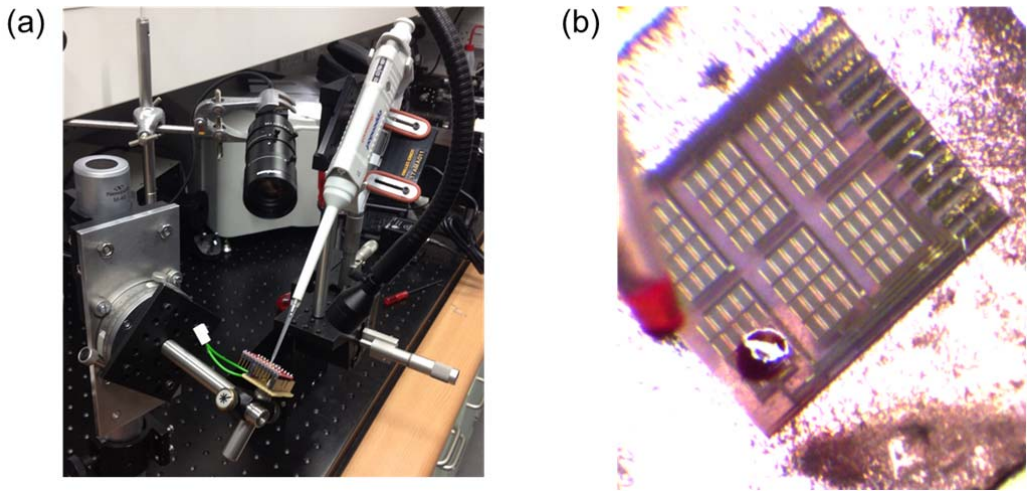

Figure 4.2: (a) Photograph of inclined angle drop casting setup (b) Image of LED chip drop casted with QD-630 using inclined angle drop casting.

Although by using this method, the controlled deposition for targeted location was slightly improved but it still suffered from cross contamination and was unable to control the thickness of the layer. This demands a sophisticated QD deposition technique like contact printing [2], mist deposition [3],spray coating [4,5] or inkjet printing [6–8]. Contact printing involves an additional processing step like creating mould for lithography but it still results in poor control over thickness. The consumption of QD solution in mist deposition [7] is higher, resulting in wastage of expensive colloidal QDs. Whereas, spray coating and ink printing minimises the waste of QDs and are capable of scaling down to commercial production. Therefore, the ink jet printing is used in this work to fabricate the colour tuneable light emitting diodes.

4.2.3 QD deposition: Inkjet printing

Inkjet printing of QDs on the LEDs were carried out using Dimatix material printer (DMP-2800) by FujiFilm. The inkjet printing is capable of printing on area of 210mm× 315mm using 16 inkjet nozzles. One nozzle is used to print 5mm× 5mm LED module. Figure 4.3(a) shows the nozzle from where QD solution is ejected and figure 4.3(b) shows the QD droplet ejection. The formation of QDs droplets and their ejection is controlled by voltage-time waveform, which in turn controls the piezo-electric print head. The voltage controls the amount of QD solution pumped into the chamber while the slew rate determines the volume change. The detailed ejection recipe developed for QDs solution for concentration of 10mg/ml is shown in appendix (B.1). To ensure high resolution of printing, the spacing between ejected droplets was set to 5µm. Printing was carried in ambient conditions at room temperature. The QDs solutions were prepared to concentration of 10mg/ml, for achieving a desired droplet velocity (6 to 9 meter/second) used for inkjet printing.

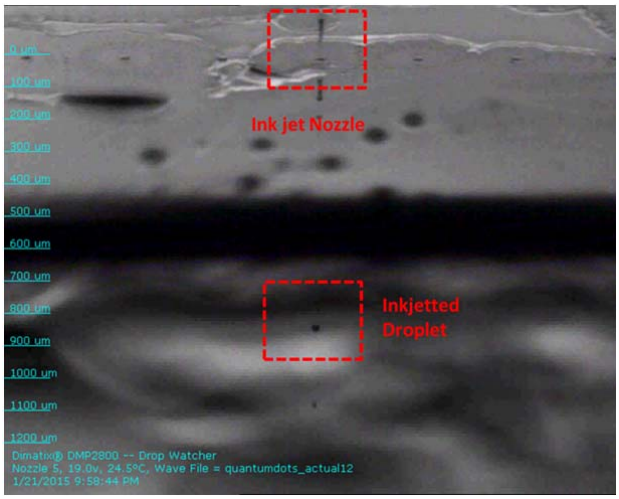

Figure 4.3: Screen capture of QDs ejection from the nozzle and ejected QD droplet

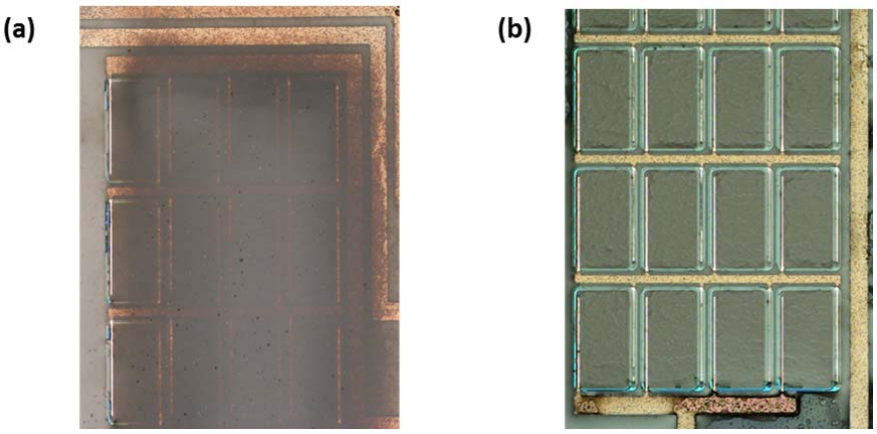

Figure 4.4: (a) Microscopic image (×10 magnification) of LED module flooded with QD solution ejected at higher velocity (> 12m/s) (b) shows LED module inkjet printed with QDs at ejection speed of 6m/s.

Figure 4.3 shows the screen capture of QDs ejected at the speed of 6m/s. Ejection at higher or lower speeds will result in doubling or omitting of the deposition respectively. LED module printed with higher velocities (> 12m/s), result in QD solution flooding as shown in Figure 4.4 (a). For comparison purposes, figure 4.4 (b) shows the LED module ink ejected at desired drop velocity.

4.2.4 Characterisation Method

For characterisation, the LED spectra and intensities were measured inside a six-inch integration sphere coupled to a TE-cooled BWtek spectrometer. The morphology and thickness of the QDs on LED module was characterised using Zeiss Nvision 40 FIB-SEM and Nikon microscope.

4.3 Device Characterisation

4.3.1 CCT tuneable LEDs using drop casting

The device studied in this section consists of GaN/InGaN MQWs grown on top of patterned sapphire substrate then 12-fold PQC are patterned by nanoimprint method. The LED wafer with PQC was processed through link chip process. The fabricated LED has six sub modules with the aim of hybridising using different emissions of QD to cover the visible spectrum. By effectively tuning the emission intensities of modules, it is possible to tune CCT and CIE co-ordinates. Four modules was drop casted with QD-535, QD-585, QD-630 and QD 665 respectively. Inclined angle deposition method, described in section 4.2.2, was carried for drop casting. Although the chip contained six modules, only four were used due to cross-contamination between adjacent modules. Figure 4.5 (a) and (b) shows the schematic and an image electrically excited CCT tunable LED hybridised with inclined drop casting.

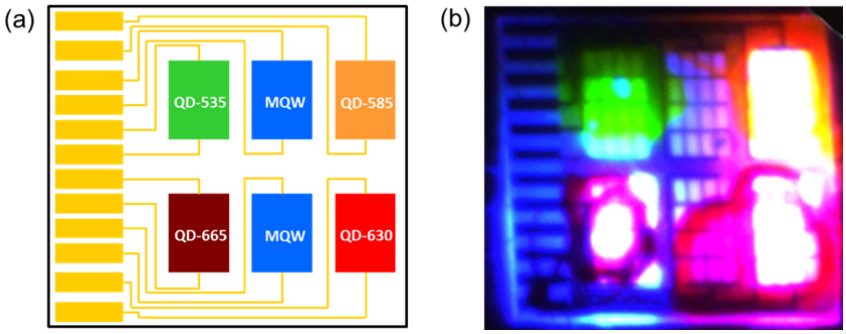

Figure 4.5: (a) Schematic of CCT tunable LED with different QDs deposited. (b) An image of a CCT tunable LED hybridised with QD-535, QD-585, QD-630 and QD-665.

Figure 4.6 (a) shows the normalised electroluminescence spectra of individual modules after hybridised with QDs and their relative intensity can be controlled by injection current. The corresponding CIE coordinates of hybridised modules (black squares) are shown in figure 4.6 (b). The EL spectra (figure 4.6 (a)) and CIE coordinates (figure 4.6 (b)) are measured at current density of 110mA/cm^2. By tuning the intensity of LED modules, the CCT is tuned from 2888K to 5153k (red stars in Figure 4.6 (b)). The colour rendering index (CRI) of corresponding CIE coordinates is shown in table2. The CRI of CCT LED is 82% at 2888K and this is above minimum recommended CRI 80% for interior lighting. The colour gamut of CCT tuneable LED is governed by EL spectra of the LED modules.

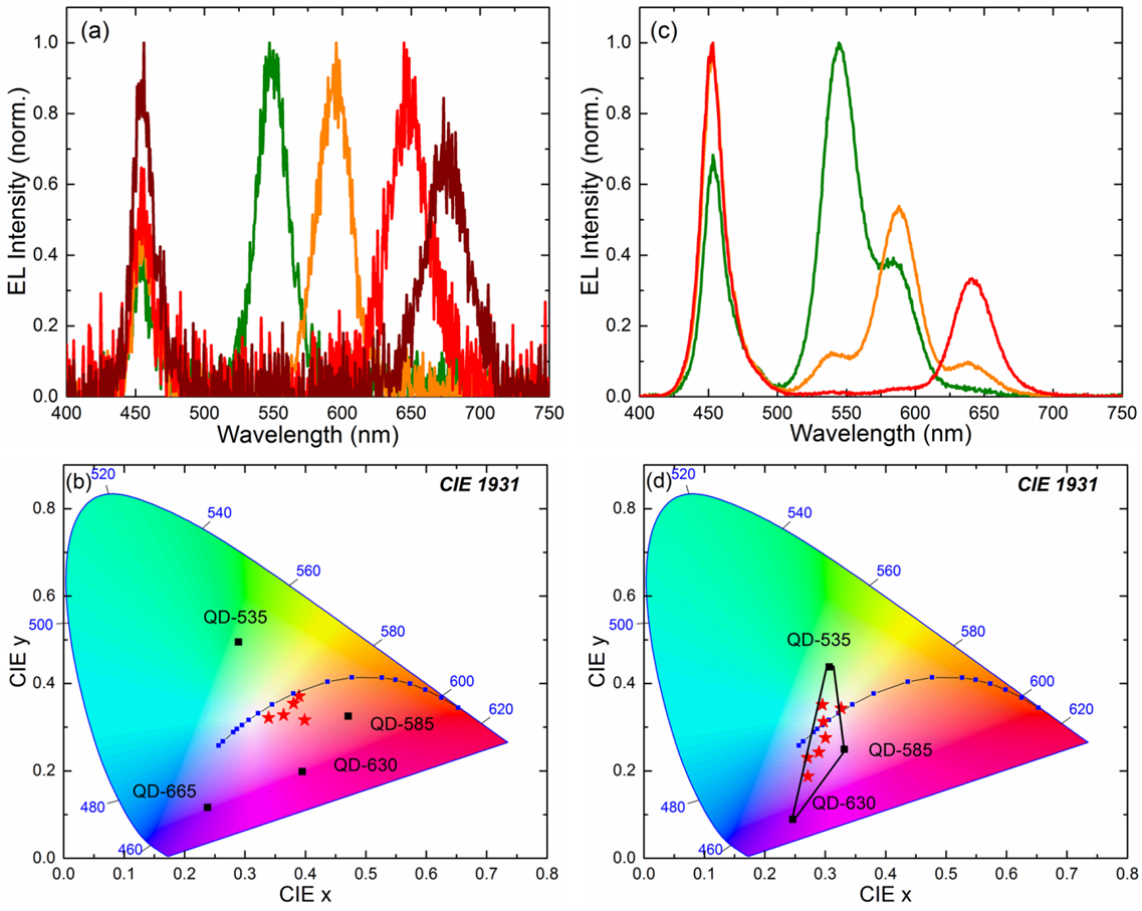

Figure 4.6: Shows the electroluminescence spectra and CIE co-ordinates for drop casted hybrid LEDs. The results of Inclined angled drop casted hybrid LEDs are shown in (a) and (b). For comparison (c) and (d) shows conventional drop casted hybrid LED. (a) Normalised electroluminescence (EL) spectra of LED modules hybridised with QD-535 (green solid line), QD-585(orange solid line), QD-630(red solid line) and QD-665 (wine red solid line). (b) Chromaticity diagram indicating CIE coordinates of hybridised LED modules (black squares) and some of their tuneable CIE -coordinates (red stars). (c) Normalised EL spectra for drop casted LED module with QD-535(green), QD-585 (orange) and QD-630 (red). (d) Black square represents the CIE coordinates of (c) with some spectrally tunable CIE coordinates (red stars).

Normalised EL spectra (Figure 4.6 (c)) and CIE plot (4.6 (d)) of conventional drop casting is also shown for comparison along with inclined angle deposition. Only three QDs (QD-535, QD-575, and QD-630) were drop casted due to increased overlap of QDs deposition, which is observable from their EL spectra (figure 4.6 (c)). Black squares in figure 4.6(d) correspond to CIE coordinates of the spectrum in figure 4.6(c). Similar to previous observations, it is possible to tune the CIE coordinates (red stars, figure 4.6 (d) within the colour gamut.

Table 2: CIE coordinates, correlated colour temperature (CCT) and colour rendering index (CRI) for colour tunable LED shown in figure 4.6(b)

CIE co-ordinates (x,y)	CCT	CRI/ LED modules
0.29,0.49	-	QD-535
0.47,0.33	-	QD-585
0.39,0.2	-	QD-630
0.24,0.12	-	QD-665
0.4,0.32	2888K	82.7%
0.39,0.37	3708K	59.8%
0.38,0.35	3819K	57.8%
0.36,0.33	4116K	76.1%
0.34,0.32	5153K	68.3%

4.3.2 Colour tunable LEDs using inkjet printing

In section 4.3.1, the importance of QD deposition at respective LED module was discussed. For this purpose, ink jet printing technology was preferred. Figure 4.7 (a) shows the LED module printed with 2 layers, 4 layers and 16 layers from top to bottom respectively. Figure 4.7 (b) shows the magnified image of 16 layers and Figure 4.7 (c) shows the electro luminescence of LED modules printed with QD-630 and QD- 535. The developed recipe for inkjet printing enables high precision of printing where single layer has the thickness of 150nm and 15 layers have the thickness equal to 2.77µm. Figure 4.8 (a) and (b) shows the top and cross-sectional view of 16 layers.

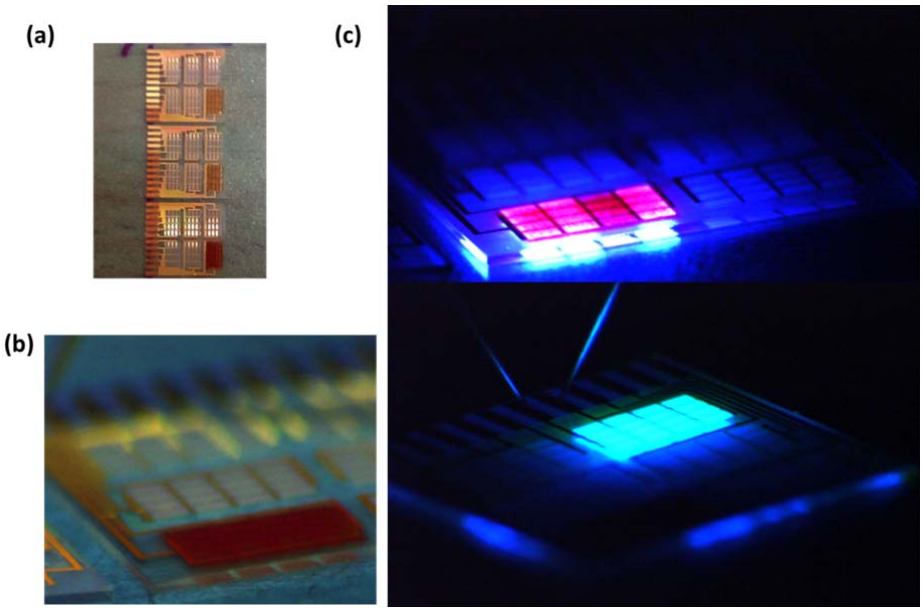

Figure 4.7: (a) LED modules with printed with 2 layer, 4 layers and 15 layers of QD from top to bottom (b) Magnified image of LED modules printed with 15 layer of QD-630 (c) EL of LED module printed with 15 layer of QD-630(top) and QD-535(bottom) at current density 110mA/cm^2.

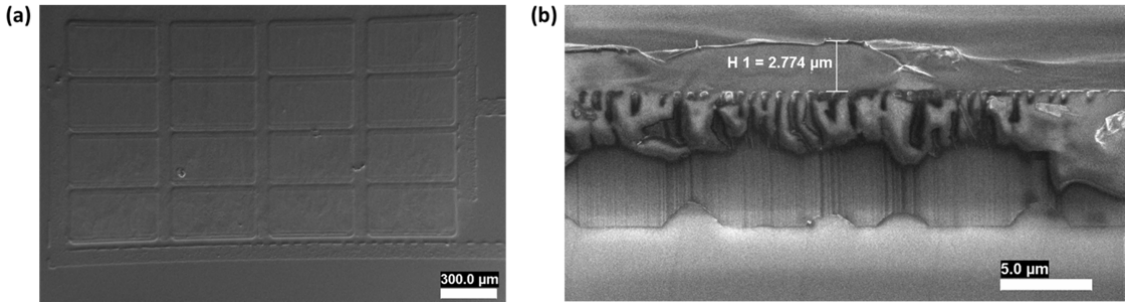

Figure 4.8: (a) SEM image of LED module after printing with 16 layer of QD-630 (b) Cross sectional SEM image of figure 4.8(a) shows 2.77µm thick QD layer.

For reproducibility comparison of inkjet printing, two CCT tunable LEDs were printed with 16 layers of QD-535, QD-550, QD-585, QD-630 and QD-665. Injection current was set to 2mA and CIE co-ordinates of LED modules were compared. Black squares and red stars in Figure 4.9 represent CIE coordinates of LED modules of two CCT tuneable LED chips. The CIE co-ordinates of figure 4.9 is shown in table 3. Good reproducibility of CIE co-ordinates with ±0.2 deviation in x or y coordinates for QD-550, QD-585, QD-630 and QD-665 can be observed. This variation is due to intensity variation in LED chip and printing in ambient condition. Despite the fact that both chips are processed simultaneously, intensity variation can arise due to the variability between different chips.

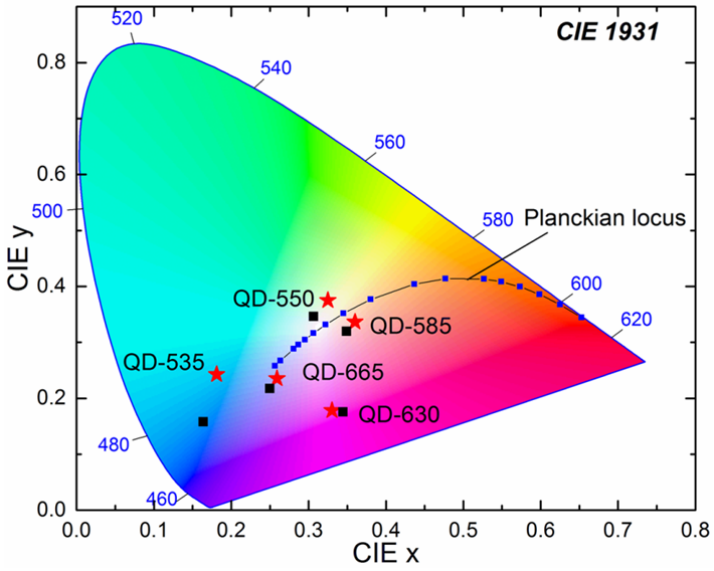

Figure 4.9: Chromaticity diagram indicating CIE coordinates for inkjet printed colour tunable LEDs (Black square and red stars).

Table 3: CIE coordinates of two CCT tuneable LED chips (Figure 4.9) is represented by black squares and red stars respectively

CIE co-ordinates (x,y) (black squares)	CIE coordinates (x,y) (red stars)	LED module
0.16,0.16	0.18,0.24	QD-535
0.31,0.35	0.32,0.37	QD-550
0.35,0.32	0.36,0.33	QD-585
0.34,0.18	0.33,0.18	QD-630
0.25,0.22	0.25,0.24	QD-665

Another reason for variation is due to printing in atmospheric conditions, which causes evaporation of the solvent (toluene) during printing. Evaporation of the toluene causes change in the concentration and affects the droplet volume. Using vacuum chamber or glove box can reduce this deviation. Significant variation of CIE co-ordinates for QD-535 is due to the variation in quantum yield of the QDs. Therefore, by using the QDs with same quantum yield, this deviation can be reduced.

4.4 Conclusion

This work has shown that hybrid PQC LED module can achieve CCT tunability between 2888K and 5153K. By using three or four different types of QD, the possibility to tune CIE co-ordinates governed by colour gamut of hybridised LED modules is also shown. A precise deposition of QDs can be achieved using the inkjet printing. It also gives the freedom of printing multiple layers. A good reproducibility for CIE coordinates of two CCT tuneable LED chips with inkjet printing was achieved. This technique can also be extended to QD based LED displays.

References

1. Y. Zhao, C. Riemersma, F. Pietra, R. Koole, C. de Mello Donegá, and A. Meijerink, "High-Temperature Luminescence Quenching of Colloidal Quantum Dots," ACS Nano **6**, 9058–9067 (2012).

2. L. Kim, P. O. Anikeeva, S. a. Coe-Sullivan, J. S. Steckel, M. G. Bawendi, and V. Bulović, "Contact printing of quantum dot light-emitting devices," Nano Lett. **8**, 4513–4517 (2008).

3. T. Zhu, K. Shanmugasundaram, S. C. Price, J. Ruzyllo, F. Zhang, J. Xu, S. E. Mohney, Q. Zhang, and a. Y. Wang, "Mist fabrication of light emitting diodes with colloidal nanocrystal quantum dots," Appl. Phys. Lett. **92**, 15–18 (2008).

4. K.-J. Chen, H.-C. Chen, K.-A. Tsai, C.-C. Lin, H.-H. Tsai, S.-H. Chien, B.-S. Cheng, Y.-J. Hsu, M.-H. Shih, C.-H. Tsai, H.-H. Shih, and H.-C. Kuo, "Resonant-Enhanced Full-Color Emission of Quantum-Dot-Based Display Technology Using a Pulsed Spray Method," Adv. Funct. Mater. **22**, 5138–5143 (2012).

5. Y.-K. Liao, M. Brossard, D.-H. Hsieh, T.-N. Lin, M. D. B. Charlton, S.-J. Cheng, C.-H. Chen, J.-L. Shen, L.-T. Cheng, T.-P. Hsieh, F.-I. Lai, S.-Y. Kuo, H.-C. Kuo, P. G. Savvidis, and P. G. Lagoudakis, "Highly Efficient Flexible Hybrid Nanocrystal-Cu (In, Ga) Se2 (CIGS) Solar Cells," Adv. Energy Mater. **5**, 1401280 (2015).

6. A. M. Elliott, O. S. Ivanova, C. B. Williams, and T. a. Campbell, "Inkjet printing of quantum dots in photopolymer for use in additive manufacturing of nanocomposites," Adv. Eng. Mater. **15**, 903–907 (2013).

7. H. M. Haverinen, R. a. Myllylä, and G. E. Jabbour, "Inkjet printing of light emitting quantum dots," Appl. Phys. Lett. **94**, 12–15 (2009).

8. C. Lin, C. Hung, P. Kuo, and M. Cheng, "Display Technology Letters," J. Disp. Technol. **8**, 681–683 (2010).

Chapter 5: Quantum dots as route to enhance the performance of Si solar cells

5.1 Introduction

Silicon based photovoltaics are leading the global market with more than 92% of market and will lead the market for following years with the same trend. The efficiency of lab based Si solar with sophisticated anti-reflection coating and passivation are ~25% [1] [2]. If efficiency of the solar cell needs to further improve then this can be achieved through efficient photon management. Nano structures [3] [4] and pyramids [1] along with antireflection coating have been put forward as an efficient strategy in photon management. Another interesting strategy is to use QDs as light absorbers and shift the wavelength down where the quantum efficiency of solar cell is high. CdSe/ZnS(core/shell) [5] and PbS QDs [6] as luminescent down shifters (LDS) were shown in silicon solar cells. The QDs in these devices were deposited on top of anti-reflective coating and this architecture benefits from LDS only. In this configuration, the solar cell only benefits from the LDS. If suitable QDs are placed close to the silicon, it is possible to transfer excitons efficiently from QDs to the silicon through RET [7].

In this chapter, QDs are deposited as the superficial layer on polished silicon solar cell and interaction mechanism with underline silicon solar is investigated. Two types of QDs PbS and CdSe/ZnS are used to hybridise the solar cell. The PbS and CdSe/ZnS were chosen to have their emission peaks at infra-red and visible region respectively. In first section, PbS with 900nm peak emission is deposited on top of Si solar cell, enhanced solar cell performance is observed. The contribution of refractive index matching, LDS, RET and scattering from QD aggregate will be shown. In second section, the Si solar cell is hybridised with CdSe/ZnS and the existence of RET transfer is demonstrated with time resolved photoluminescense measurements. In the final section, the CdSe/ZnS QD layer on top of Si solar cell is optimised to maximise the Jsc enhancement. The opitimum thickness of QD layer was determined from absorption and external quantum efficiency (EQE) measuements.

5.2 Materials and Methods

5.2.1 Fabrication of hybrid Silicon/QDs Solar cells

Monocrystalline silicon (c-Si) solar cells were produced by Q CELLS in Germany. It is an n^+pp^+ c-Si solar cell without contacts and antireflective coating. The doping profile of phosphorus atom is shown in appendix C1. The doping of phosphorus atom was controlled to form metallurgical junction at depth of 400nm. The rear of solar cell is highly doped with boron atom, to serves as a back surface field and provides ohmic contact with aluminum back contact. Chromium (Cr) layer about 100nm was evaporated on to the n+ emitter using e-beam. Cr serves as a front contact electrode. For a rear contact of the solar cell, a 500nm aluminum layer is evaporated via E-beam. S1813 photoresist was spun on top of the front contact (Cr). Direct laser writing was used to expose the areas where Cr need to removed which was then developed and wet etched using Cr etchant followed by dicing. The devices were then micro bonded to printed circuit board (PCB) for characterisation. The active area of device was measured to be 5.76 mm^2. Lead sulphide (PbS) core QDs with emission wavelength of 900nm (QD-900) were used to hybridise the solar cells. The QDs are capped with oleic acid and their 1s absorption peak was found to be at 825nm wavelength. PbS colloidal QDs were dispersed in octane with a concentration of 12.5mg/ml. Dynamic spin coating technique was then used to hybridise the Si solar cells. Figure 5.1 (a) shows the schematic of hybrid Si solar cell. The surface morphology of QDs layer deposited can be seen from the AFM image shown in figure 5.1(b). Cross-sectional scanning electron microscope (SEM) image (fig 5.1(c)) shows the 35nm thick QD layer.

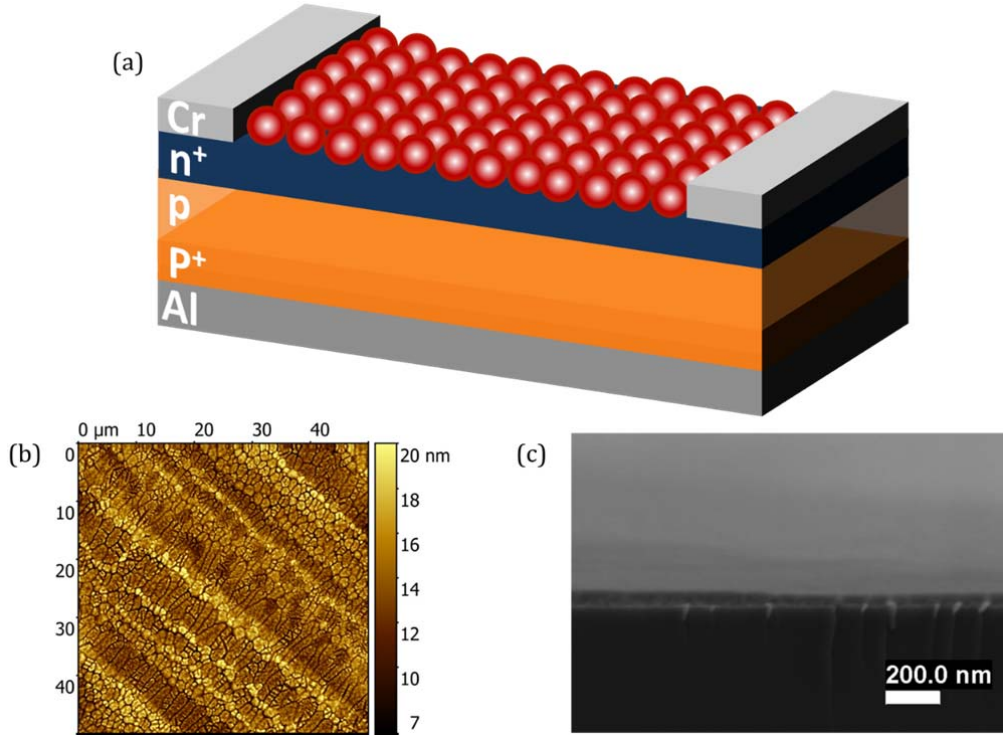

Figure 5.1: (a) Schematic representation, (b) AFM image showing surface morphology of QDs deposited and (c) Cross-sectional SEM image showing thickness of QDs layer.

5.2.2 Characterisation Method

Bentham PV300 commercial photovoltaic characterisation system was used to measure the reflectance of the solar cells. Dual Xenon/Quartz halogen lamp is used as a source lamp and the light from the source is coupled into monochromator via parabolic reflector and lenses. Specific wavelength from monochromator passes through the entrance port of integration sphere to the sample (or reference sample) placed at reflectance port using 45 degree reflecting mirror. Reflection of the solar cell is determined by the ratio of signals (I_s/I_{ref}) in Si photodiode. Where I_s is a sample signal reflectance and I_{ref} is the reflectance from integration sphere without the sample and absorption of solar cell is then calculated from reflection.

Illuminated I-V and the solar cell efficiency was characterised using solar simulator by Abet technologies. Xenon short arc lamp with AM1.5G filter produces one sun illumination over a 110×110mm field. Reference photodiode was used for the calibration of the system.

PV300 system was used to determine the External Quantum Efficiency (EQE) for tuneable wavelengths between 300nm and 1000nm. A square probe light with an area of 3.24mm^2 at specific wavelength is focussed on to the sample (or reference Si photodiode) and spectral responsivity was then measured. EQE can be computed using spectral responsivity (SR) as shown below.

$$EQE_{solar}(\lambda) = SR(\lambda)\frac{hc}{q} * \frac{1}{\lambda} \tag{17}$$

Where q is the elementary charge, c is the speed of the light and h is planck's constant.EQE takes in account all the photons including those not absorbed by the solar cell therefore EQE is corrected to find reflectance Internal Quantum Efficiency (IQE) of the solar cell. Jasco UV/VIS/NIR spectrophotometer was used to measure the absorption spectra of QD-900 and Photo Luminescence (PL) spectra were obtained using Jobin Yvon spectrometer. Values for refractive index (n) and extinction coefficients (k) for QD-900 were taken from the literature [8] and is shown in appendix C.2.

5.3 Hybrid QD/Si solar cell with PbS QDs

The photovoltaic devices studied in this section is an n^+pp^+ c-Si solar cell with Cr(100nm) and Al (500nm) as their front and rear contacts respectively. Fabrication of Si solar is described in section 5.2.1 and their schematic is as shown in figure 5.1(a). C-Si solar cell are hybridised using PbS QDs where peak emission is 900nm $\pm$ 10nm. All optical and electrical characterisation is carried before and after hybridisation of the sample to avoid disparity in the results.

5.3.1 Optical characterisation of Hybrid QD/Si solar cell

The colloidal QDs have stronger absorption in UV and can be used to harvest the high energy photon lost at surface of the Si solar cell. The absorbed photons are then transferred to silicon solar cell via luminescent down shifting (LDS) and RET. Figure 5.2 (a) shows the EQE of the device before (black) and after (red) hybridisation with QD-900. A relative enhancement in the EQE after hybridisation is as shown in figure 5.2(b). As predicted, there is a strong enhancement of EQE in UV region and decreases with increasing wavelength and this corresponds to absorption of QDs as shown in figure 5.2 (d). In contrary to author's expectations, the enhancement above absorption (dotted black line) of QDs can be seen. Figure 5.2 (c) shows the internal quantum efficiency (IQE) before and after hybridisation with QD-900. After hybridisation, enhancement in IQE can be seen for wavelength between 475nm-1000nm.The absorption of the device gives the information about the enhancement in EQE and IQE. The absorption of solar cell before (black solid line) and after hybridisation (red solid line) is shown in figure 5.2 (e) and their relative absorption (red solid line) is given in figure 5.2 (f).

Increase in absorption is observed between 910nm and 1100nm, to estimate their contribution to short circuit current(Jsc), it was weighted with AM1.5GM (ASTMG173) solar spectrum. A relative increase of 4.3% was observed and anti-reflection effect due to refractive index matching is a possibility for this enhancement. The relative absorption for non-absorbing QDs layer was modelled using RSOFT diffraction mode. The dashed blue line in Figure 5.2 (f) shows a good fit for non-absorbing spectral region of the QDs.

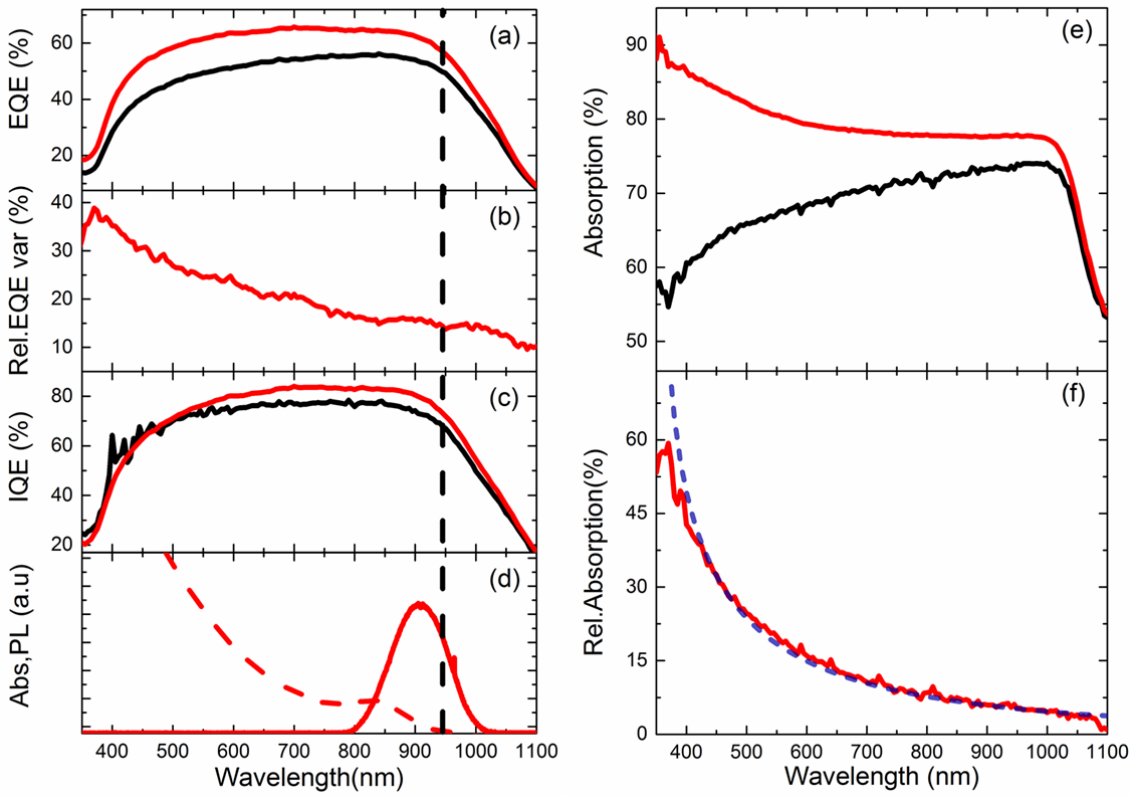

Figure 5.2: (a) The EQE of the device before (black solid line) and after (red solid line) hybridisation, (b) Relative enhancement in the EQE after hybridisation ,(c) shows the IQE of device before (black solid line) and after (red solid line) hybridization (d) shows the absorption and photoluminescence of QD-900 deposited on to the glass and dashed black line serves as a guide for separation below and above absorption of QDs. (e) shows the absorption of device before (black) and after (red) hybridisation. (f) Shows the experimental and modelled (blue dashed line) relative enhancement of absorption after hybridisation.

Using the relative increase in absorption of the solar cell, the EQE after anti reflection coating can be predicted. Using this approach, the EQE of hybrid QD/Si solar cell was calculated [9].

$$EQE_{cal}(\lambda) = EQE_{bare}(\lambda)(1 + \Delta A(\lambda)) \quad (18)$$

EQE_{bare} denotes the EQE before hybridisation and $\Delta A(\lambda)$ is a relative increase in absorption after hybridisation with QD-900.

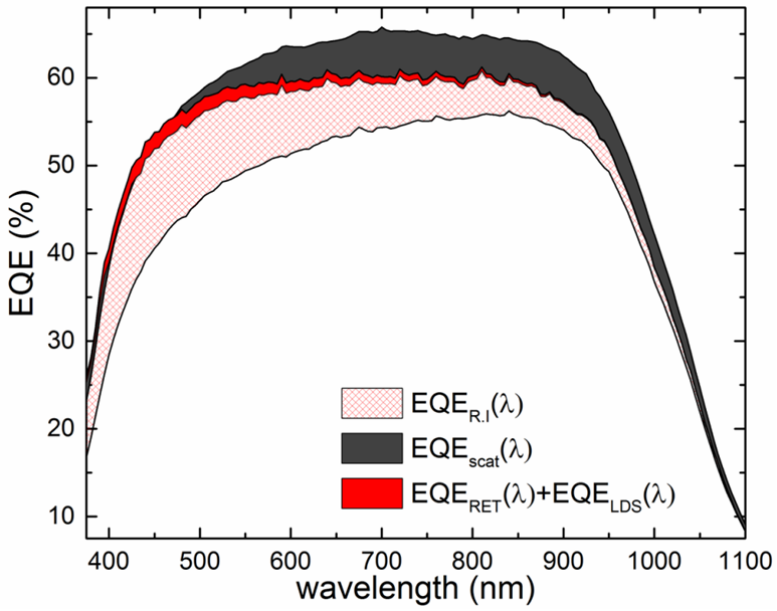

Figure 5.3: Shows EQE of hybrid device highlighting the enhancement due to different mechanisms.

The equation 19 does not take all the interaction mechanism between QD-900 and Si solar cell and this leads to discrepancy between calculated EQE ($EQE_{cal}(\lambda)$) and measured EQE. The EQE of hybrid QD/ Si ($EQE_{hybrid}(\lambda)$) can be modelled [9] with contributions from LDS, RET and refractive index matching as shown below:

$$EQE_{hybrid}(\lambda) = EQE_{R.I}(\lambda) + EQE_{LDS}(\lambda) + EQE_{RET}(\lambda) + EQE_{scat}(\lambda) \quad (19)$$

Where $EQE_{R.I}$, EQE_{LDS}, EQE_{RET} and EQE_{scat} are the EQE contribution due to refractive index matching (RI), luminescent down shifting (LDS), resonant energy transfer (RET) and scattering at QD aggregates respectively.

$$EQE_{R.I}(\lambda) = EQE_{cal}(\lambda) \times (1 - QD_{abs}(\lambda)) \quad (20)$$

$$EQE_{LDS}(\lambda) = IQE_{PL-QDS}(\lambda) \times A_{hybrid}(\lambda) \times QD_{abs}(\lambda) \times \left(1 - \eta_{RET}\right) \times QD_{yield} \quad (21)$$

$$EQE_{RET}(\lambda) = EQE_{cal}(\lambda) \times QD_{abs}(\lambda) \times (\eta_{RET}) \times QD_{yield} \quad (22)$$

QD_{abs} is the absorption of deposited QD layer and is calculated from refractive index and extinction coefficients [8] using Rsoft diffraction mode. IQE_{PL-QDS} is IQE of the device at peak emission wavelength of QDs. Figure 5.2(c) black curve corresponds to the IQE of the device before hybridisation along with emission of QDs(figure 5.2(d)). A_{hybrid} is an absorption of the device after hybridisation with QD-900. η_{RET} is the efficiency of RET from QDs to silicon, and is equal to 46% [7]. QD_{yield} is the quantum yield of QDs and is equal to ~30%. In this analysis, both η_{RET} and QD_{yield} are assumed to be independent of wavelength. Green dashed line in figure 5.3 represents the modelled EQE of the hybrid solar taking refractive index matching, LDS and RET into account. A good match between measured and modelled EQE can be observed between 375 and 450nm. The mismatch in modelled EQE above 450nm to 1100nm is due to scattering from the QD layers. The surface morphology of QDs can be observed from atomic force microscope (AFM) image shown in Fig 5.1 (a), it shows that the deposited QDs form aggregates between 0.45um and 10um. The deposited QD aggregate act as an efficient scattering centres, enhancing the EQE between 450nm and 1100nm. The contribution from refractive index matching, LDS, RET and scattering to photocurrent can be calculated by using equation below:

$$\Delta Jsc = \frac{\int \left[S_{hyb}(\lambda) - S_{Bare}(\lambda)\right] \Phi_{AM1.5G}(\lambda)}{\int S_{Bare}(\lambda)\, \Phi_{AM1.5G}(\lambda)} \tag{23}$$

where S_{hyb} and S_{Bare} is the spectral responsivity of hybrid and bare device. $\Phi_{AM1.5G}$ is the photon flux of AM1.5GM (ASTMG173) solar spectrum. The relative enhancement in short circuit density after hybridisation is given by ΔJsc where the integration limits are between 375 nm and 1100nm. Between 375nm and 1100nm, EQE contribution of R.I matching, LDS, RET and QD aggregates to ΔJsc are 8.73%, 0.77%, 1.47% and 9.28% respectively. Even though, there is a significant contribution from antireflection and scattering at QD aggregate, RET boosts the short circuit density by 1.47 % through efficient photon management. The contribution from LDS and RET can be increased further by using a near unity Quantum yield QDs.

5.3.2 Electrical characterisation of hybrid QD/Si solar cell

The current voltage (J-V) characteristics of device were investigated before and after hybridisation with QD-900. Figure 5.4 shows J-V curves under one sun illumination, where bare denotes the device before hybridisation. As expected, it can be observed from EQE measurements the enhancement in short circuit current (Jsc) from 20.65mA/cm^2 to 24.29mA/cm^2. The photon conversion efficiency increases from 6.74% to 8.11%, yielding a relative enhancement of 20.3%. The open circuit voltage (Voc) increases due to the scattering from QD aggregates [10], which will

lower the photon penetration depth and limit the bulk recombination. The fill factor reduces as Voc increase; this is due to reduction in shunt resistance. The series and shunt resistance are calculated from the slopes near Voc and Jsc respectively. Series resistance of solar cell is about 3.8ohm.cm^2 and remains the same before and after hybridisation but the shunt resistance reduces from 1239 ohm.cm^2 to 1199 ohm.cm^2. The relative percentage reduction in shunt reduction is about 3%. The shunt resistance reduction is due to the leakage along edges of the chip between the front and rear electrodes.

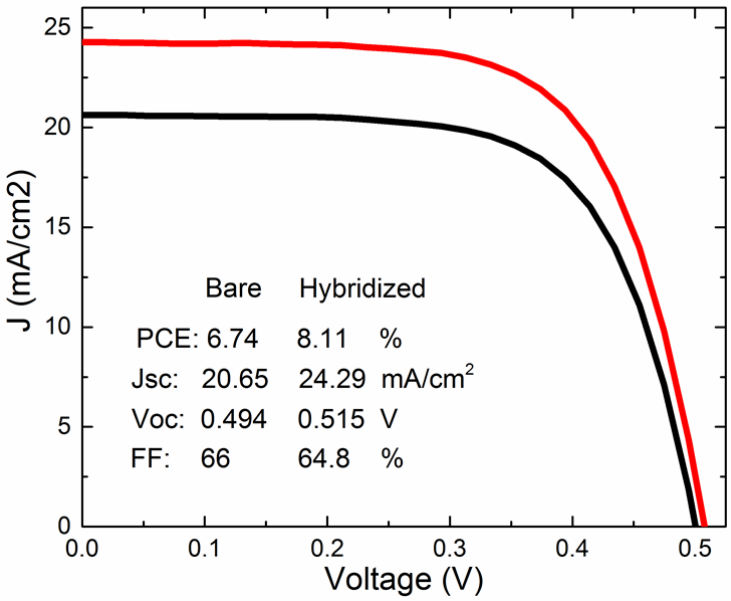

Figure 5.4: Shows J-V characteristics of before (black) and after (red) hybridisation.

5.4 Hybrid QD/Si solar cell with CdSxSe1-x/ZnS

The photovoltaic devices presented in this section are an n^+npp^+ c-Si solar cell where the front and rear contacts are made up of 500nm thick Al layer where the front contact fingers were deposited via e-beam evaporation after lithography pattern transfer.

C-Si solar cell are hybridised with CdS_xSe_{1-x}/ZnS (core/shell) colloidal semiconductor QDs with peak emission of 630±15nm for QD-630 where 1s absorption peak is at 620nm. All the optical and electrical characterisation are carried out before and after hybridisation of a sample to avoid any disparity in the results.

5.4.1 Optical characterisation of Hybrid QD/Si solar cell

CdSxSe1$_{-x}$/ZnS (QD-630) QDs are diluted in toluene solution which has the concentration of 17.5mg/ml. Using spin casting, QDs (QD-630) are deposited onto the surface of planar Si solar cell. Formed superficial QD (QD-630) layer acts as a strong absorber and absorbs the UV photons,

this extends up to wavelength of 650nm and is in the visible region of the spectrum. The electron-hole pairs are generated in QD and then transferred to underlie Si solar cell via LDS or RET. Figure 5.5(a) shows the absorption of planar solar cell before (black solid line) and after hybridisation (red solid line) with QD-630. The absorption of solar cell increases over the entire spectral operational region of the Si solar cell and their relative absorption increase is given in figure 5.5(b). The absorption enhancement is found to be stronger at 300nm (UV region) with 55 % and then it decays exponentially reaching 2% at 1100nm. The QD-630 does not absorb above 650nm, hence the refractive index matching might be responsible for enhancement between 650nm-1100nm.

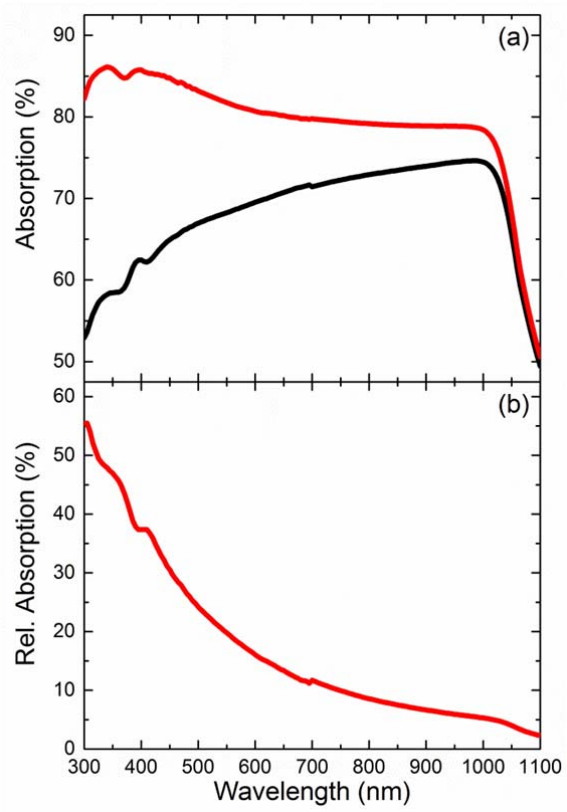

Figure 5.5: (a) Shows the absorption of planar solar cell before (black solid line) and after hybridisation (red solid line) with QD-630, (b) shows the relative absorption after hybridisation with QD-630.

The EQE of planar Si solar cell before (black) and after (red) hybridisation is shown in figure 5.6(a), broad band enhancement in EQE is observed. The EQE enhancement can be attributed to LDS, RET and R.I matching as observed in section 5.3. The enhancement above the band gap absorption of QDs is due to R.I matching and scattering. The relative enhancement of EQE after hybridisation is as shown in figure 5.6(b). The relative enhancement of EQE at 300nm is 70%, whereas relative absorption (figure 5.5(b) for same wavelength is 55%. Additional 15% enhancement is incurred at wavelength of 300nm by excitation for this hybrid QD/Si solar cell.

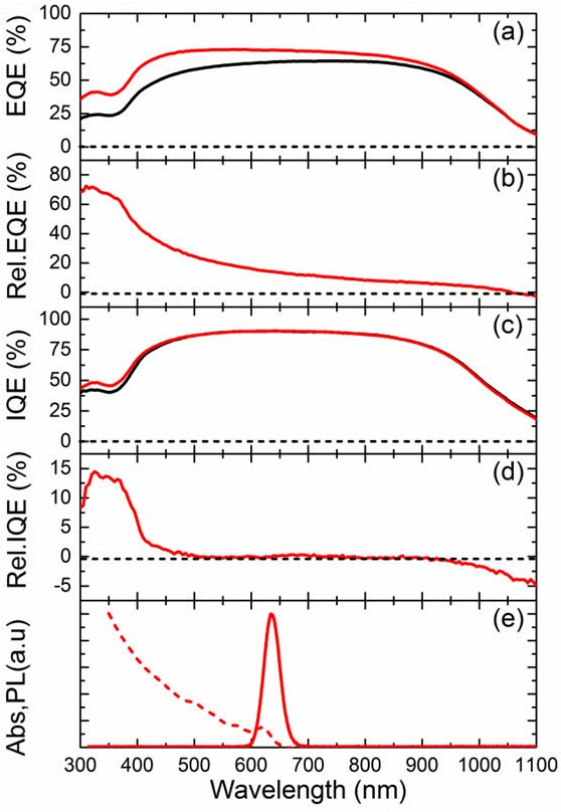

Figure 5.6: (a) The EQE of planar solar cell before (black solid line) and after (red solid line) hybridisation, (b) Relative enhancement in EQE after hybridisation and (c) shows the IQE of device before (black) and after (red) hybridisation, (d) Relative IQE after hybridisation with QD-630(e) Shows absorption and photoluminescence of QD-630 deposited on the glass (f) shows absorption of planar solar cell before (black solid line) and after hybridisation (red solid line), (g) shows relative absorption after hybridisation with QD-630.

The internal quantum efficiency (IQE) of solar cell is the efficiency of charge collection where only photons absorbed by solar cell are taken into the account. When IQE (figure 5.6 (c)) of the planar Si solar cell before (black) and after (red) hybridisation are compared, the effect of R.I can be excluded. IQE relative variation after hybridisation is as shown in figure 5.6(d). About 14% relative increase in IQE is observed between 310nm-370nm. Enhancement of the IQE drops to zero at wavelength of 500nm. The decrease below 310nm is the experimental discrepancies from integration of sphere and Si detector. Figure 5.6(e) shows the photoluminescence (solid red line) and absorption (dotted red line) of QD-630 deposited on the glass. The photoluminescence and absorption tells where QDs plays as an active or passive component in hybrid QD/Si solar cell.

In absorption regime of QDs, the QDs absorb photons and luminescent down shift or transfer electron-hole pairs to Si through non-radiative RET transfer. Photons above the band gap or coupled into Si either through refractive index matching or scattering at QD aggregate. For planar Si solar cell hybridised with CdSe/Zns, no aggregates were observed and is in accordance with author's IQE measurements.

Time resolved spectroscopy was used to study non-radiative resonant energy transfer (RET) from CdSe/ZnS QDs to underlie Si solar cell. Hybrid QD/Si was excited at 400nm using frequency-doubled Ti:Sapphire laser and photoluminescence of CdSe/ZnS at 630nm was then detected using avalanche photon diode and time-correlated single photon counting electronics. As a reference, the CdSe/ZnS was coated on a glass slide and TRPL study was performed. The decay dynamics of CdSe/ZnS QDs on glass (solid black line) and on Si solar(red solid line) is shown in figure 5.7. The QDs were excited with 1.6µW of power and the power was kept low to avoid causing any degradation due to local heating.

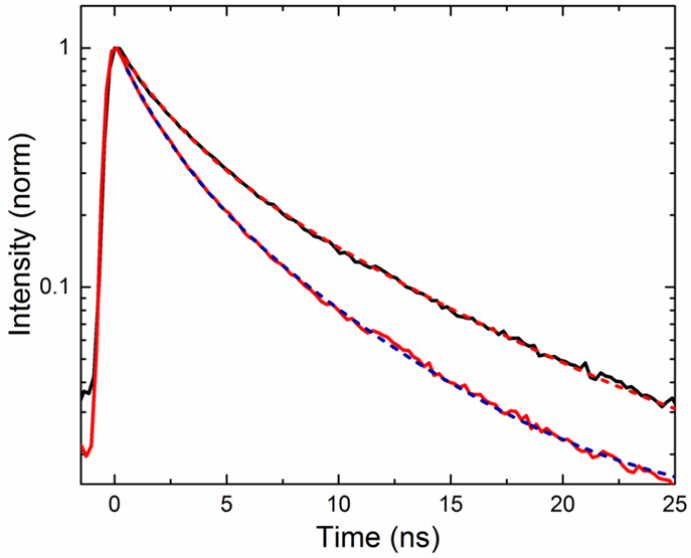

Figure 5.7: TRPL decays of QD-630 on a glass slide (black bold line) and planar Si solar cell (red bold line). The bi-exponential fit of QD-630 on glass and Si solar are shown as red dashed line and blue dashed line respectively.

The decay dynamics of QD-630 exhibits a bi-exponential decay and it is given by the relation [7] show below:

$$I(t) = A * e^{-k1*t} + Be^{-k2*t} + C \tag{24}$$

$$k = \frac{A * \tau_1 + B * \tau_2}{A * {\tau_1}^2 + B * {\tau_2}^2} \tag{25}$$

where k is an average decay rate with $\tau_1 = 1/k1$ and $\tau_2 = 1/k2$. The life time of excited electron is given by $\tau = 1/k$. The average decay rate of QD-630 on glass and Si are 0.15ns^{-1} and 0.23 ns^{-1} respectively. The efficiency of RET transfer can be calculate from the decay rates.

$$k_{hyb} = k_{RET} + K_{QD} \quad (26)$$

where k_{hyb} and k_{QD} are the decay rates of QDs on Si and glass respectively. k_{RET} corresponds to an additional accelerated decay rate due to the RET. The efficiency of RET ($\eta_{RET} = \frac{k_{RET}}{k_{RET}+k_{QD}}$) is calculated to be 32%.

5.4.2 Electrical characterisation of hybrid QD/Si solar cell

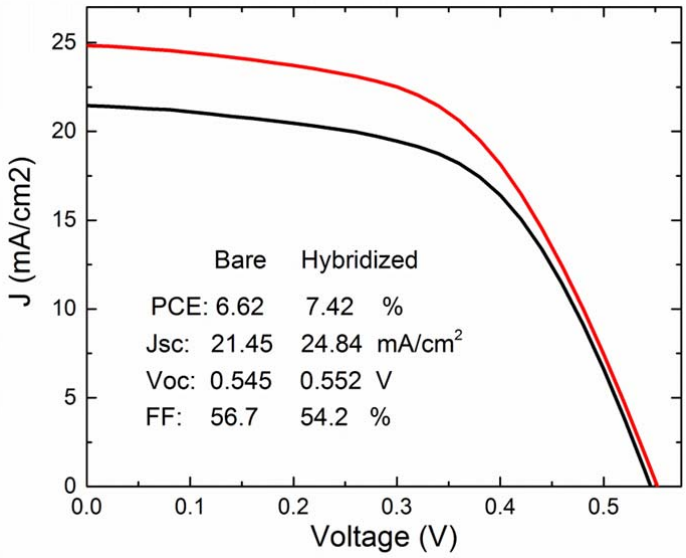

Figure 5.8: J-V of planar solar cell before (black solid line) and after (red solid line) hybridisation with QD-630

Figure 5.8 shows the J-V curves of planar Si solar with AM1.5G light bias. J-V curves are taken before (in black, fig 6.8) and after (in red, fig 6.8) hybridisation with QD-630. The solar cells were secured to PCB and wire bonded using Al. The QDs were spin casted on to the solar cell bonded on the PCB, to avoid any disparity resulting from contact. In figure 5.8, bare denotes the planar Si solar cell before hybridisation with QD-630. The Jsc (21.45mA/cm^2) of bare is lower than integrated Jsc (23.49 mA/cm^2) from EQE measurements. Jsc relative change of 9.5% from EQE and ABET solar simulator is the difference due to illumination area, illumination intensity, contact resistance and shading from contacts. The contact shadowing is ~2.5% of total cell area. After hybridisation with QD-630, Jsc increases from 21.45mA/cm^2 to 24.84mA/cm^2 and the relative enhancement of Jsc is 16%. The photon conversion efficiency increases from 6.62% to 7.42%,

yielding to a relative enhancement of 12.1%. The variation in Voc after hybridisation with QD-630 is about 1 %. The series and shunt resistance are estimated from the slope near the Voc and Jsc respectively. Series resistance is equal to ~7.3 ohm.cm^2 remains the same before and after hybridisation but shunt resistance increases by 9%. The increase in shunt resistance is due to passivation from organic ligands, passivating the QDs.

5.5 QD layer optimisation

Optical characteristics of planar Si solar cell were investigated as a function of spin speed for two different concentrations 17.5mg/ml and 60mg/ml. The spin speed of QD deposition was varied between 1500 rpm and 5000 rpm. All the samples studied in this section were hybridised with QD-630.

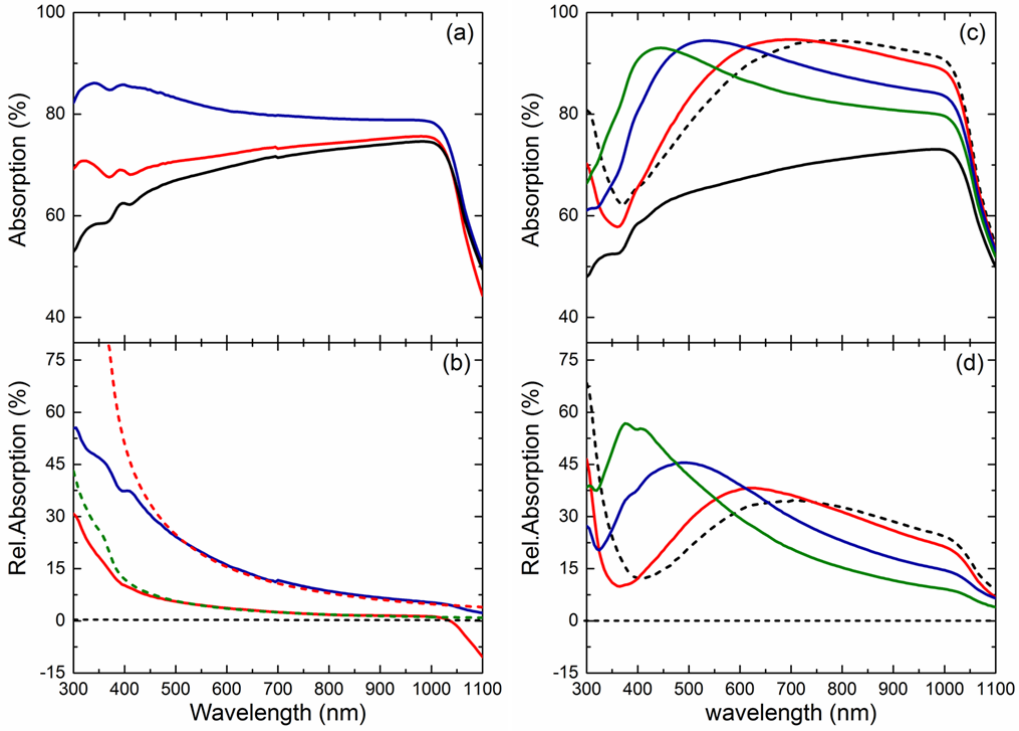

Figure 5.9: Absorption and relative absorption of planar Si solar cell hybridised with QD-630 at different spin speeds for concentrations 17.5mg/ml ((a) and (b)) and 60mg/ml((c) and (d)). a) Absorption of planar Si solar cell before (black solid line) and after hybridisation with spin speeds 1500 rpm (blue solid line) and 2500 rpm (red solid line). b) shows relative absorption of (a) where red dashed line (38nm QD layer) and green dashed line (18nm QD layer) are both modelled relative absorption, (c) absorption of planar Si solar cell before (black solid line) and after hybridisation with spin speeds 1500 rpm (black dashed line), 2000 rpm (red solid line), 3000 rpm (blue solid line) and 5000 rpm (green solid line).

The colloidal QDs (herein, QD-630) with concentration 17.5mg/ml were spun on top of the planar silicon solar cells (Figure 5.9 (a)) with spin speeds of 1500 rpm (blue solid line) and 2500 rpm (red solid line). The enhancement in absorption was observed for both spin speeds, with a significant increase near UV and gradual drop towards the band edge of the silicon. The relative increase in absorption after hybridisation is shown in figure 5.9(b). The QDs are strong absorbers near UV wavelength (300nm), with the relative increase of 55% and 31% for 1500rpm and 2500 rpm respectively. The QDs do not absorb above 630nm, which suggests that there might be contribution from R.I matching as observed in the case of planar Si solar cells hybridised with PbS QDs (section 5.3). Assuming QDs are non-absorbing layer, the relative absorption was modelled using Rsoft. The optical constants refractive index (n) and extinction co-efficient of QD-630 are determined from ellipsometer measurements and used for modelling. The optical constants plot for QD-630 is shown in appendix C.3. For 38nm (red dotted line) and 18nm (black dotted line) QD layer, a relatively good agreement between experimental and modelled was obtained between 500nm and 1050nm. Hence, QD-630 layer on Si can serve as a refractive index layer, increasing the coupling of light into the silicon.

Since the thickness dependent enhancement was observed for hybrid QD/Si solar cell at 17.5mg/ml. The concentration of QD-630 in toluene was increased to 60mg/ml to get thicker QD layer. Figure 5.9(c) shows the absorption of hybrid QD/Si solar cell as a function of spin speeds for the concentration of 60mg/ml. On hybridisation with QD-630 at 60mg/ml concentration, the absorption profile of hybrid QD/Si structure deviates from absorption of QDs. QDs has a strong absorption in UV and gradually drops to zero at the band edge as an optical behaviour. In this hybrid architecture, the peak absorption is in visible region of the spectrum (440nm) and shifts to near infra-red (775nm) for lower spin speeds. The relative increase in absorption after hybridisation with QDs (QD-630) at different spin speeds is shown in figure 5.9(d). To understand the optical behaviour of hybrid QD/Si solar, the relative absorption is modelled in RSoft diffract mod for a non-absorbing layer. The refractive index constant of QD layer was measured using ellipsometer and was used in the model. Figure 5.10 (a) shows the modelled relative absorption for QD layer where the thicknesses are as follows: 120nm as green solid line, 100nm as blue solid line, 90nm as red solid line, 80nm as black solid line, 70nm as black dotted line, 50nm as red dotted line, 35nm as blue dotted line and 15nm as green dotted line. For thin film of QDs (15nm and 35nm), the relative absorption has an exponential behaviour similar to the absorption behaviour of QD-630. As the thickness increases to 50nm, the relative absorption deviates from exponential behaviour exhibits in two regions. The relative absorption increases linearly up to 370nm and then drops exponentially at higher wavelengths. The two region of absorption is observed for 70nm QD layer on Si with plateau around 430nm. As the thickness of QDs increase further, three regions in the relative absorption is observed. As the thickness increases, maxima of absorption are shifted towards the infra-red region of the spectrum. For thin QD layer, maximum absorption is near the

UV region of the spectrum. The observed multiple regions in the absorption are from a 50nm QD layer due to the interference at QD/Si and QD/ air interfaces.

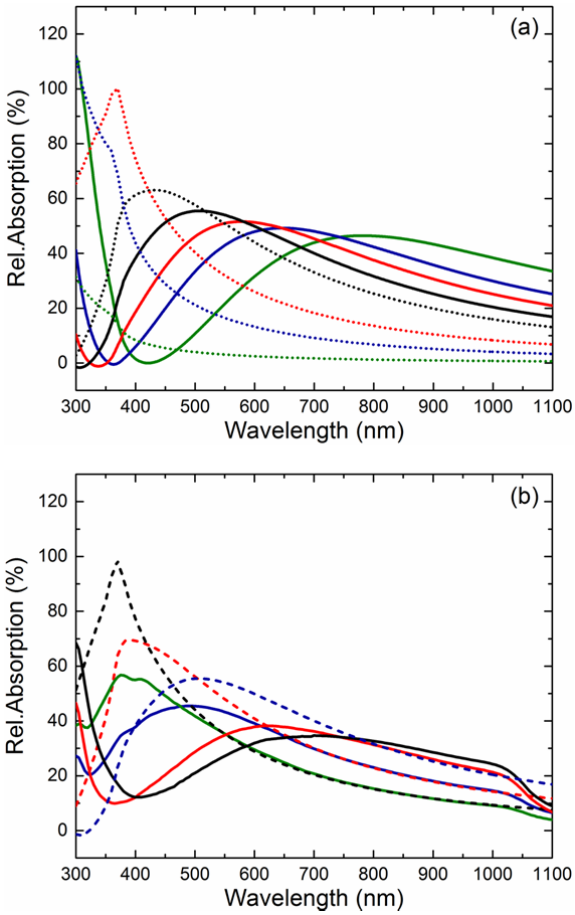

Figure 5.10: (a) Simulation of relative absorption of hybrid QD/Si structure for different QD layer thicknesses: 120nm (green solid line), 100nm (blue solid line), 90nm (red solid line), 80nm (black solid line), 70nm (black dotted line), 50 nm (red dotted line), 35nm (blue dotted line) and 15nm (green dotted line), (b) Experimental relative absorption for different spin speeds matched with the simulation results. The solid line corresponds to experimental relative absorption for different spin speeds 1500rpm (black solid line), 2000 rpm (red solid line), 3000 rpm (blue solid line) and 5000 rpm (green solid line). The dashed line correspond to simulated relative absorption for QD/Si hybrid structure with different QD layer thicknesses: 80nm (dashed blue line), 66nm (dashed red line) and 53nm (black dashed line).

The experimental relative absorption of hybrid QD/Si planar Si solar cell for different spin speeds between 1500rpm and 5000 rpm is shown in figure 5.10(b). The experimental relative absorptions are matched with modelled results. Above 630 nm where QDs does not absorb, a good match for 3000 rpm (blue solid line) and 5000 rpm (green solid line) was obtained with 66 nm (red dashed line, figure 5.10(b)) and 53nm (black dashed line, figure 5.10(b)) non-absorbing QD layer

respectively. For spin speeds below 2000 rpm, the model deviates from the experimental data. A 80nm QD layer, in figure 5.10(b) as blue dashed line, only gives a good match between 780nm and 1000nm for a spin speed of 2000rpm. The thicknesses of actual QD layer were measured using SEM and it corresponds to 100nm, 81nm, 62nm and 53nm for 1500rpm, 2000rpm, 3000rpm and 5000rpm respectively. The QD layer thickness versus spin speed plot for concentration 60mg/ml is shown in appendix C.4. The deviation between extracted model and SEM was found to be $\pm$ 5nm. Although, the model is not accurate for the entire spectral range, it still provides a good understanding of relationship between the thickness and absorption.

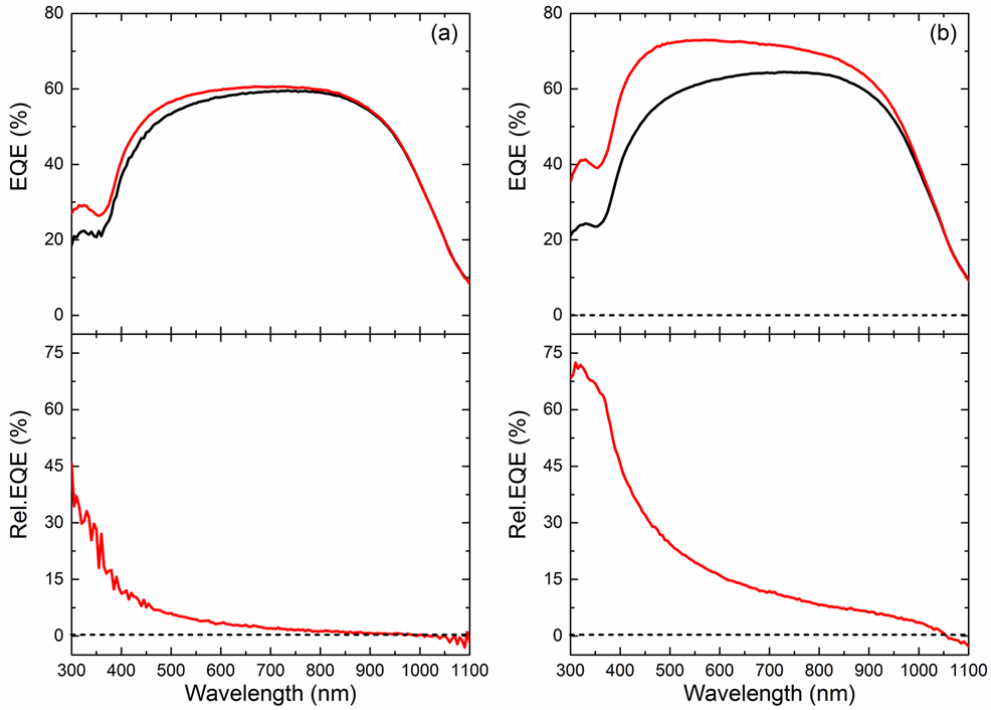

Figure 5.11: The EQE and relative EQE of planar Si solar cell hybridised with QD-630 with the concentration of 17.5mg/ml (a) The EQE before (black solid line) and after (red solid line) hybridisation at spin speed equal to 2500rpm. The relative increase in EQE after hybridisation is shown in bottom panel of the graph,(b) The EQE before (black solid line) and after (red solid line) hybridisation at the spin speed of 1500rpm with their relative EQE are given in the bottom panel. The QD layer thickness at spin speeds 2500rpm and 1500rpm for concentration 17.5mg/ml are 18nm and 38nm respectively.

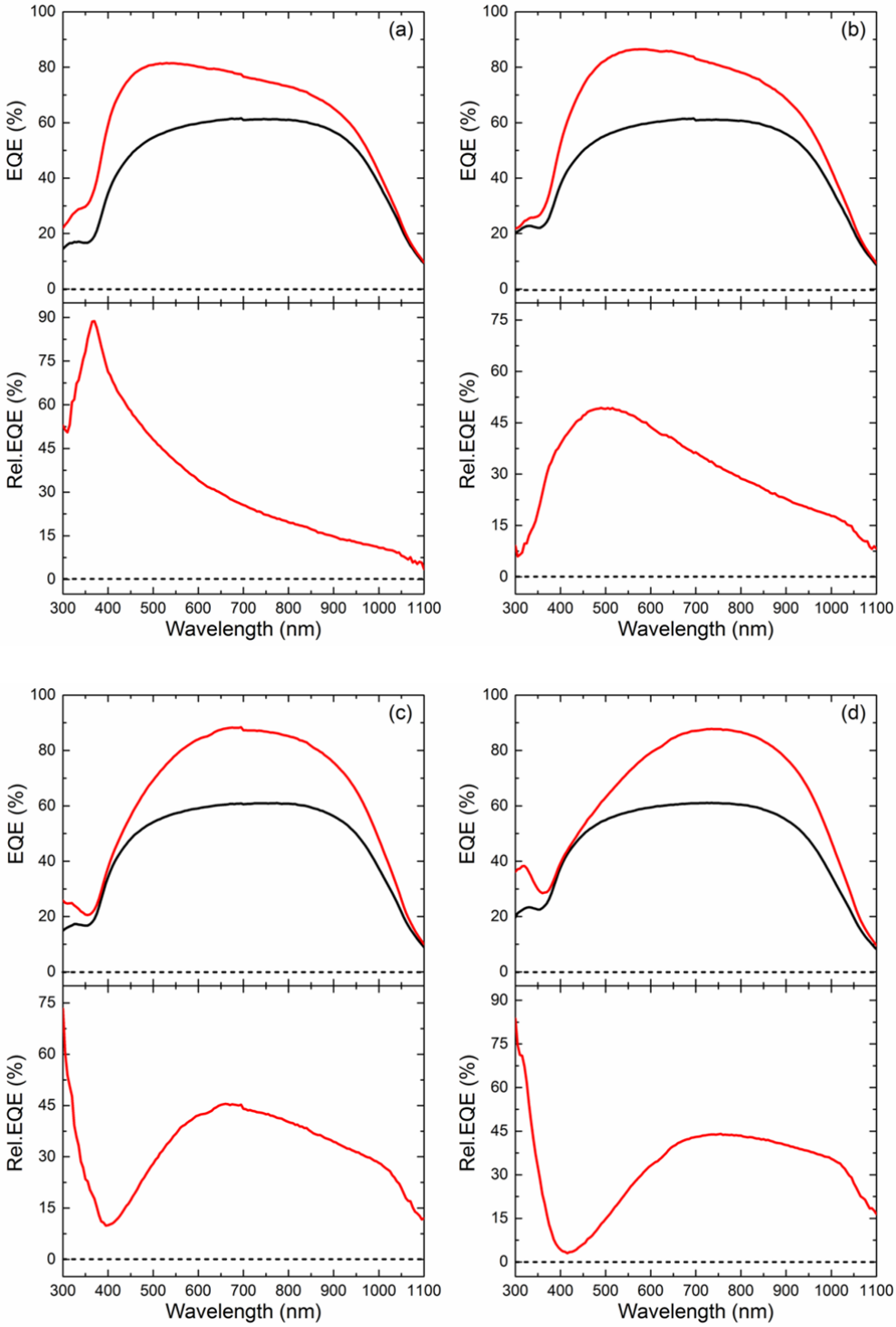

Figure 5.12: The EQE and relative EQE of the planar Si solar cell hybridised with QD-630 for the concentration of 60mg/ml (a)5000rpm,(b)3000rpm,(c)2000rpm and (d) 1500 rpm. The EQE of planar Si solar cells before and after hybridisation with QDs is presented as black and red solid line respectively. The relative increase in EQE after hybridisation is shown in bottom panel of corresponding graphs. The QD layer thickness at different spin speeds for concentration 60mg/ml are shown in appendix C.4.

The EQE dependence on spin speeds of QD deposition and concentration was investigated. The EQE of planar Si solar cell was measured before and after hybridisation with QDs. Figure 5.11 shows the EQE and relative EQE when hybridised with QD-630 which has a concentration of 17.5mg/ml for the spin speeds equal to 2500rpm and 1500 rpm. The QDs deposited at 2500 rpm showed substantial increase in EQE near UV, with relative enhancement of 46% at 300nm. The EQE enhancement decreases with the increase in wavelength reaching less than 3% above the absorption of QD-630. The EQE enhancement in UV is attributed to non-radiative RET and LDS, the photons absorbed at QDs site excite the electron-hole pairs. This then annihilate by emission of photon at 630±15nm or by electron-hole pair transfer to silicon through RET transfer. As QDs deposition speed is reduced from 2500rpm to 1500rpm, QD layer thickness increases from 18nm to 38nm; increasing the probability of RET and LDS below wavelength of 630nm. In comparison with planar silicon solar cell; relative enhancement of 68% at 300nm and 13.5% at 650nm was achieved with 1500rpm (Figure 5.11(b)). QD deposited with 1500rpm yielded an additional relative EQE of 22% and 11% at 300nm and 650nm respectively when compared with 2500rpm spun QD. For hybridisation with QD-630 having the concentration of 17.5mg/ml, shows slower spin speed (in this case, 1500 rpm) yielded higher EQE enhancement, not only in absorption region of QD-630 but also at longer wavelengths. Above the absorption, the enhancement can be attributed to R.I matching and scattering.

Hence, the thicker QD layer shows a drastic increase in EQE, to find the optimum QD layer thickness, the concentration was increased to 60mg/ml. Figure 5.12 shows the EQE before and after hybridisation, along with their relative EQE when the concentration is equal to 60mg/ml. The QD-630 is deposited with spin speeds equal to 5000rpm, 3000rpm, 2000rpm and 1500rpm. QDs deposited at 5000 rpm (figure 5.12(a)) shows a significant increase in EQE reaching a relative enhancement of 89% at wavelength of 370nm. Above the absorption of QDs (650nm onwards), the relative enhancement of EQE drops to 29.6 % which is still 16% higher than the best result for the concentration of 17.5mg/ml. When the QDs deposition speed is reduced to 3000 rpm, the increase in EQE throughout spectral range 300 nm -1100nm is observed. In comparison with 5000rpm, the QDs deposited at 3000 rpm leads to relatively low enhancement below 490nm and higher enhancement above 495 nm. For QD-630 deposited at slow spin speeds (1500 rpm and 2000 rpm) also shows an increase in EQE at measured wavelength spectrum (300nm-1100nm). The relative enhancement varies with respect to spin speeds, the observation can be summarised as follows: at highest speed (5000rpm), one can observe significant enhancement in the UV and the drop is exponential. Above 700nm, it can be observed that slower the spin speed, the relative enhancement of EQE increases (figure 5.13). Below 600nm, the relative enhancement of EQE increases with the increase in spin speed.

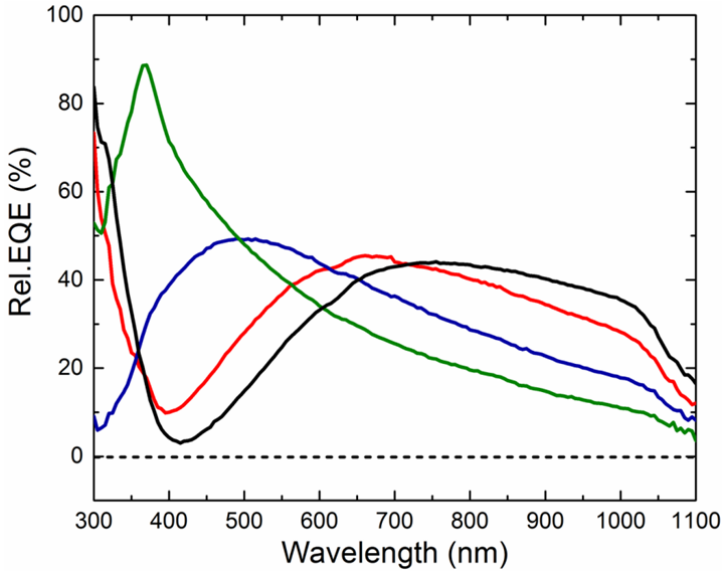

Figure 5.13: (a) Relative EQE of planar Si solar cell after hybridisation with QD-630 at spin speeds 5000 rpm(green), 3000 rpm(blue), 2000 rpm(red) and 1500 rpm(black) for concentration 60 mg/ml.

The short circuit current density (Jsc) of solar cells can be estimated from the EQE (or spectral responsitivity) and it is given by equation:

$$Jsc = \int S_{Bare\ or\ hyb}(\lambda)\Phi_{AM1.5G}(\lambda)\, d\lambda \tag{27}$$

where S_{Bare} and S_{hyb} denotes the spectral responsivity before and after hybridisation with QD-630. The spectral responsivity is weighted with $\Phi_{AM1.5G}(\lambda)$, and is the photon flux of AM1.5GM (ASTMG173) solar spectrum. Figure 5.14(a) shows the Jsc of planar Si solar cell after hybridisation with QD-630 for concentrations equal to 17.5mg/ml (blue solid circle) and 60mg/ml (red solid circle). The green dashed line at 22.5±0.625 mA/cm^2 represents the average Jsc before hybridisation. When QD-630 is deposited with 17.5mg/ml concentration, Jsc increases with reduced spin speed. For 2500 rpm, Jsc increases from 21.61mA/cm^2 to 22.27mA/cm^2, obtaining an increase of only 0.66mA/cm^2. As QD-630 deposition speed is reduced to 1500 rpm, Jsc increases by 3.72mA/cm^2 thus achieving 27.21mA/cm^2. The decrease in Jsc due to spin speed is clear from SEM, EQE and absorption measurements. The absorption decreases with QD thickness, reducing the probability of photon absorption, which in turn limits the number of photons involved in LDS and RETS transfer. Coupling of the light into silicon was also increased when QDs deposition speed was reduced from 2500rpm to 1500rpm. As the concentration was increased to 60mg/ml, slightly different trend was observed. The short circuit current density (Jsc) increases with the spin speed, as a result 29.52mA/cm^2 and 30.2mA/cm^2 for 1500rpm and 2000rpm respectively is achieved as Jsc. Above 3000rpm, the Jsc decreases and reaches 28.91mA/cm^2.

Although all the planar Si solar cells are processed at the same time, there still can be variation between samples, therefore relative Jsc enhancement is considered.Figure 5.14(b) shows the relative variations in Jsc after hybridisation. For concentration of 17.5mg/ml, the relative enhancement in Jsc increases from 3.1% to 13.7% when the spin speed is reduced from 2500rpm to 1500rpm. As the concentration was increased to 60mg/ml, Jsc increased further to 29.3mA/cm^2 for same spin speed of 1500rpm. Increasing the spin speed further to 2000rpm for concentration 60mg/ml was beneficial, achieving 36% relative enhancement in Jsc.

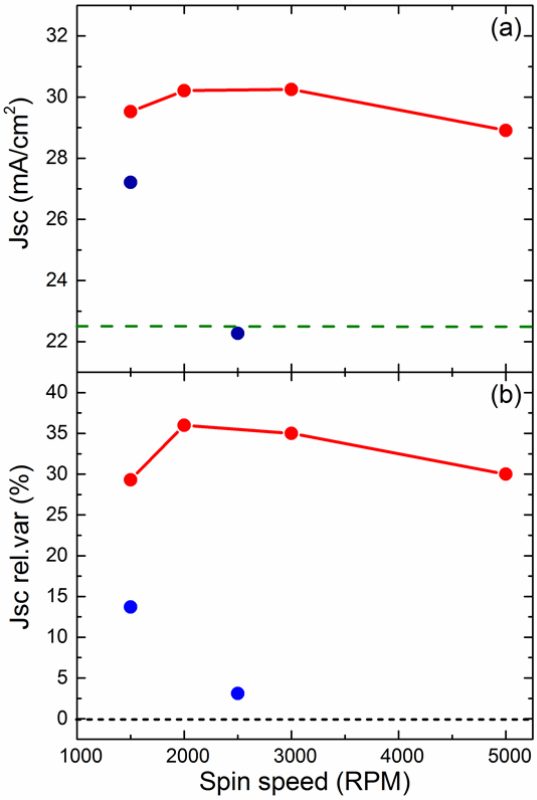

Figure 5.14: (a) Short circuit density (Jsc) after hybridisation with QD-630, (b) Relative variation in Jsc after hybridisation. The solid blue circle and solid red circle represent QD-630 hybridisation for concentrations of 17.5mg/ml and 60mg/ml respectively. The red solid line serves as guide line for the trend in Jsc and relative Jsc.

The deposition of QDs above 2000rpm saw a small drop by 1% to 35% at 3000rpm. At high speeds (in this case, 5000rpm), the relative enhancement Jsc decreased further by 5% reaching 30%. It is worth noting that QDs deposited at 60mg/ml has higher Jsc enhancement than QDs deposited at 17.5mg/ml. From this experimental work, it can be seen that hybridisation with QD-630 is beneficial, and boosts Jsc of the silicon solar cell.

5.6 Conclusion

In this work, it can be seen that by hybridising Si solar cells, the performance can significantly be enhanced. By using PbS QDs as a superficial layer of Si solar cells, the photon conversion efficiency can be enhanced by 20%. The large enhancement in PCE is due to refractive index matching and scattering as QD aggregates. The performance of device is boosted further by RET transfer of excitions from QDS to Si solar cell. The efficiency of LDS in this device was limited by PbS QDs with quantum yield equal to 30%. By using near unity quantum yield QDs, the efficiency of hybrid QD/Si cell can be increased further.

On hybridising with CdSxSe1-x/ZnS, a significant enhancement in near-UV was obtained through LDS and RET. The relative enhancement in PCE and Jsc was 12% and 16% respectively. The QD-630 deposition on planar Si solar cell was optimised for concentrations equal to 17.5mg/ml and 60mg/ml. The optical performance of hybrid QD-630/Si solar cell was investigated as function of spin speeds. The QD-630 was deposited between the spin speeds of 1500 rpm and 5000 rpm. For QD-630 deposited at 2000 rpm with concentration 60mg/ml, the Jsc was increased from 22.23mA/cm2 to 30.2mA/cm^2. On hybridisation with QD-630, our best device gave a Jsc enhancement of 36%, which is 18.4% higher than planar Si solar cell hybridised with PbS (QD-900) QDs.

References

1. J. Zhao, A. Wang, M. A. Green, F. Ferrazza, J. Zhao, A. Wang, and M. A. Green, "19.8% efficient “honeycomb” textured multicrystalline and 24.4% monocrystalline silicon solar cells," Appl. Phys. Lett. **73**, 1991–1993 (1998).

2. K. Masuko, M. Shigematsu, T. Hashiguchi, D. Fujishima, M. Kai, N. Yoshimura, T. Yamaguchi, Y. Ichihashi, T. Mishima, N. Matsubara, T. Yamanishi, T. Takahama, M. Taguchi, E. Maruyama, and S. Okamoto, "Achievement of More Than 25% Conversion Efficiency With Crystalline Silicon Heterojunction Solar Cell," IEEE J. Photovoltaics **4**, 1433–1435 (2014).

3. J. Oh, H. Yuan, and H. M. Branz, "An 18.2%-efficient black-silicon solar cell achieved through control of carrier recombination in nanostructures," Nat Nano **7**, 743–748 (2012).

4. H. Savin, P. Repo, G. von Gastrow, P. Ortega, E. Calle, M. Garín, and R. Alcubilla, "Black silicon solar cells with interdigitated back-contacts achieve 22.1% efficiency," Nat Nano **10**, 624–628 (2015).

5. S. Baek, J. Shim, and J. Park, "The energy-down-shift effect of Cd 0.5 Zn 0.5 S–ZnS core–shell quantum dots on power-conversion-efficiency enhancement in silicon solar cells," Phys. Chem. Chem. Phys. **16**, 18205–18210 (2014).

6. S. Kalytchuk, S. Gupta, O. Zhovtiuk, A. Vaneski, S. V Kershaw, H. Fu, Z. Fan, E. C. H. Kwok, C. Wang, W. Y. Teoh, and A. L. Rogach, "Semiconductor Nanocrystals as Luminescent Down-Shifting Layers To Enhance the E ffi ciency of Thin-Film CdTe / CdS and Crystalline Si Solar Cells," J. Phys. Chem. C **118**, 16393–16400 (2014).

7. P. Andreakou, M. Brossard, C. Li, P. G. Lagoudakis, M. Bernechea, and G. Konstantatos, "Spectroscopic evidence of resonance energy transfer mechanism from PbS QDs to bulk silicon," EPJ Web Conf. **54**, 1017 (2013).

8. B. T. Diroll, E. A. Gaulding, C. R. Kagan, and C. B. Murray, "Spectrally-Resolved Dielectric Functions of Solution-Cast Quantum Dot Thin Films," Chem. Mater. **27**, 6463–6469 (2015).

9. M. Brossard, C.-Y. Hong, M. Hung, P. Yu, M. D. B. Charlton, P. G. Savvidis, and P. G. Lagoudakis, "Novel Non-radiative Exciton Harvesting Scheme Yields a 15% Efficiency Improvement in High-Efficiency III-V Solar Cells," Adv. Opt. Mater. **3**, 263–269 (2015).

10. Y.-K. Liao, M. Brossard, D.-H. Hsieh, T.-N. Lin, M. D. B. Charlton, S.-J. Cheng, C.-H. Chen, J.-L. Shen, L.-T. Cheng, T.-P. Hsieh, F.-I. Lai, S.-Y. Kuo, H.-C. Kuo, P. G. Savvidis, and P. G. Lagoudakis, "Highly Efficient Flexible Hybrid Nanocrystal- Cu (In, Ga) Se2 (CIGS) Solar Cells," Adv. Energy Mater. **5**, 1401280 (2015).

Chapter 6: Photonic Quasi Crystals to enhance the performance of Hybrid QD/Silicon Cells

6.1 Introduction

12-fold photonic quasi crystal is used to enhance the performance of hybrid QD/Si solar cell. Photonic quasi crystals (PQC) are etched into the planar Si solar cell and colloidal QDs are deposited via spin coating. PQC serves as a nano template to bring QDs close to the metallurgical junction of solar cells. QDs on absorption of photons, transfers the percentage of generated electrons-hole pairs into the Si solar cells via resonant energy transfer (RET). As transferred electron-hole pairs are generated in close proximity of junction, the minority charge carriers transverse and are swept across the junction, increasing the performance of solar cells. A percentage of electron-hole pairs generated in QDs also undergoes a radiative recombination. In the case of radiative route, high energy photons are down shifted to lower energy photons through the band gap emission of QDs and it is coined as luminescent down shifting (LDS). LDS photons can be absorbed by underlie of silicon, enhancing the performance of Si solar cells. From previous chapter, it can be observed that QD can acts as a refractive index matching layer, enhancing the performance of the solar cell. Therefore, QDs within the PQC can also alter coupling of the light into Si solar cell.

In this chapter, 12-fold photonic quasi crystal (PQC) with lattice pitch of 700nm and hole diameter of 350nm is patterned on to the planar Si solar cell. PQC acts as nano template to bring QDs close to the metallurgical junction of silicon solar cell. CdSe/ZnS QDs with emission peak at 630±15nm is deposited on the surface and within holes. QDs act as efficient light absorbers and transfers the absorbed photons to Si solar cell through radiate and non-radiative RET transfer. QDs deposited on PQC solar cell can alter the coupling of light into silicon contributing to enhancement of Jsc short circuit current. Optimisation of QD layer was performed through dispersing at different spin speeds. The coupling of light into solar cell was enhanced through increasing the air fill fraction of PQC. In the final section, the best hybrid PQC solar cell discussed in this chapter is compared with best hybrid planar device from chapter 5.

6.2 Fabrication of PQC solar cell

Monocrystalline Silicon (c-Si) solar cells were produced by Q CELLS in Germany. It is n^+pp^+ c-Si solar cell without contacts and antireflective coating. n^+ emitter was sputtered with 100nm thick silicon dioxide (SiO_2) where SiO_2 layer was employed as a hard mask for etching Si using Chlorine (Cl_2)/Argon (Ar) plasma. E-beam lithography and reactive ion plasma etching (RIE) were used to transfer 12 fold symmetric quasi crystals (PQC) on to the SiO_2 layer. SiO_2 layer was spin coated with a 400nm ZEP-520A layer (e-beam resist). E-beam resist was then pre-baked at 180°C for 3 minutes. After cooling, conductive polymer ESpacer was spin casted to avoid charge buildup during e-beam exposure. This was then exposed with 190μC/cm^2 exposure dose, followed by rinse of Espacer with DI water then e-beam resist was developed using ZEDN-50. SiO_2 nanoholes were formed by two steps RIE process using CHF_3/Ar to etch and nitrogen (N_2) as coolant gas in a loop etches. Silicon (Si) was etched in an inductively coupled plasma reactive ion etching (ICP-RIE) using Cl_2 and Ar (Cl_2/Ar = 50/12.5 sccm) process gases with bias power of 200W and ICP power of 1000W.Using lithography, metallization and lift-off processes, a 500nm thick Al fingers were deposited as front contacts. For rear contact of solar cells, 500nm thick aluminum was evaporated using E-beam. Final diced devices were micro bonded to printed circuit board for characterisation. The active device area is equal to 36mm^2 and e-beam patterned PQC is equal to ~ 9mm^2. Herein, the patterned solar cells are referred as PQC solar cells. CdSxSe1-x/ZnS (core/shell) QDS with peak emission at 630±15 nm (QD-630) were used to hybridise PQC solar cell. These are 5.5-6.5nm QDs capped with oleic acid. QD630 colloidal QDs used were dispersed in toluene with concentration of 60mg/ml. The QD-630 was chosen in this experimentation to compensate for detrimental effects due to ICP etching of PQC solar cell. Dynamic spin coating was used to hybridise the PQC solar cells. Figure 6.1 (a) shows the schematic of PQC solar cell. The top view of PQC solar cell before and after hybridisation is shown in fig 6.1(b) and (c) respectively. The inset in figure 6.1(c) shows the 100 times magnified SEM image, where individual QDs are visible.

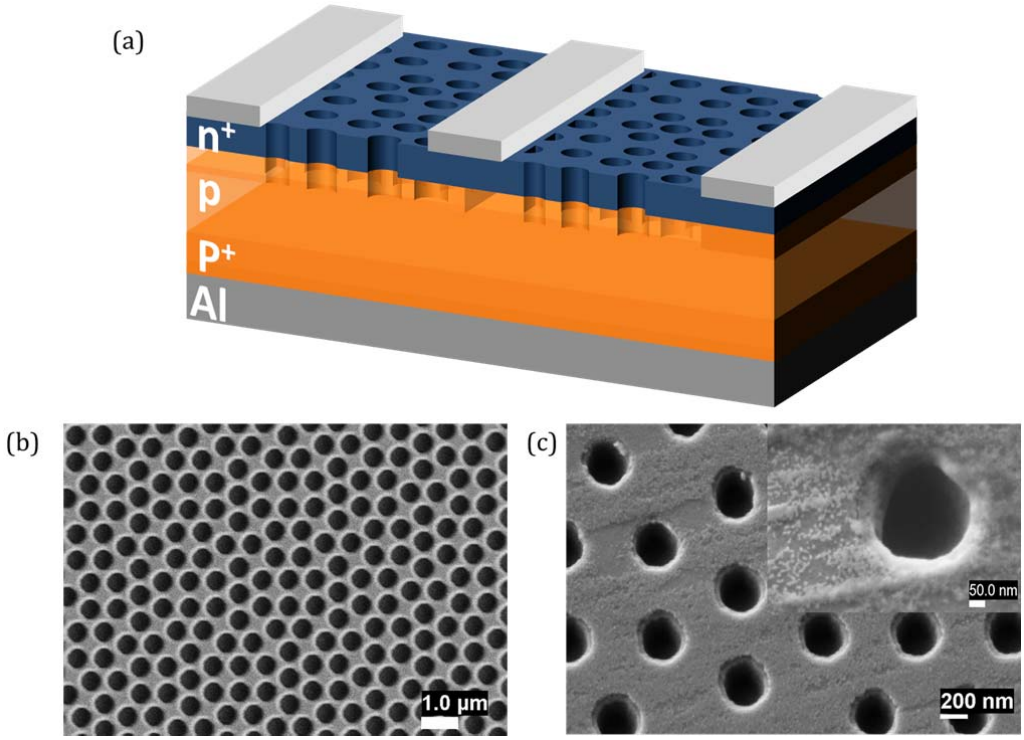

Figure 6.1: (a) Schematic representation of PQC solar cell, (b) and (c) top view SEM image of PQC solar cell before and after hybridisation with CdSe/ZnS QDs. Inset in figure (c) shows the QDs

6.3 Device Characterisation

The PQC solar cell devices studied are made up of n^+pp^+ structure with a 500nm Al layer used as front and rear contacts. Reference device without PQC (planar in this case) are metallized with same contacts for comparative studies. Planar and PQC solar cell are hybridised with QD-630. All the optical and electrical characterisation is done prior and after hybridisation to avoid disparity in the results of different samples.

6.3.1 Optical characterisation

Using the appropriate colloidal QDs, short circuit current density of planar Si solar cell can be enhanced by LDS, RET and R.I matching (refer chapter 5). Figure 6.2 shows the schematic and simple band diagram of different electron-hole generation schemes in hybrid Si solar cells. The aim is to bring the QDs close to the junction of solar cell. In this chapter we use PQC to bring QDs close to depletion region. On photon absorption, electron-hole pairs created in QDs are transferred to the silicon through RET mechanism. In this case, electron-hole pairs are transferred to close proximity of metallurgical junction; strong electric field separates the minority charges and they are

then collected at emitter (n-type) and base (p-type). For defect-free depletion region the charge collection probability is close to unity.

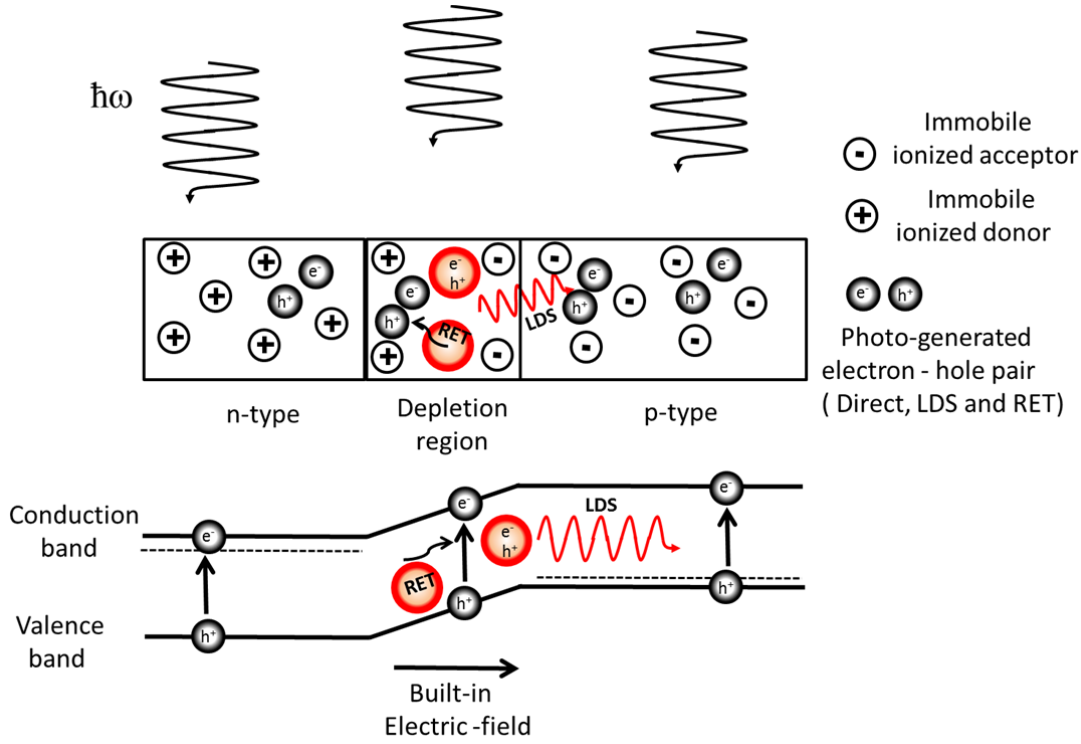

Figure 6.2: Shows the schematic and simple band diagram of p-n junction under illumination with photon-generated electron- hole pair in hybrid Si solar cells. Where LDS and RET denote luminescent downshifting process and resonant energy transfer mechanism.

The author used photonic quasi crystal to bring QDs close to the junction of solar cell. 12-fold quasi crystal has a lattice pitch of 700nm and nanholes diameter of 350nm. The nanoholes have a depth of 300nm, and they are ~100nm away from metallurgical junction (Refer Appendix C.1). QD-630 with concentration of 60mg/ml is dispersed on to the PQC solar cell as a function of spin speeds. Figure 6.3 shows the cross-sectional SEM image of hybridised PQC solar at spin speeds 3000rpm (Figure 6.3(a)), 2000rpm (Figure 6.3(b)) and 1500 rpm (Figure 6.3(c)). When QD-630 spin speed is reduced, QDs starts filling the nanoholes. QDs fill at spin speed 3000rpm, 2000rpm and 1500 rpm are 142nm, 203nm and 254nm respectively. The QDs also get deposited surface of PQC solar cell and the QD layer thickness at 3000rpm, 2000rpm and 5000rpm are 30nm, 56nm and 88nm respectively. It can be noted that the slower the spin speed is, the thicker the spin coated QD layer will be.

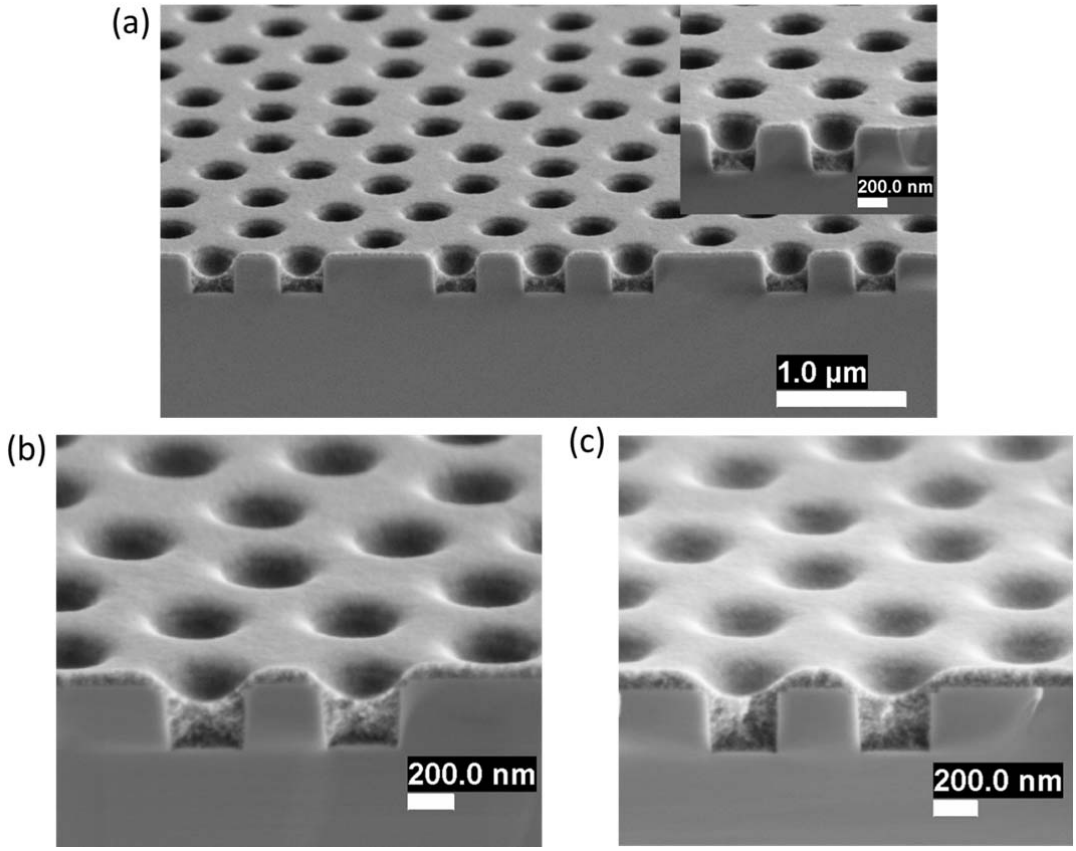

Figure 6.3: Cross-sectional SEM image of PQC solar cell hybridised with QD-630 at different spin speeds: a) 3000rpm and inset is higher magnification of (a), b) 2000rpm and c) 1500rpm.

All the PQC solar samples are measured before and after hybridisation to avoid variability between different samples. Figure 6.4 (a), (b) and (c) show EQEs of hybrid PQC (red solid line) for different QD deposition speeds along with their EQEs before (black solid line) hybridisation. After hybridisation with QD-630 at spin speed 3000rpm, significant enhancement near UV with relative enhancement of 104% at 300nm can be seen. Relative increase in EQE drops with the increase in wavelength reaching zero at 650nm. After 650nm, QDs do not absorb. For the wavelengths between 655nm and 775nm, hybridisation with QD-630 is detrimental as coupling of the light via PQC is reduced. Above 755nm, hybridisation is beneficial with EQE enhancement. As the spin speed is reduced to 2000rpm and 1500 rpm, the EQE enhancement below 400nm is reduced. Nevertheless, enhancement was still observed in the visible and near infra-red regions of the spectrum.

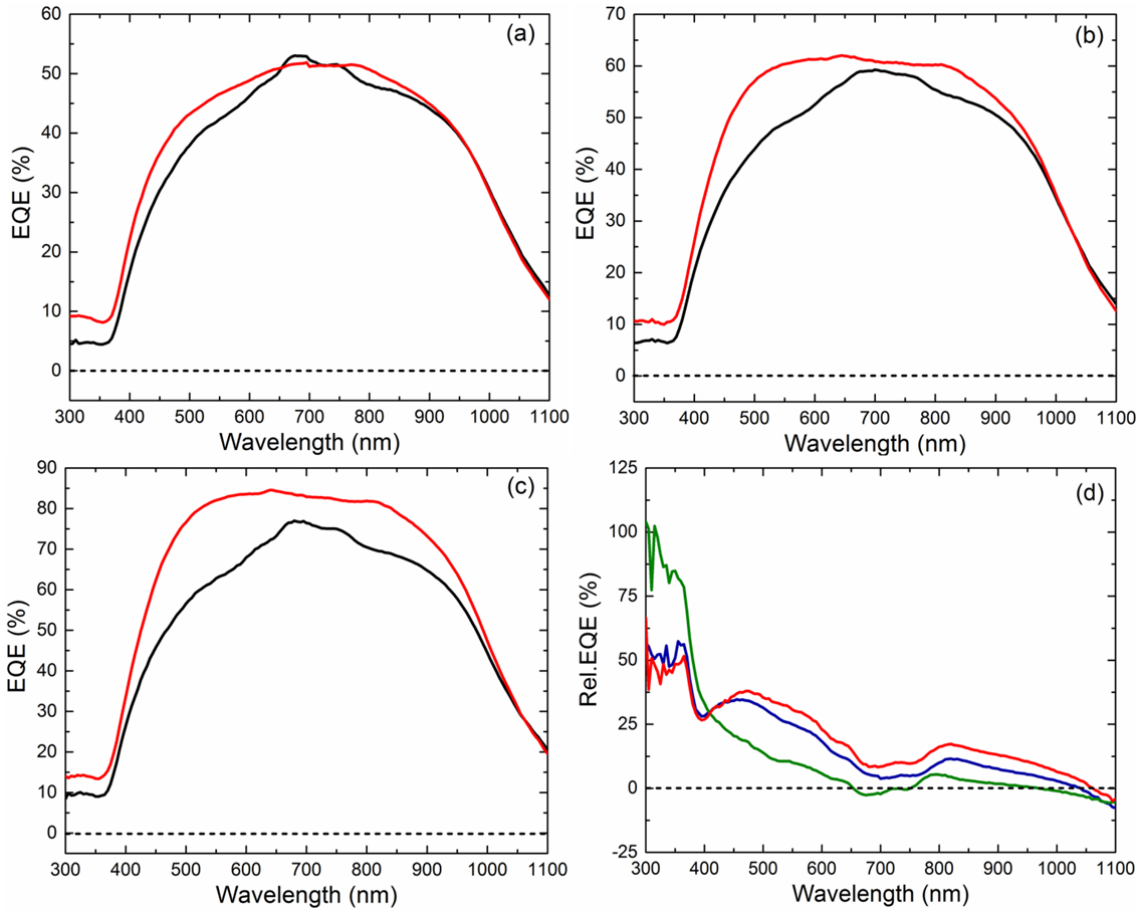

Figure 6.4: The EQE of hybrid PQC (red solid line) is measured as a function of spin speeds (a) 3000rpm, (b) 2000 rpm and (c) 1500rpm. The black solid line represents the reference EQE of corresponding PQC solar cell before hybridisation. (c) Shows the relative EQE after hybridisation for spin speeds of 3000rpm (green solid line), 2000rpm (red solid line) and 1500rpm (blue solid line).

Near UV spectral region, the EQE enhancement diminished with reduced spin speed refer to Figure 6.4(d), which shows the relative variation of EQE. Correlation can be observed between relative EQE measurements and QD layer thicknesses. Figure 6.3 shows the cross-sectional SEM image of nanoholes cavities filled with QD. The QD layer thickness is proportional to absorption and re-emission losses and QD-QD RET transfer also increases for closely packed QDs. These losses can be circumvented with near-unity quantum yield QDs. In this study, 12-fold quasi crystal with lattice pitch of 700nm and hole diameter of 350nm was used. Before hybridisation, maximum EQE is observed at 700 nm as the effect of the pitch. On hybridisation, coupling at 700nm and at 350nm are reduced, leading to two dips (~ 390nm and 700nm) in relative EQE.

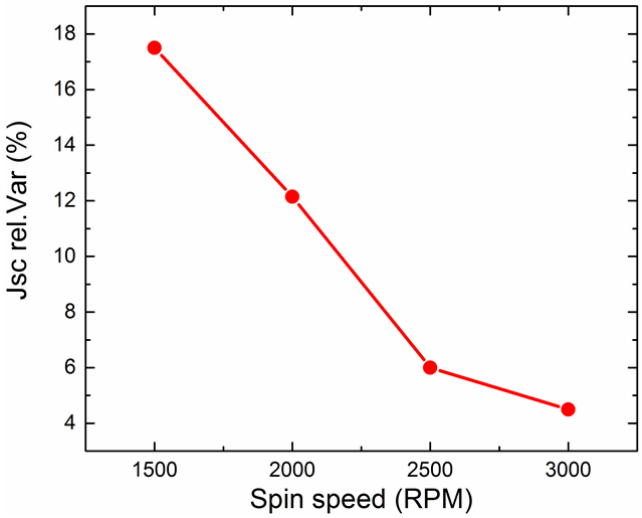

Figure 6.5: Relative variations of short-circuit current (Jsc) for QD-630 depositions at different spin speeds.

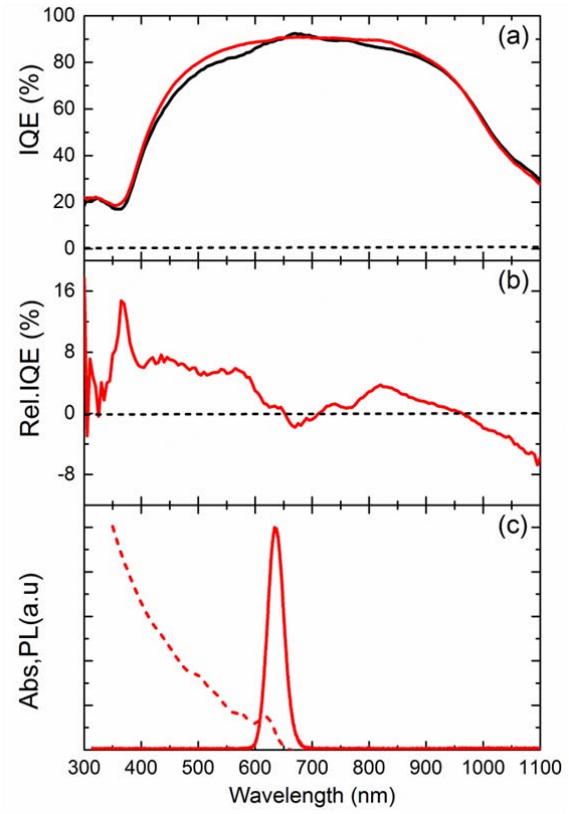

Figure 6.6: (a) The IQE of PQC solar cell before (red solid line) and after (black solid line) hybridisation with QD-630 at spin speed 1500rpm, (b) Relative variation of the IQE after hybridisation, (c) The absorption and photoluminescence of QD-630 on glass.

From EQE measurements, Jsc can be estimated. The relative variation in Jsc can be estimated from the equation 23. Maximum Jsc enhancement of 17.5% was observed at 1500rpm (Figure 6.5), as the spin increases Jsc enhancement drops linearly until it reaches 4.5% at 3000rpm. The calculated Jsc for the PQC solar cell before and after hybridisation with QD-630 at 1500rpm is 25.5 mA/cm^2 and 30mA/cm^2 respectively.

Enhancement in Jsc can be attributed to the refractive index matching, LDS and RET. The enhancement due to the index matching is directly proportional to the increase in absorption after hybridisation. Internal quantum efficiency (IQE) is given by the ratio of EQE and absorption, where the first order approximation of IQE (hybrid device) only contains information about LDS and RET. Internal quantum efficiency (IQE) of best PQC solar cell before and after hybridisation is presented in Figure 6.6(a). The PQC solar cell is hybridised with QD-630 at spin speed of 1500 rpm. The relative variation in IQE after hybridisation is given in Figure 6.6(b). Figure 6.6(c) shows the absorption (red dashed line) and photo luminescence (red solid line) of QD-630. IQE of hybrid PQC solar cell shows enhancement in the absorption region of QDs. At 365nm, the maximum relative enhancement of 15% was obtained. IQE enhancement then gradually decreases reaching 7%-5.5% between 415nm and 575nm. Above the absorption region of QDs (650nm), IQE enhancement reaches zero. The hybridisation of PQC with QD-630 is beneficial in absorption region of QDs, IQE enhancement is attributed to LDS and RET of electron-hole pairs. Below 360nm, IQE enhancement drops and this is due to absorption and re-emission losses in thick QD layer. IQE enhancement has also been observed for wavelengths between 715nm and 960nm, where the QDs do not absorb. For shallow p-n junction, change in the effective penetration depth can boost the IQE of the solar cell. This phenomenon can be attributed to IQE enhancement between 715nm and 960nm. Hybridisation with QD-630 was found to be detrimental above 960nm.

6.3.2 Time resolved photo luminescence

Efficiency of RET from QD-630 to silicon can be estimated from time resolved photoluminescence (TRPL) measurements (chapter 5). QD-630 was excited at 400nm using a frequency- doubled Ti:Sapphire laser. QDs on glass and PQC solar cell were excited with power of 1μW. The PL was detected using APD and time-correlated single photon counting electronics. Figure 6.7 shows the decay of QD-630 on glass slide and PQC solar cell. The decay dynamics of QDs is accelerated for QD-630 on PQC silicon solar cell.

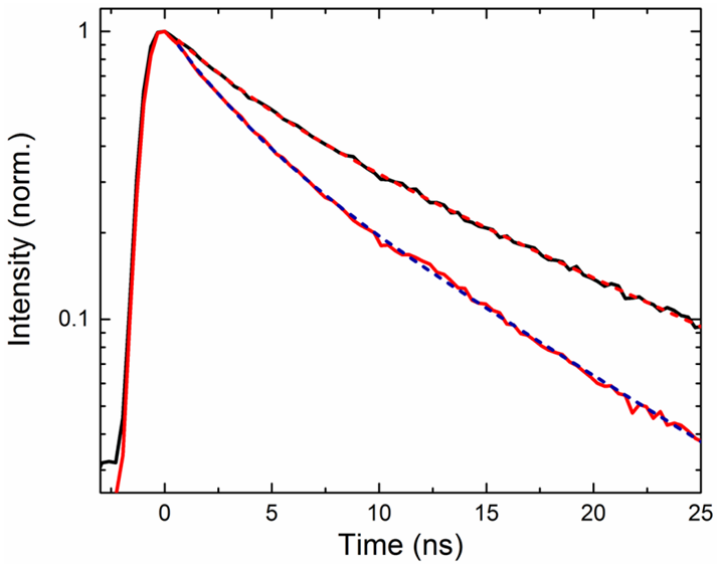

Figure 6.7: Decay dynamics of QD-630 hybridised on glass (black solid line) and PQC (red solid line) solar cell. The fit for decay of QDs on glass and PQC solar cell are shown as dashed redline and dashed blue line respectively.

The decay of the QD are fitted with bi-exponential decay (equation 24), the decay rate of QDs on the glass and PQC solar are $0.085(ns)^{-1}$ and $0.123(ns)^{-1}$ respectively. From the decay rates, the calculated RET efficiency is 31%.

6.4 PQC solar cell versus planar solar cell

PQC solar cell hybridised with QD-630 at spin speed of 1500rpm (Figure 6.3 (c)) achieved the Jsc of $30mA/cm^2$. The Jsc is estimated from the EQE, the red solid line in Figure 6.4 (c). The EQE is converted to spectral responsivity and then Jsc is calculated from equation 27.For optimised QD deposition planar device also yielded a short circuit of $30.2mA/cm^2$ (section 5.5). To improve hybrid PQC, the EQE of the PQC and planar Si solar cells before and after hybridisation were considered.

Figure 6.8(a) shows that the EQE of PQC (red solid line) solar cell is better than of a planar solar (black solid line) cell above 480nm. PQC solar cell has peak EQE of 77% at 680nm and 76.4% at 700nm. The maximum EQE at 700nm corresponds to pitch of photonic quasi crystal. Above 700nm, there is a gradual drop in EQE of PQC but it is still better than the EQE of the planar solar cell. Relative increase in EQE of PQC is shown in figure 6.8(b). Maximum enhancement of EQE when patterned with PQC (in this case, 700nm pitch and 350nm hole diameter) is at the band edge of the silicon. The second maximum enhancement is at the pitch of PQC. Below 480nm, the EQE of the PQC solar cell was found to have poor performance in comparison with planar Si solar cell.

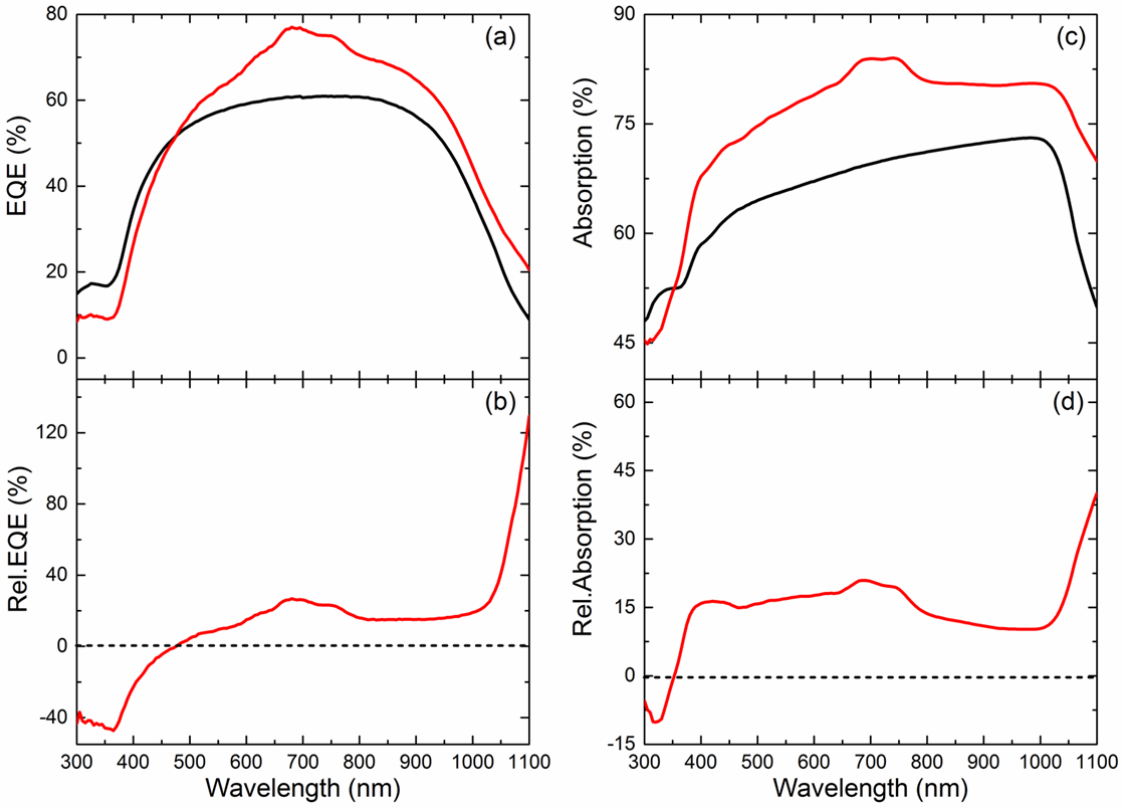

Figure 6.8: (a) EQE of the planar (black solid line) and PQC (red solid line) solar cell. (b) Relative variation of PQC solar cell with respect to planar Si solar cell (c) Absorption of planar (black solid line) and PQC (red solid line) solar cell (d) Relative absorption of PQC solar cell.

To analyse the detrimental effect of PQC below 480nm, the absorption of the PQC and planar solar cell were compared and it is shown in figure 6.8(c). From 355nm onwards, the absorption is significantly enhanced when patterned with PQC, where the maximum absorption is at the pitch of PQC. The relative absorption after patterning with PQC is shown in figure 6.8 (d). About 15%-20% enhancement is observed between 390nm- 740nm and above 750nm, the relative absorption drops gradually from 19 % at 750nm to 10.2% at 980nm. At 985nm, the absorption gradually increases from 10.3% until the maximum relative absorption of 40% at 1100nm is reached. Assuming the PQC layer on solar cell is an refractive index-matching layer, it is possible to estimate the EQE of PQC solar cell from the EQE of planar Si solar cell and relative variation in absorption after patterning it with PQC (refer to equation below).

$$EQE_{PQC} = EQE_{planar}(A_{rel} + 1) \quad (28)$$

Where EQE_{PQC} is the estimated EQE of PQC solar cell and EQE_{planar} is the EQE of planar Si solar cell. A_{rel} is the relative variation in absorption after patterning with PQC.

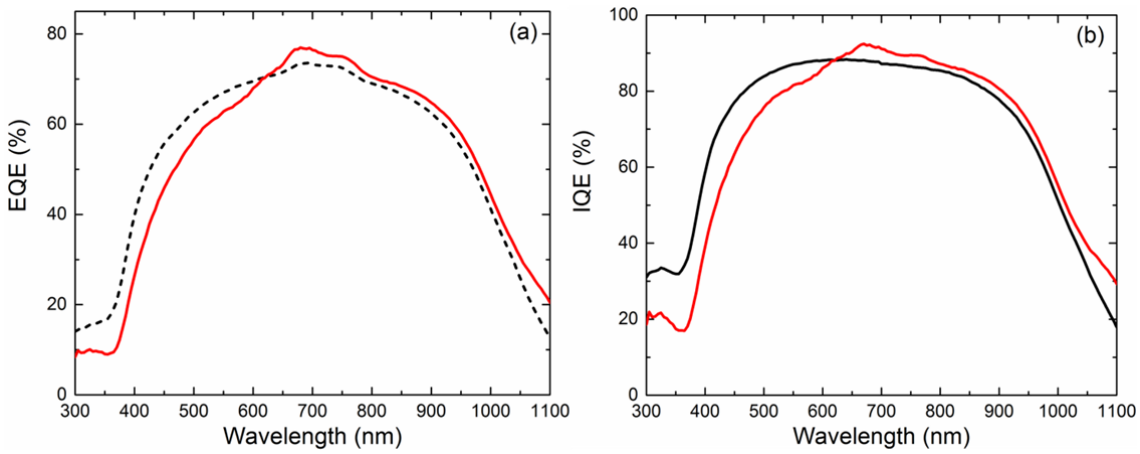

Figure 6.9: (a) Shows the measured (red solid line) and estimated (black dashed line) EQE of PQC solar cell. (b) IQE of planar (black sold line) and PQC (red solid line) solar cell.

From figure 6.9 (a), it can be seen that EQE_{PQC} is much higher than the actual measured EQE of PQC solar cell for wavelengths below 620nm. At 365nm, the measured EQE drops relatively by 50% and above 365nm, it gradually improves. The loss of EQE at near UV and visible regions suggests that generated electron-hole pairs are not extracted efficiently. Inductive coupled plasma etching of Si generates a lot of surface traps on the surface of etched sidewalls and the surface traps act as a recombination centre. If the surface traps are reduced, the Jsc of PQC solar cell can be enhanced. To compensate for etch loss; few nm of passivation layer like Al2O3 can be grown using atomic layer deposition. This processing step was not performed in devices presented in this chapter but have shown to reduce surface states of PQC solar cell. Another interesting observation is that above 625nm, the measured EQE of the PQC is higher than EQE_{PQC}. This effect can be attributed to change in effective penetration depth and increased collection between 625nm and 1100nm. From EQE_{PQC} , it can be seen that quality and the effective Jsc of PQC solar cell can be improved.

Internal quantum efficiency (IQE) is the number of charge carrier collected to the number of photons absorbed and this can give information about the percentage of photons, which undergo recombination before collection at the electrodes. Figure 6.9(b) shows the IQE of planar (black solid line) and PQC (red solid line) silicon solar cell. Below 620nm, the IQE of PQC deteriorates and it increases at UV region of the spectrum. At 365nm, the relative drop in IQE is ~50% and it corresponds the relative variation between EQE_{PQC} and measured EQE (refer to figure 6.9(a)). This match confirms that recombination centres are responsible for degrading the performance in the UV and visible region. Improved photon absorption near the junction, increases the IQE above 625nm.

6.5 Increasing the fill-fraction of PQC solar cell

Air fill fraction of the PQC solar was increased by increasing the hole diameter. In section 6.3, 12-fold PQC solar cell with lattice pitch of 700nm and hole diameter of 350nm was studied before and after hybridisation. In this section, air fill fraction of the PQC is increased from 22% to 49% for the same pitch. In other words, the hole diameter is increased from 350nm to 525nm in diameter for the same pitch (700nm). Figure 6.10 (a) and (b) shows the top view and cross-sectional SEM image of fabricated hybrid PQC/QD Si solar cell. From the top view, PQC has a lattice pitch of 741nm (~750nm) and hole diameter of 529nm (~525nm). In this section, PQC solar cell denotes 12-fold quasi PQC with pitch of 700nm and hole diameter of 525nm unless otherwise stated. PQCs have been etched to depth of 500nm and it penetrates into metallurgical junction at 400nm. Figure 6.10(b) shows the cross-sectional SEM image of PQC solar cell deposited with QD-630. QDs were dynamic spin coated at spin speed of 3000rpm. As a result, the nanoholes are filled with a 100nm thick layer of QDs and the sidewalls are also coated. From zoomed out image in figure 6.9(b), it can be seen that QD layer within the nanoholes is uniform over a large area.

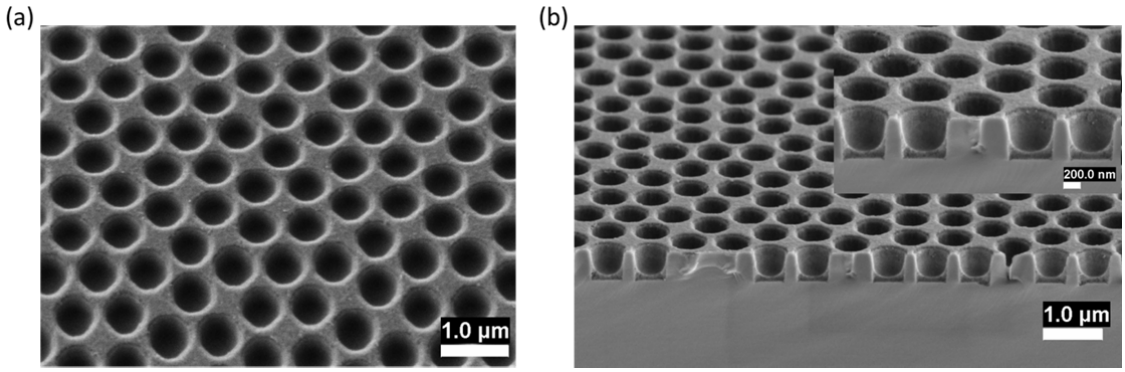

Figure 6.10: (a) Top view of PQC solar cell with pitch of 700nm and hole diameter of 525nm. (b) Cross-sectional SEM image of PQC solar cell. PQC nanoholes have the depth of 500nm and nanoholes are filled with 100nm of QD layer.

The effect of PQC air –fill fraction was investigated, from the absorption of PQC solar cells with hole diameters of 350nm and 525nm for the same pitch (700nm). Figure 6.11 shows that as the hole diameter increases from 350 nm to 525nm, the absorption of PQC Si solar cell is enhanced for the entire measured spectral range 300nm-1100nm. At 315nm, the relative enhancement in absorption is 58%, which then drops to 5.8% at 380nm. For wavelength between 385nm and 730nm, the enhancement varies between 6%-11%. Above 730nm, the absorption increases until the relative enhancement of 20% at 960nm is obtained. At 1000nm and 1100nm, the relative enhancement absorption drops to ~16%.

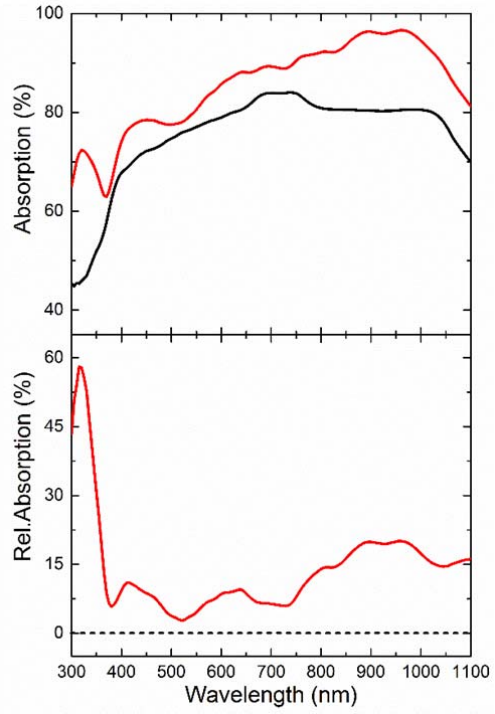

Figure 6.11: Absorption of PQC with pitch 700nm for two hole diameter 350nm (black solid line) and 525nm (red solid line) and the relative variation for hole diameter 525nm is shown in plot below.

Increase in air-fill fraction for PQC lattice showed the increase in absorption of the incoming photons between 300nm-1100nm. The increase in absorption is due to reduction of effective refractive index of PQC. The effective refractive index for one dimensional calculation can be determined from the relation [1] $n_{PQC}^2 = Fn_{air}^2 + (1-F)n_{Si}^2$. In this equation n_{PQC}, n_{air} and n_{Si} are refractive index of PQC, air and silicon respectively. The fill factor (F) here denotes the ratio of air to silicon. The air fill fraction increase from 22% to 49% when the hole diameter is increased from 350nm to 525nm. The refractive index of Si at 630nm is 3.879 [2]; the effective refractive index of PQC with hole diameter 350nm and 525nm are respectively 3.457 and 2.849 respectively. The reduction effective refractive index of silicon reduces the reflection at air/semiconductor interface. The following section will discuss the optimised deposition of QD and will present optimised QD deposition. Using the best QD spin speed, the optical characterisations were carried out before and after hybridisation with QD-630.

6.5.1 QD deposition optimisation

EQE dependence on QD deposition at different speeds was investigated. QDs in toluene are dynamically dispersed at required speeds. QDs with emission peak at 630±15nm were deposited at spin speeds of 1500rpm, 2000rpm, 3000rpm and 5000rpm. When QD-630 is deposited with 1500rpm spin speed (Figure 6.12 (a)), the EQE of PQC solar cell showed enhancement between 320nm and 840nm. The relative enhancement in EQE increases from 3.6% at 320nm to 22% at 385nm. The initial decrease in EQE is attributed to absorption and re-emission loss taking place in the QD layer. As QDs have high absorption cross section, they tend to absorb almost all the high energy photons. QD-630 used in this study has the quantum yield of ~50% and there is 50% chance for losses to occur due to absorption and re-emission. For near unity quantum yield QDs, this loss will significantly reduce thus the highest enhancement can be observed near UV wavelengths. Above 385 nm, the EQE enhancement gradually decreases at longer wavelength. That is the relative EQE drops from 21.5% at 390 nm to 1.85% at 630 nm. This occurs due to the absorption properties of QDs. QD-630 have the highest absorption at 300nm and then it exponentially drops to almost zero between 630-650nm. QDs absorbed photons are then transferred to Si via LDS and RET. Above 630nm, the EQE increases and reaches 10% at 730nm. Since QDs do not absorb in this region, the enhancement can be attributed to refractive index matching. Above 845nm, hybridisation of the PQC with QD-630 at spin speed 1500 rpm is proven to be detrimental.

As QD deposition speed is increased to 2000rpm (Figure 6.12 (a)), distinct enhancement is observed near-UV. A relative enhancement of 29% at 365nm was achieved which is 11% higher than the QDs deposited at 1500rpm. Increasing the speed to 3000rpm resulted in further enhancement in EQE in the UV region, obtaining a relative enhancement of 36.5% at 365nm. The QDs deposited at 2000 rpm and 3000 rpm is less detrimental to EQE in the near-infra red region. Increasing the QD deposition speed to 5000 rpm showed very little enhancement in EQE compared to QDs deposited at 3000 rpm.

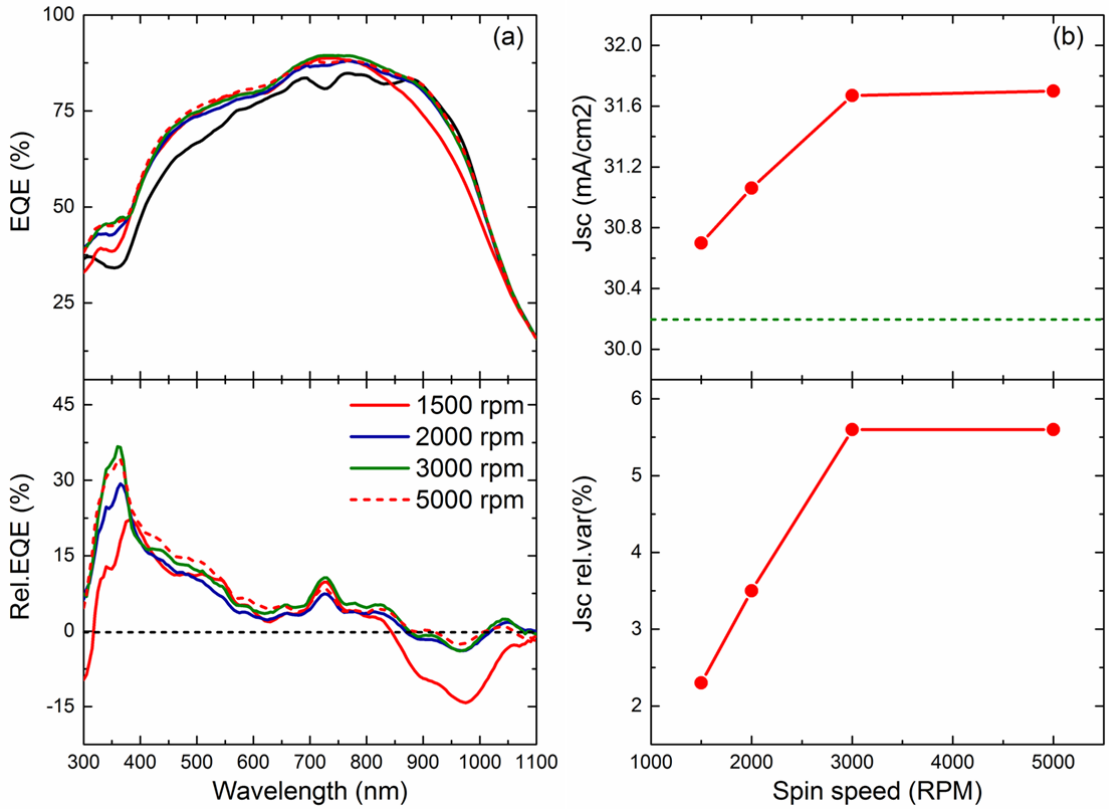

Figure 6.12: (a) EQE as a function of different spin speeds, 1500rpm(red), 2000 rpm(blue),3000rpm(green) and 5000 rpm (dashed red). The black solid line represents the EQE of PQC solar cell before hybridisation. Relative variations in EQE after hybridisation at different spin speed are shown in the bottom panel. (b) Short-circuit current density achieved when PQC solar cell is hybridised with QD-630 at different spin speeds. Green dashed line corresponds to reference Jsc before hybridisation. The relative variations in Jsc after hybridisation are shown in the bottom panel.

From the EQE measurements, the short circuit density (Jsc) has been calculated and plotted in Figure 6.12 (b). The Jsc of PQC solar cell before hybridisation is 30.2mA/cm^2 and is presented as green dashed line. The Jsc increases with spin speed from 30.7mA/cm^2 at 1500 rpm to 31.67 A/cm^2 at 3000rpm. When QDs deposition speed is increased more than 3000rpm, the Jsc enhancement is negligible. The relative enhancement in Jsc for hybridisation at different speed is shown in the bottom panel of Figure 6.12 (b). The maximum relative Jsc enhancement of 5.6% is obtained for QDs deposited at 3000rpm and 5000rpm.

6.5.2 Optical characterisation of hybrid PQC/QD Si solar cell

PQC solar with pitch of 700nm and hole diameter of 525nm gave the maximum Jsc (31.67%) when hybridised with QD-630 at 3000rpm. The optical properties of the PQC solar cell before and after hybridisation with QDs will be discussed in this section.

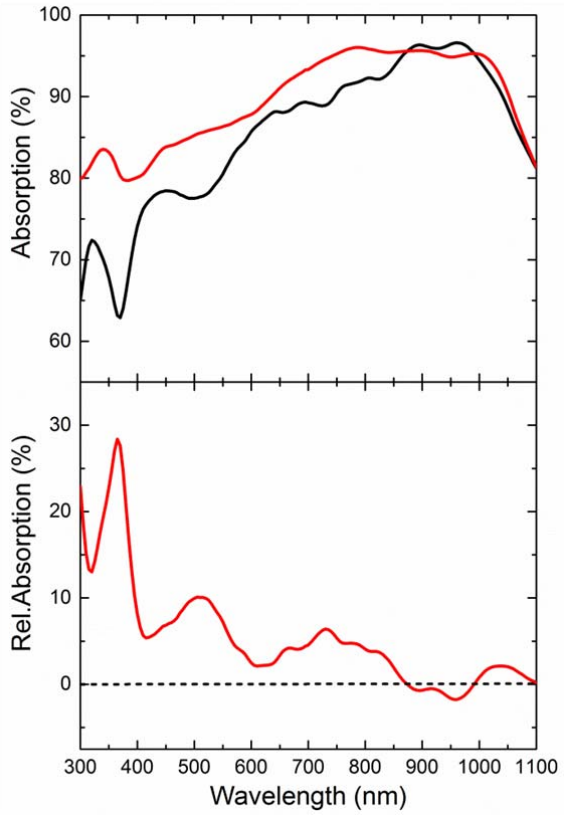

Figure 6.13: Absorption of the PQC solar cell before (black solid line) and after (red solid line) hybridisation with QD-630. The relative variations in absorption after hybridisation are shown in the bottom panel of the graph.

Due to hybridisation of PQC solar cell, the absorption (Figure 6.13) increased between 300nm and 870nm, with the maximum relative enhancement of 28% at 365nm and then a gradual drop until it reached 2% at 630nm was observed. QDs have strong absorption in the UV region. It then drops exponentially until 630nm. Above 630nm, QDs do not absorb. The dips and peak in absorption are due to PQC, this means the coupling of the light into hybrid PQC is stronger at certain wavelengths. Above the QD absorption, the enhancement is due to only refractive index matching. The absorption increases from 2% at 635nm to 6.3% at 735nm. Above 735nm, there is a gradual drop until the relative enhancement almost reaches zero at 870nm. Between the wavelengths of 875nm and 990nm, the hybridisation with QD 630 has a detrimental effect, reducing the absorption by 1%. Nevertheless, the overall increase in absorption shows that the hybridisation of PQC solar cell with QD-630 is beneficial.

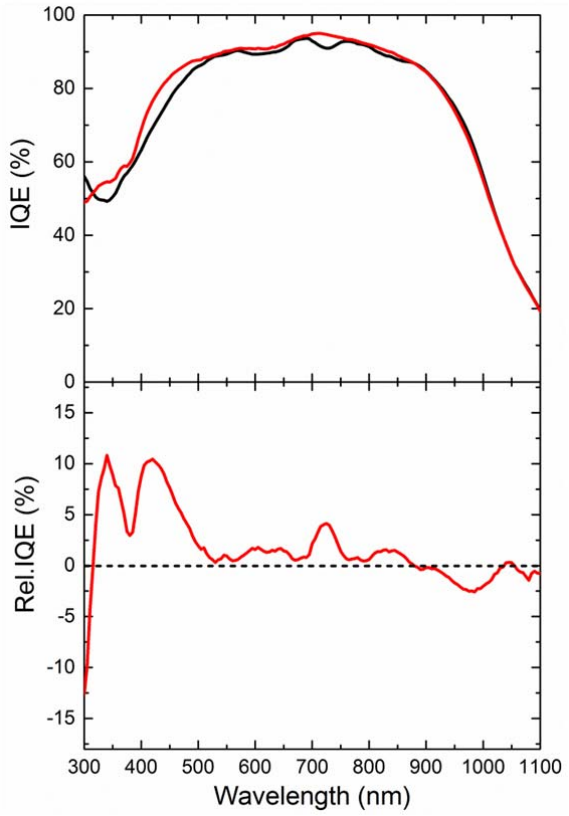

Figure 6.14: The IQE of the PQC solar cell before and after hybridisation with QD-630 along with the relative variation in IQE in the bottom graph.

The efficiency of charge generation and collection from solar cell can be determined from IQE measurements. The IQE of PQC solar cell (refer, Figure 6.14) shows the enhancement between 320nm and 875nm. At 340nm, there is about 10.8% relative enhancement in IQE. The relative enhancement in IQE starts to drop at 420nm from 10% until it reaches 0.5% at 530nm. For the wavelength between 530nm and 630nm, the IQE enhancement remains less than 1.5%. Above the absorption of QDs, the IQE enhancement drops to almost zero with peaks at 730nm and 835nm which arises due to the change in effective penetration depth.

The time resolved photoluminescence of the QD-630 (Figure 6.15) on PQC solar is compared with QDs on glass (reference) with excitation power of 1µW. Acceleration in decay of QDs is observed when deposited on PQC solar cell with the pitch of 700nm and hole diameter of 525nm. The decay rate of QD-630 is calculated from bi-exponential fit (equation 24) and is equal to $0.085ns^{-1}$ and $0.143ns^{-1}$ for reference and PQC solar cell respectively. The efficiency of RET from this hybrid QD/PQC solar architecture is 40.2%, which states that 40% of electron-hole pair generated in QDs are transferred to PQC solar cell through non-radiative RET.

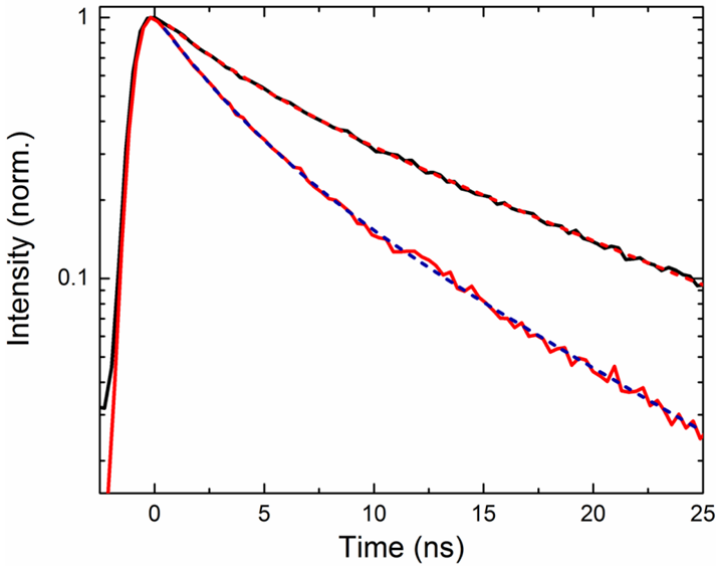

Figure 6.15: Decay dynamics of QD-630 deposited on glass (black solid line) and on PQC (red solid line) solar cell with pitch of 700nm and hole diameter of 525nm. The red dashed line and blue dashed line are the fits for QD-630 on glass and PQC solar cell.

On comparison with QD-630 coated planar Si solar cell, there is an absolute 8% increase in RET efficiency. The enhancement in RET efficiency is attributed to nano-template, which increases the surface area of QD/Si interface. The true benefit from the hybrid PQC/QD Si solar cell is that generated electron-hole pairs at QDs is transferred to close proximity of p-n junction. Non-radiative transferred electron-hole pair are separated and collected at respective electrodes increasing the short-circuit current.

6.6 PQC boost the performance

This section draws the comparison between best hybrid PQC solar cell and best hybrid planar solar cell. Figure 6.16 shows the EQE of best planar and PQC solar cell devices before and after hybridisation with QD-630 .The best solar cell was determined by their short circuit density (Jsc). Planar (black solid line) solar cell has the maximum EQE of 60% between 635nm and 830nm. When patterned with 12-fold PQC with pitch of 700nm and hole diameter of 525nm, a significant enhancement in EQE was observed throughout measured spectral range 300nm-1100nm. Herein, PQC solar denotes 12-fold PQC lattice with pitch of 700nm and hole diameter of 525nm. Maximum EQE of 80%-85% was achieved for PQC solar cell between 660nm and 880nm. On comparing PQC patterned solar cell with planar Si solar cell, 145% relative enhancement of EQE is obtained at 300nm. The EQE of 12-fold PQC was also substantial in the near infra-red region with relative enhancement of 32% - 46% between 670nm and 980nm. After hybridisation with QD-630,

planar Si solar cell reached the maximum EQE of 88.4% at 695nm due to the efficient coupling of the light into the Si. Enhancement is also observed within the absorption region of QDs due to LDS, refractive index matching and RET. PQC solar cell when hybridised with QD-630 demonstrates enhancement in EQE over wide spectral range with maximum enhancement near UV.

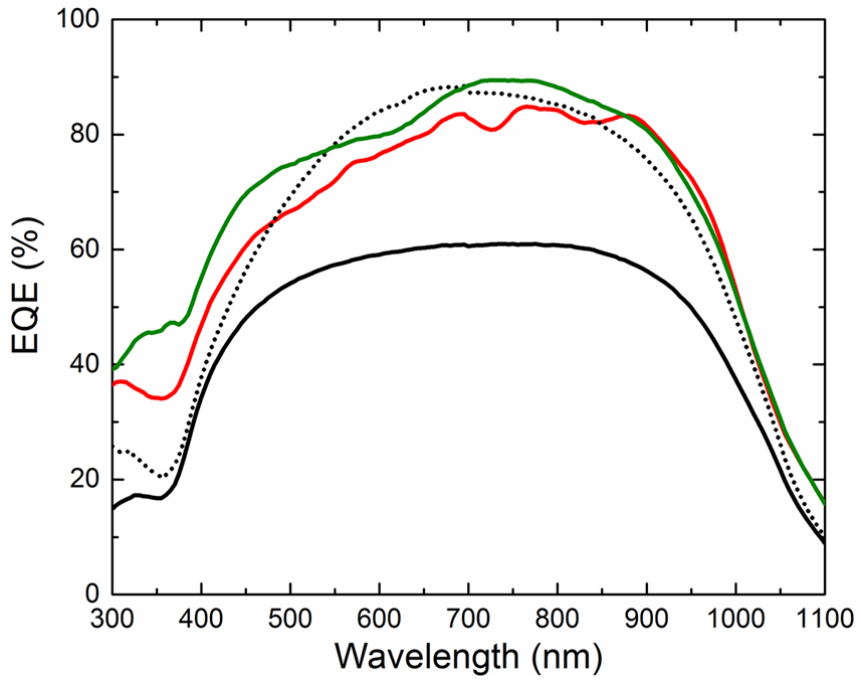

Figure 6.16: The EQE of best planar and PQC solar cell devices before and after hybridisation. The black and red solid line represents the planar and PQC solar cell before hybridisation. The black dotted line and green solid line corresponds to planar and PQC solar cell after hybridisation with QD-630.

The planar solar when hybridised with QD-630 at spin speed of 2000 rpm yielded a Jsc of 30.2mA/cm^2. The detailed information of planar solar cell before and after hybridisation is given in chapter 5. PQC solar cell with pitch of 700nm and hole diameter of 525nm achieved Jsc 31.67mA/cm^2 after hybridisation with QD-630 at spin speed of 3000rpm. In comparison to planar polished Si solar cell, an absolute and relative enhancement in Jsc of 9.17mA/cm^2 (22.5mA/cm^2 to 31.67mA/cm^2) and 41% was achieved after PQC patterning and hybridization with QD-630.

IQE of hybrid planar and PQC solar cell was also considered (Figure 6.17), hybrid PQC solar cell with QD-630 shows significant enhancement of IQE in the absorption region. Relative enhancement of 33% and 59% was achieved at wavelengths of 300nm and 360nm respectively. The IQE enhancement gradually drops to zero at edge of QD absorption region. The enhancement

in IQE of PQC is due to PQC lattice, LDS and RET. From EQE and IQE measurements, it is demonstrated that hybrid PQC structure is more efficient for photovoltaics than hybrid planar silicon solar cell.

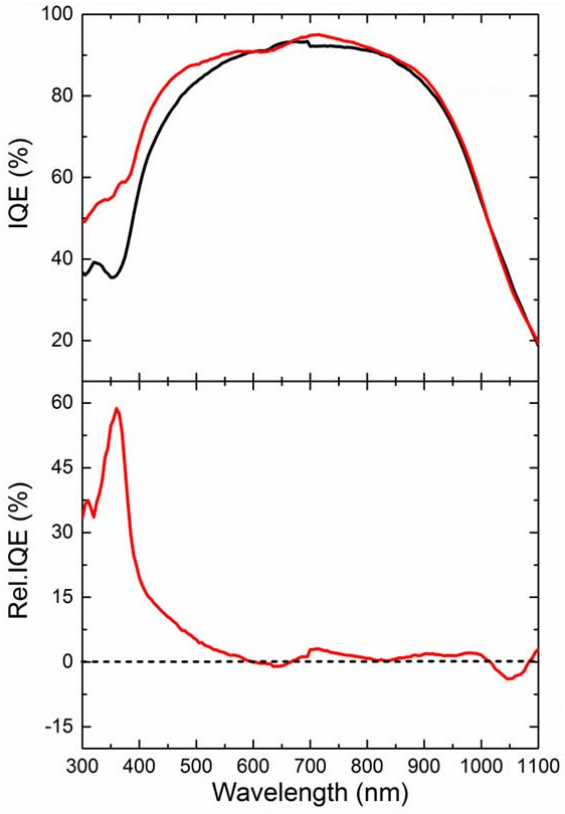

Figure 6.17: Shows the IQE of planar (black solid line) Si solar and PQC (red solid line) solar cell with pitch of 700nm and hole diameter of 525nm after hybridisation with QD-630. The IQE variation of hybrid PQC in comparison with hybrid planar is shown in below graph.

6.7 Conclusion

Patterning of 12-fold PQC lattice with pitch of 700nm and hole diameter of 350nm, the enhancement in Jsc was observed and it is due to efficient coupling of the light into the Si solar cell. On hybridisation with optimised QD deposition, Jsc of 30mA/cm^2 was obtained. In comparison with best hybrid planar device (chapter 5), the hybrid PQC achieved the same short circuit current. Also, 12-fold PQC's air fill fraction was increased by increasing the hole diameter from 350nm to 525nm for same pitch (700nm).

12-fold PQC with pitch of 700nm and hole diameter of 525nm, on hybridisation with QD-630 showed a drastic enhancement in solar cell performance. In comparison with planar polished Si solar cell, the hybrid PQC showed an absolute and relative Jsc enhancement of 9mA/cm^2 and 41% respectively. This optical enhancement strategy using PQC and QDs can be extended to thin film solar cells where the performance is limited due to poor absorption of incoming solar radiations.

References

1. C. Wiesmann, K. Bergenek, N. Linder, and U. T. Schwarz, "Photonic crystal LEDs - designing light extraction," Laser Photonics Rev. **3**, 262–286 (2009).

2. M. A. Green and M. J. Keevers, "Optical properties of intrinsic silicon at 300 K," Prog. Photovoltaics Res. Appl. **3**, 189–192 (1995).

Chapter 7: Conclusion and future work

7.1 Conclusion

Size dependent properties of colloidal QDs and easy integration into the devices make them an attractive material for current and future optoelectronics. QDs have demonstrated tuneable emission and absorption in UV and mid infrared regions of the electromagnetic spectrum. This thesis has shown the integration of QDs into LEDs and photovoltaic in quest of finding an efficient lighting emitter and harvesters.

QDs have found their way into the market with applications in solid-state lighting and as back lighting in displays. Sony, Samsung, LG and Amazon have used QDs as back lights for liquid crystal displays (LCDs) [1,2] where QDs are blended into polymer matrix and sealed into glass tube to avoid exposure from atmospheric oxygen [1]. Another similar approach is that QD polymer films [3] are sandwiched in barrier films to avoid degradation of QDs. Both the QD tubes and films are optically excited with InGaN blue LEDs. The light generated by the LED stack is trapped as guided modes due to total internal reflection. Photonic crystals have been employed to improve the light extraction of LEDs. Chapter 3 showed that by integrating QDs into 12-fold photonic quasi crystal LEDs, the effective colour conversion quantum yields of 123% and 110% for single colour QDs and white LEDs respectively were achieved. It is worth mentioning that these results are significantly higher than previously reported colour conversion quantum yield [4]. This improvement in performance was achieved through etching PQC into quantum wells and depositing QDs into the PQC templates. This architecture also benefits from non-radiative RET transfer from quantum wells to QDs and has the efficiency of 82%.

QDs requires more robust method for integration into the device where some examples include contact printing [5], spray coating [6] and inkjet printing [7,8] for it to be viable for real world applications. In chapter 4, inkjet printing was used to achieve controlled QD deposition over a certain area. The QDs ink was ejected on to the hybrid PQC colour tunable LED. Reproducibility and correlated colour temperature tunability was demonstrated. The PQC LED module had a thickness of 150μm therefore it is possible to make thin QD LED displays by using pixelated deposition.

QDs are strong absorbers due to their quantum confinement and by optimising the size and material composition; change in their absorption region can be achieved. The absorption region can be tuned either to be in visible or infrared region of the spectrum. The PbS or PbSe are extensively researched material for photovoltaic applications due to their near infrared emission. In chapter 5, PbS QDs used as superficial layer on the Si solar cell showed broad spectral enhancement in the EQE, with absolute (1.37%) and relative (20%) increase in photon conversion efficiency. The

enhancement in the solar cell performance was caused by luminescent down shifting (LDS), refractive index matching, resonant energy transfer (RET) and scattering at QD aggregate. CdSe/ZnS (core/shell) QDs were also used to hybridise the planar Si solar and their optical enhancement were studied. It was demonstrated that QDs can act as a refractive index layer enhancing the coupling of the light into the solar cell in addition to LDS and RET. The optimum QD thickness was investigated to maximise the short circuit enhancement of the hybrid QD/planar Si solar cell.

Harvesting the solar power has become a global phenomenon and the demand for efficient and cheaper photovoltaics is rapidly growing so is the awareness within and outside the academia. In chapter 5, QDs was demonstrated to improve the performance of the planar Si solar cell. In chapter 6, 12-fold photonic quasi crystal pattern was etched into the planar Si solar cell and was used as a template to bring QDs in proximity to p-n junction. QDs were deposited in nanoholes cavities and optimised QD thickness was determined. The air fill fraction for PQC solar cell was also increased for efficient light trapping into the solar cell. The PQC solar cell with optimised QD deposition demonstrated 41% relative enhancement in short circuit current through LDS, RET and efficient light trapping.

7.2 Future work

Hybrid 12-fold PQC LED has shown a great promise for efficient pumping of QDs. The PQC lattice structure is not optimised and requires further optimisation for efficient transfer (radiative and non-radiative) of photons from QWs to QDs. In this work, only spherical colloidal nanostructure (QDs) was considered for hybrid devices. These studies can be extended further to different nanostructures like nano rods and tetrapod semiconductor crystals. For hybrid PQC LEDs to reach market from research labs, a lifetime and stability characterisations of QDs need to be investigated. One of the most important aspect to consider is to encapsulate the QDs to avoid degradation over time due to the atmosphere. Research publications are claiming close to unity photoluminescence, it would also be interesting to analysis the hybrid PQC LED with high quantum yield QDs.

Using colloidal QDs, different optical enhancement schemes were proposed in this thesis. Hybrid PQC QD/Si solar cell was shown to enhance the performance of the Si solar cell. PQC pattern transfer creates surface states at the sidewall of etched nanoholes, which requires counter active measures to reduce these surface states. Atomic layer deposition of Al_20_3 is a proposed method to reduce the surface states significantly and it can be achieved by growing few nm of oxide layer. Surface states free hybrid PQC cell solar can benefit from non-radiative RET electron-hole pairs. This idea can be extended to thin Si PV, which would have a greater impact on solar community where photon absorption efficiency has limited its performance below its bulk counterpart.

References

1. J. S. Steckel, J. Ho, C. Hamilton, C. Breen, W. Liu, P. Allen, J. Xi, and S. Coe-Sullivan, "12.1: Invited Paper: Quantum Dots: The Ultimate Down-Conversion Material for LCD Displays," SID Symp. Dig. Tech. Pap. **45**, 130–133 (2014).

2. Z. Luo, D. Xu, and S. T. Wu, "Emerging Quantum-Dots-Enhanced LCDs," J. Disp. Technol. **10**, 526–539 (2014).

3. J. Chen, V. Hardev, J. Hartlove, J. Hofler, and E. Lee, "66.1: Distinguised Paper: A High-Efficiency Wide-Color-Gamut Solid-State Backlight System for LCDs Using Quantum Dot Enhancement Film," SID Symp. Dig. Tech. Pap. **43**, 895–896 (2012).

4. V. Wood and V. Bulović, "Colloidal quantum dot light-emitting devices," Nano Rev. **1**, 1–7 (2010).

5. T.-H. Kim, K.-S. Cho, E. K. Lee, S. J. Lee, J. Chae, J. W. Kim, D. H. Kim, J.-Y. Kwon, G. Amaratunga, S. Y. Lee, B. L. Choi, Y. Kuk, J. M. Kim, and K. Kim, "Full-colour quantum dot displays fabricated by transfer printing," Nat. Photonics **5**, 176–182 (2011).

6. K.-J. Chen, H.-C. Chen, K.-A. Tsai, C.-C. Lin, H.-H. Tsai, S.-H. Chien, B.-S. Cheng, Y.-J. Hsu, M.-H. Shih, C.-H. Tsai, H.-H. Shih, and H.-C. Kuo, "Resonant-Enhanced Full-Color Emission of Quantum-Dot-Based Display Technology Using a Pulsed Spray Method," Adv. Funct. Mater. **22**, 5138–5143 (2012).

7. V. Wood, M. J. Panzer, J. Chen, M. S. Bradley, J. E. Halpert, M. G. Bawendi, and V. Bulović, "Inkjet-Printed Quantum Dot–Polymer Composites for Full-Color AC-Driven Displays," Adv. Mater. **21**, 2151–2155 (2009).

8. A. M. Elliott, O. S. Ivanova, C. B. Williams, and T. a. Campbell, "Inkjet printing of quantum dots in photopolymer for use in additive manufacturing of nanocomposites," Adv. Eng. Mater. **15**, 903–907 (2013).

Appendix A: Correlated colour temperature tunable light emitting diodes

A.1: Fabrication of PQC LED using link chip process

The LED epi structure was grown as described in section 3.2.1. Here process steps involved in the fabrication of hybrid LED is shown.

1. Indium tin oxide (ITO) of 230nm is deposited on LED stack using e-beam evaporation and SiO_2 of 400nm is deposited using plasma enhanced chemical vapour deposition

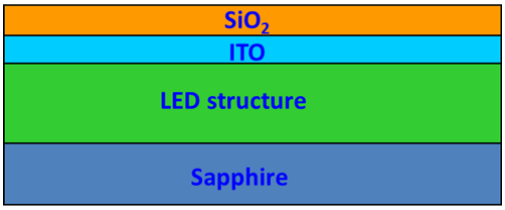

2. Using spin deposition 360nm thick imprint layer is deposited on top of SiO_2 and reactive ion etching of SiO_2 in O_2 and CHF_3 plasma.

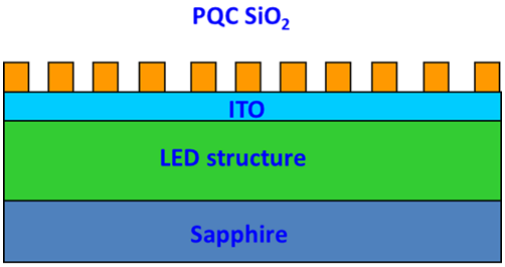

3. Define PQC etch area using photo-lithography and using ICP the LED stack is etched up to depth of 1.2µm including ITO film.

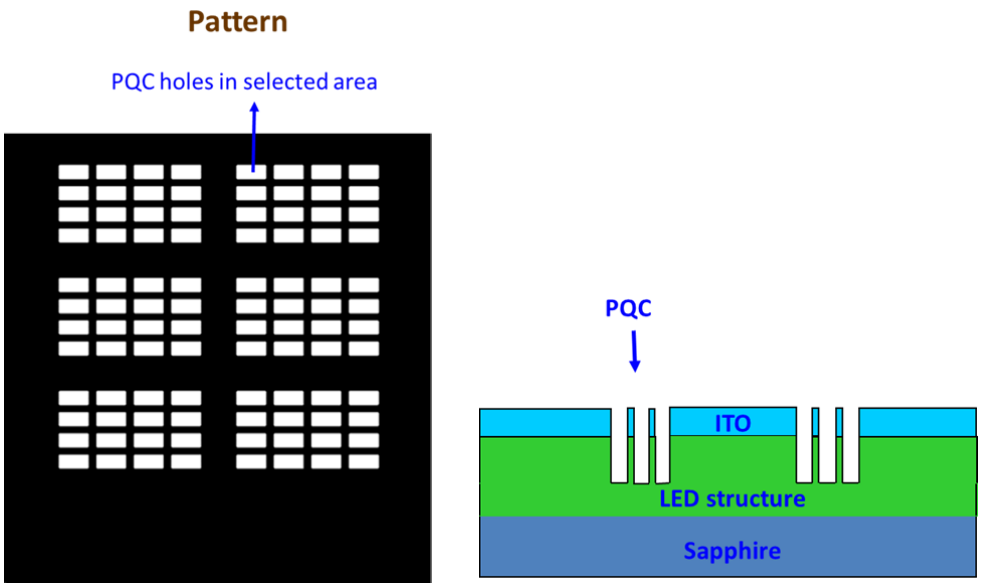

4. ITO area is defined using photolithography. The exposed ITO area is etched using mixed solution of hydrochloric acid (HCl)/ ferric chloride ($FeCl_3$) . After ITO etching , the LED stack is annealed in furnace in at 500°C for 20minutes in nitrogen atmosphere.

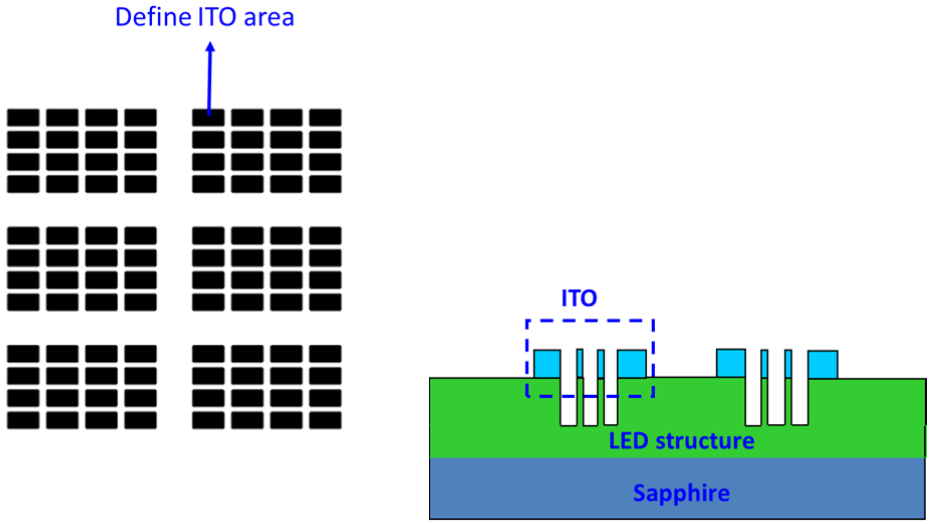

5. Define Mesa area using photolithography and etch on to n-GaN layer. Mesa etching was performed using $Cl_2/BCl_3/Ar$ gas in an ICP-RIE system. The Mesa was etched up to depth of 1.2µm

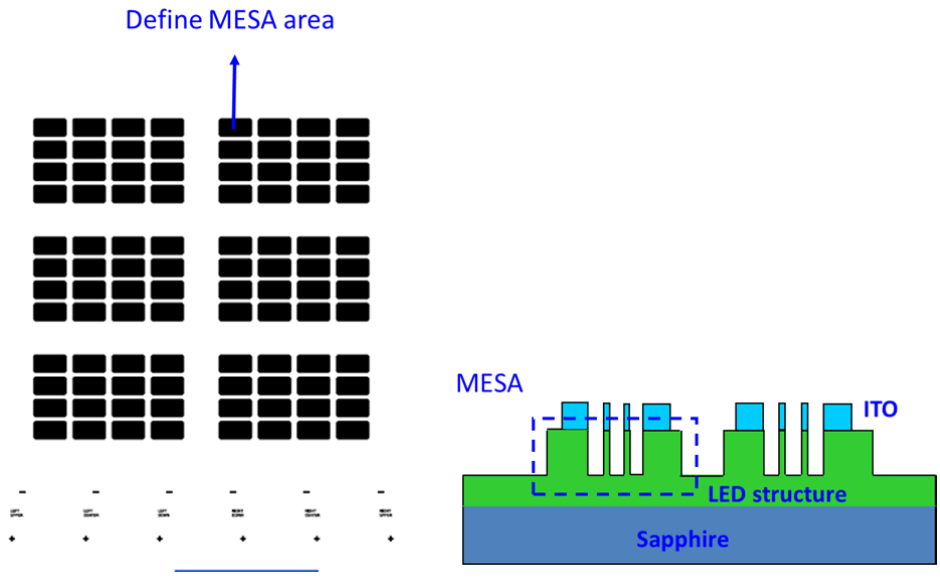

6. Chip isolation in modular array of LED is obtained by deposition 10µm SiO_2 and defining the area with photolithography and ICP etching about 8µm

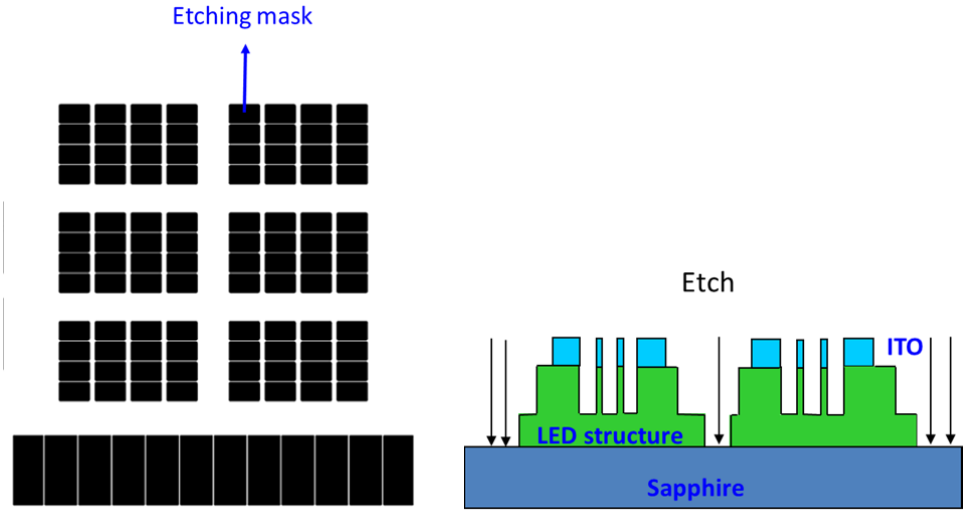

7. The side walls of isolated chips are passivated and isolated with 500nm thick SiO2. For contacts SiO_2 is defined using photolithography and etched with buffer oxide etch.

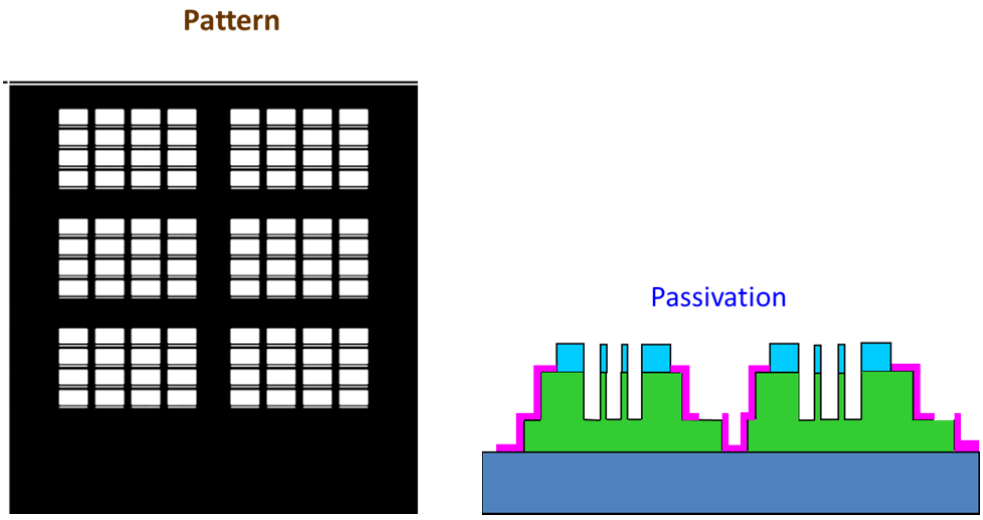

8. PN pad is defined with photolithography and 1.3µm thick gold is evaporated using e-beam evaporation and lifted-off. The similar process flow was used for PQC LED described in chapter 3, the only difference the masks were designed to have 80 micro LEDs with one positive and negative contact.

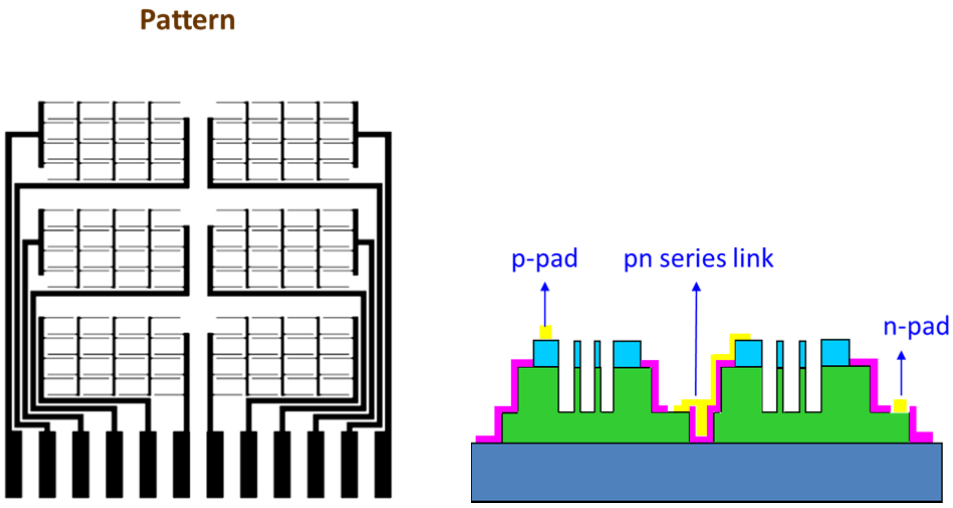

A.2: Semi-log J-V characteristics of PQC LED

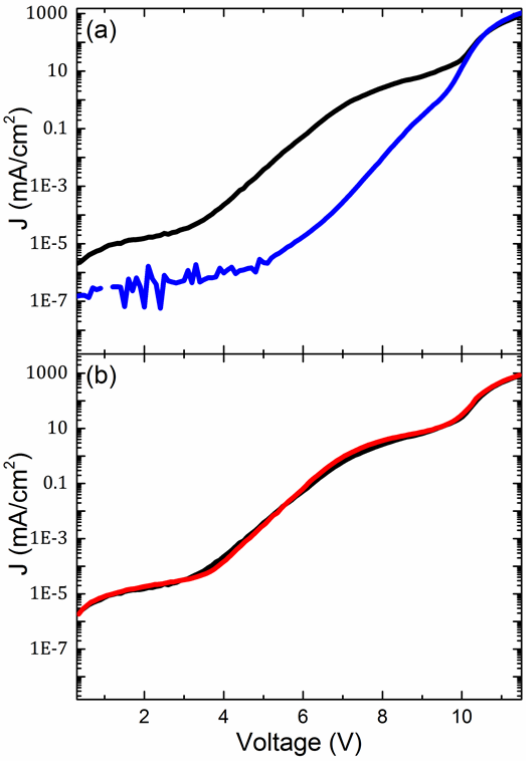

Figure: (a) semi-log J-V characteristics of a planar (blue) and of PQC (black solid line) LED. (b) semi-log J-V characteristics of a PQC LED (black solid line) and after hybridisation (red solid line) with QD-585

Appendix B: Correlated colour temperature tunable light emitting diodes

B.1: Inkjet printing recipe

Recipe name – Quantum dot_actual 29

Jetting speed 6m/s

Firing voltage 16 -19V

Drop spacing - 5µm

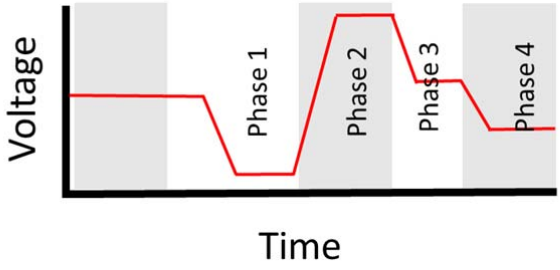

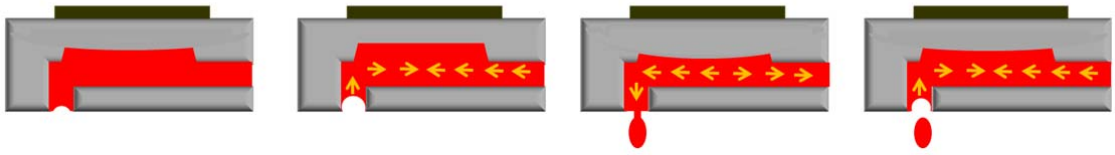

Phase 1	Phase 2	Phase 3	Phase 4
Voltage 16-19V	Level 7% Slew rate 1.44 Duration 3.77 µs	Level 73% Slew rate 1.44 Duration 3.77 µs	Level 53% Slew rate 0.58 Duration 0.896 µs

Appendix C: Quantum dots as route to enhance the performance of Si solar cells

C.1: Doping profile of Si Solar cell

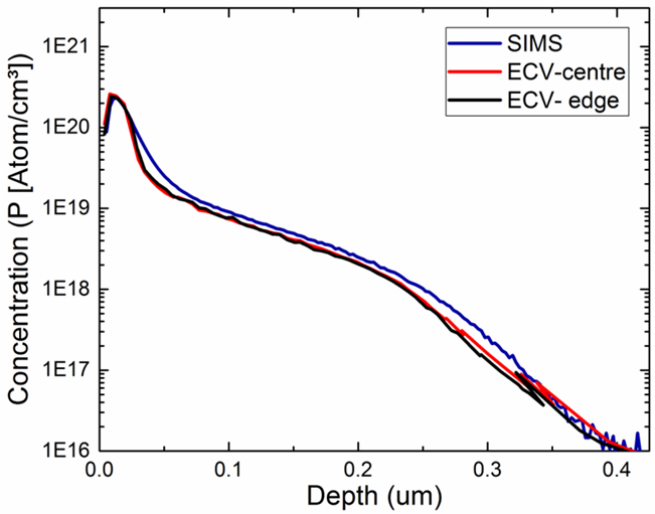

C.2: Optical constant of PbS QDs (QD-900)

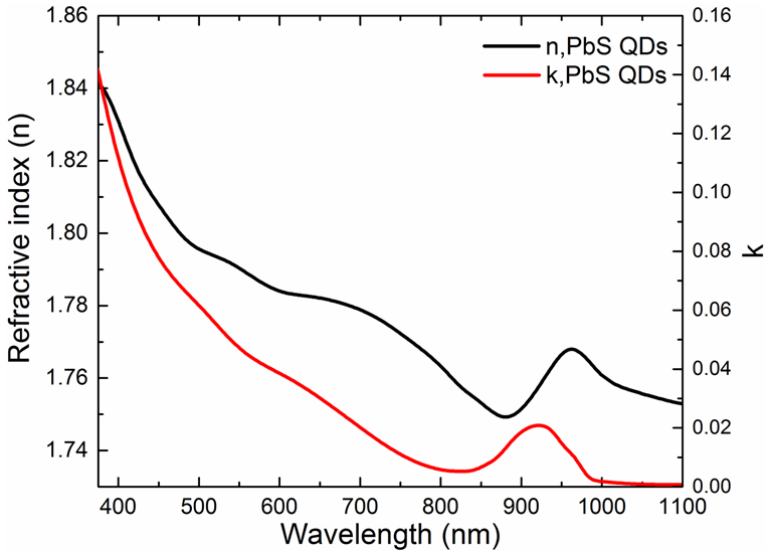

C.3: Optical constants of CdSe/ZnS QDs (QD-630)

The QDs (here QD-630) are spin coated on Si substrate and optical constants of QD layer are determined using woollam ellipsometer. First Cauchy dispersion model is used to determine the thickness in the transparent region (630nm-1100nm) of QD-630. After film thickness is determined B-spline dispersion model is used to determine optical constants of QD-630.

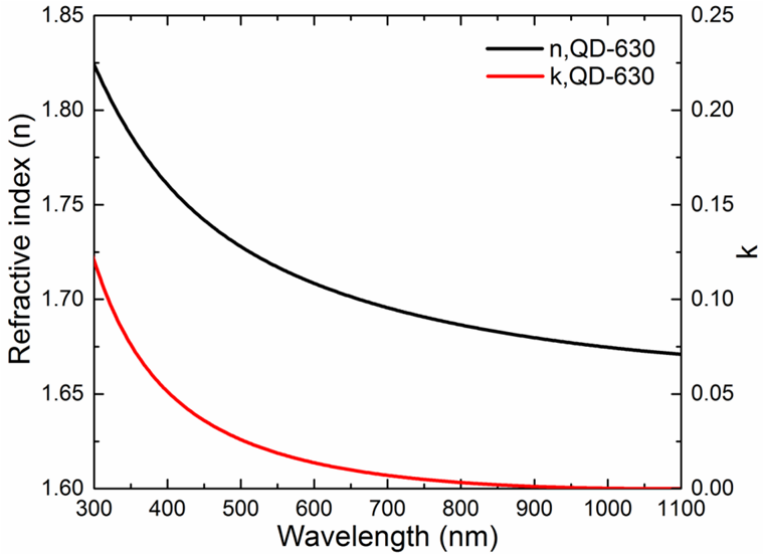

C.4: QD layer thickness versus spin speed for concentration 60mg/ml